Günter Krois

Alkali - Alkaline Earth Metal Molecules on Cold Helium Droplets

DOCTORAL THESIS

For obtaining the academic degree of
Doktor der technischen Wissenschaften

Doctoral Programme of Technical Sciences
Technical Physics

Graz University of Technology

Supervisor:
Univ.-Prof. Mag. Dr.rer.nat. Wolfgang E. Ernst
Institute of Experimental Physics

Co-Supervisor:
DI Dr.techn. Florian Lackner
Institute of Experimental Physics

Graz, July 2014

Abstract

In the course of this thesis three alkali-alkaline earth metal (Ak-Ake) molecules, namely lithium-calcium (LiCa), rubidium-strontium (RbSr) and rubidium-calcium (RbCa) have been prepared on helium nanodroplets and investigated by resonance enhanced multi-photon ionization time-of-flight spectroscopy, laser induced fluorescence spectroscopy and dispersed fluorescence spectroscopy. The combination of these methods together with theoretical calculations allowed a characterization of previously uninvestigated molecules (RbSr and RbCa). Comparisons with known data (LiCa) verified that molecular parameters of free molecule can be deduced from spectra of Ak-Ake molecules on He droplets. Especially RbSr and RbCa are interesting for ultracold molecular physics, since they are the most promising candidates for the realization of a molecular quantum degenerate gas of molecules with an electric and a magnetic moment. Despite this interest, no experimental data was available before, since these molecules are hard to access experimentally. Helium nanodroplet isolation spectroscopy (HENDI) provides a powerful experimental method that allows to easily form and investigate tailored molecules, as is shown in this work. In addition to the investigations of Ak-Ake molecules, results for Ak and Ake dimers on He droplets are presented in this work, which were obtained in the course of the experiments.

Zusammenfassung

Das Ziel dieser Arbeit war die experimentelle Untersuchung von Alkali-Erdalkali (Ak-Ake) Molekülen auf Helium Tropfen. Die drei Moleküle Lithium-Kalzium (LiCa), Rubidium-Strontium (RbSr) und Rubidium-Kalzium (RbCa) wurden mittels resonanzverstärkter Mehrphotonenionisations Flugzeitspektroskopie, Laserinduzierter Fluoreszenzspektroskopie und dispersiver Fluoreszenzspektroskopie untersucht. Die Kombination dieser Methoden erlaubt eine Charakterisierung von bis dato unbekannten Molekülen (RbSr und RbCa). Der Vergleich mit bekannten Daten (LiCa) verifizierte, dass Molekülparameter von freien Molekülen aus den Spektren von Ak-Ake Molekülen auf Heliumtropfen gewonnen werden können. Diese Moleküle sind im Speziellen für die ultrakalte Molekülphysik interessant, da sie die vielversprechendsten Kandidaten für die Erzeugung eines molekularen quanten-entarteten Gases mit elektrischem und magnetischem Moment darstellen. Trotz dieses Interesses waren bis zum aktuellen Zeitpunkt keine experimentellen Daten über diese Moleküle vorhanden, da sie schwer zu präparieren sind. Die Methode der Helium Nanotropfen Isolationsspektroskopie (HENDI) erlaubt eine einfache Bildung und Untersuchung von beliebigen Molekülen, was in dieser Arbeit unter Beweis gestellt werden konnte. Zusätzlich zu den Untersuchungen von Ak-Ake Molekülen sind in dieser Arbeit Ergebnisse zu spektroskopischen Untersuchungen von Ak und Ake Dimeren auf Helium Tropfen dargestellt, die sich aus den Experimenten mit Ak-Ake dotierten He Tropfen ergeben haben.

Articles Related to This Work

1. *Characterization of RbSr Molecules: A Spectral Analysis on Helium Droplets*
   G. Krois, F. Lackner, T. Buchsteiner, J. Pototschnig and W. E. Ernst;
   Submitted (2014); [87]

2. *Helium Droplet Assisted Preparation of Cold RbSr Molecules*
   F. Lackner, G. Krois, T. Buchsteiner, J. Pototschnig, and W. E. Ernst;
   Submitted (05.2014); [92]

3. *Spectroscopy of Cold LiCa Molecules Formed on Helium Nanodroplets*
   G. Krois, J. Pototschnig, F. Lackner and W. E. Ernst;
   J. Phys. Chem. A; 117, pp13719-13731, (2013)
   DOI: http://dx.doi.org/10.1021/jp407818k; [88]

4. *Spectroscopy of Lithium Atoms and Molecules on Helium Nanodroplets*
   F. Lackner, J. Poms, G. Krois, J.V. Pototschnig and W. E. Ernst;
   J. Phys. Chem. A, 117, pp11866-11873, (2013)
   DOI: http://dx.doi.org/10.1021/jp4030238; [96]

5. *Rydberg-Ritz Analysis and Quantum Defects for Rb and Cs Atoms on Helium Nanodroplets*
   F. Lackner, G. Krois and W. E. Ernst;
   Mol. Phys. 111, 14-15, (2013)
   DOI: http://dx.doi.org/10.1080/00268976.2013.788792; [93]

6. *Rubidium on Helium Droplets: Analysis of an*
   Exotic Rydberg Complex for $n^* < 20$ and $0 <= l <= 3$.
   F. Lackner, G. Krois, M. Koch and W.E. Ernst
   J. Chem. Phys. Lett. 10, pp1404-1408, (2012)
   DOI: http://dx.doi.org/10.1021/jz300381y; [94]

Articles 1-3 form the main part of this work and are partially contained in the results chapter. The theoretical calculations in these publications have been performed by Johann Pototschnig and will be a part of his PhD thesis [133]. Article 4 is related to this work and its contents is summarized here. Articles 5-6 are only indirectly related to this work and are contained in the PhD thesis of Florian Lackner [91].

EIDESSTATTLICHE ERKLÄRUNG

AFFIDAVIT

Ich erkläre an Eides statt, dass ich die vorliegende Arbeit selbstständig verfasst, andere als die angegebenen Quellen/Hilfsmittel nicht benutzt, und die den benutzten Quellen wörtlich und inhaltlich entnommenen Stellen als solche kenntlich gemacht habe. Das in TUGRAZonline hochgeladene Textdokument ist mit der vorliegenden Dissertation identisch.

I declare that I have authored this thesis independently, that I have not used other than the declared sources/resources, and that I have explicitly indicated all material which has been quoted either literally or by content from the sources used. The text document uploaded to TUGRAZonline is identical to the present doctoral dissertation.

Datum / Date

Unterschrift / Signature

Contents

CHAPTER 1

Introduction to...

1.1 ... this Thesis

I would like to use these first pages of my thesis to give a rather personal motivation. In the introduction of my master thesis I wrote about the historical perspective of helium nanodroplets and their actual development as a tool to investigate species which are hard to form or study without a matrix. At that point I found the idea interesting, but did not pursue the thought further. Now, in retrospect of my PhD thesis, all the steps taken since my master thesis fall into line smoothly. A wide range of experience with alkali atom and molecule doped He droplets has been gained in our laboratory since its setup in 2004. With the help of the experimental amendments developed in my master thesis and the beginning of my PhD thesis we were able to successfully dope helium nanodroplets with both alkali (Ak) and alkaline earth (Ake) atoms at the same time. On the prototype of lithium and calcium we saw that they do form a molecule (LiCa) and that the recorded spectra reveal valuable information about these Ak-Ake molecules. This allowed us to advance to new molecules, using the method of helium nanodroplet isolation spectroscopy to form and investigate molecules that were not investigated before, such as rubidium-strontium (RbSr) and rubidium-calcium (RbCa).

A special motivation for the investigation of these exotic species was the rising interest into their structure in ultracold molecular physics. Since the middle of the 90's and the first achievement of a Bose-Einstein-Condensate (BEC) of alkali atoms [5, 18, 35], many important findings have been reported in this area along with even more ideas about what can be done next. One such idea is the formation of ultracold molecules from ultracold atoms, which may enable to control molecular dynamics, opening fields such as ultracold controlled chemistry, see ref. [27] for a detailed description of several applications. For several molecules this has already been achieved: For homonuclear alkali dimers [34, 155] as well as for heteronuclear diatomic alkali molecules [123, 124] and very recently even for homonuclear alkaline earth dimers [149]. However, there is a new class of molecules which is especially interesting because of their electric and magnetic dipole moment, due to their unpaired electron - which the aforementioned molecules do not possess. Due to the restrictions the current cooling and trapping methods impose on the atoms, mainly alkali and alkaline earth atoms have been brought to quantum degeneracy[1] up to

[1] Note, *quantum degeneracy* for a gas of particles is reached when its behavior is dominated by its spin nature rather than its temperature. Quantum degeneracy can be reached for both bosons and fermions, but lead to

now. Hence, the best option to form an ultracold molecule with an unpaired electron is a mixed alkali-alkaline earth molecule. For this, especially RbSr is an outstanding candidate.
Therefore, it was an obvious choice for us to pick RbSr to investigate on helium droplets, so that we might provide important experimental insights into the up to now only theoretical investigation of this molecule in the spotlight of ultracold molecular physics.

This thesis is structured as follows: In the sections of the introduction the necessary prior knowledge to comprehend the results are presented in a short and simple form, including a cursory introduction into the field of ultracold molecules. The successive chapters explain the experimental setup and methods in detail: The interested reader will get a thorough idea how the experiments were performed and future colleagues will find useful information and technical details for the reproduction of the experiments. In the last chapter the results are listed, divided into sections for each investigated Ak-Ake molecule (LiCa, RbSr and RbCa) and some sections about additional results. The results are mainly taken directly from the corresponding articles, but have been restructured and some additional notes have been added as denoted in the introductions of the respective sections. In the end a short conclusion gives a summary of the insights gained in the course of this thesis.

different effects and are described by different theories.

1.2 ... Spectroscopic Units

Like most scientific communities, spectroscopists tend to use their own favorite units, which often leads to the confusion of others. Depending on the application, the units [eV], [nm], [GHz] and [cm^{-1}] may be used. This short section will give a short overview of their relation and the reason why they are used.

Naturally, energy levels of atoms and molecules should have a unit of energy, since Joule would be much too large for common energies in spectroscopy, the unit electron Volt [eV] is used (1.6×10^{-19} J). This unit describes the kinetic energy of an electron when accelerated by a potential of 1 V, therefore it is also convenient to use for acceleration voltages, e.g. in mass spectrometers.
Since spectroscopy implies the use of photons, the relation $E = h\nu$ suggests to use the frequency [1/s, Hz] of photons as a measure for the energy. However, this is an inconveniently small unit for most excitations of atoms and molecules, the visible range of light for example is in the range of $\sim 10^{14}$ Hz.
The wavelength $\lambda = c/\nu$ in [nm] (or other metric units) is the value directly measured by interferometers. Unfortunately, it is indirectly proportional to the energy, which is impractical for the study of regularities in spectra. Thus, in spectroscopy the wavenumber $\bar{\nu} = 10^7/\lambda\,[cm^{-1}]$ has been introduced, with the somewhat irritating unit of 'inverse centimeters'. However, this unit is directly proportional to the energy and its size allows a quite exact definition of energy levels with integer numbers. Interestingly, according to Herzberg [64] this unit has also been used, because the wavelength could be measured with a higher accuracy than the speed of light, which made wavenumbers more accurate than frequency.

The relations of the four units can easily be calculated, knowing the constants elementary charge (e=1.602×10^{-34} As) and Planck's constant (h=6.626×10^{-34} Js), or by using scripts as included on the CD enclosed to this work. For a quick estimation, the following relations might prove useful:

1 meV	$\sim$8 cm^{-1}	$\sim$ 240 Ghz
1 cm^{-1}	$\sim$30 Ghz	$\sim$ 0.12 meV
1000 Ghz	$\sim$4 meV	$\sim$ 33 cm^{-1}

The relation between [cm^{-1}] and [nm] relevant for this thesis, is sketched in fig. 1.1, since it is not linear.

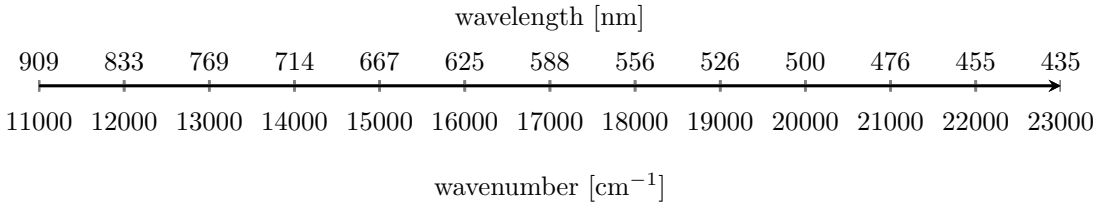

Figure 1.1: Relation of [cm^{-1}] to [nm].

1.3 ... Helium

This section aims to give a short overview of numerous exceptional characteristics of the element helium, the interested reader finds further reading recommendations in the references and at the end of this section.
Helium is the first, i.e. smallest, noble gas in the periodic table. Its closed shell (electronic configuration: $2s^2$) makes it very stable and inert. It has an ionization energy of 24.6 eV (198256 cm^{-1}) and the first allowed transition is $1s2s,^1S \leftarrow 1s^2$, ^1S above 20 eV (166000 cm^{-1} or 60 nm, i.e. far in the UV range) [135]. This means, He is completely transparent in the visible regime (e.g., the first excitation energy lies far above the ionization energies of all alkali and alkaline-earth atoms). These facts make it a very interesting element to use as a matrix in matrix isolation spectroscopy. However, helium is not only spectroscopically interesting: It is the only element that cannot be solidified under ambient pressure. This is valid for both stable isotopes ^{3}He and ^{4}He, but since ^{3}He is exceedingly rare and the present work only deals with ^{4}He, the further explanations are restricted to the ^{4}He isotope if not denoted otherwise. As can be seen in fig. 1.2, a pressure above 25 bar is needed to form solid helium. This is due to the very weak interaction between He atoms. The atoms in a He nanodroplet, for example, are only bound by an energy of 5 cm^{-1} to the droplet [26]. An additional exception of this remarkable element is that He has two liquid phases (below 4.22 K), one of which is superfluid (below the λ-transition at 2.174 K) [48].
Superfluidity defines a fluid state of matter without viscosity and with infinite heat capacity, where pure superfluidity is only reached at T=0 K. The discovery of the superfluid phase of helium was simultaneously published by Allen and Misener [2] and Kapitza [77] in 1938. Different explanations have been developed to account for the behavior of superfluid He in experiments. Most prominent are the two-fluid model [161], defining liquid He below the lambda point (2.174 K) as a mixture of superfluid and normal He, and the quasi-particle model [97] using quasi-particles as an explanation. A detailed description of helium and its characteristics can be found in e.g., ref. [48].
Superfluidity in ^{4}He stems from the fact that He shows a macroscopic quantum mechanical wavefunction. At the λ-transition the De Broglie wavelength of helium (at ambient pressure) becomes larger than the average interatomic distance between He atoms, hence the atoms lose their identity and can be described by one macroscopic wave function [6, 48].
These facts relate superfluid ^{4}He [48] and also helium nanodroplets to Bose-Einstein-condensates (BECs), since both can be described by a macroscopic wavefunction and for both the ideal Bose gas (IBG) provides an underlying theory. Ref. [32] gives a thorough comparison of BECs to He nanodroplets, the following comments are based on this article. At a given temperature the thermal distribution of n_i bosonic particles (integer spin) is given by the Bose statistics:

$$\langle n_i \rangle = \frac{1}{exp(\frac{\epsilon_i - \mu}{k_b T}) - 1} \tag{1.1}$$

Where $\langle n_i \rangle$ is the expected number of particles in the energy level ϵ_i at the temperature T, k_B denotes the Boltzmann constant and μ the chemical potential. Note that an arbitrary number of bosons can occupy the same state. If the temperature is reduced, lower and lower energy states will be occupied by the particles and finally the number of particles in the lowest energy state ϵ_0 will be in the order of the number of all particles - this is called Bose-Einstein condensation. Note that, as will be explained in section 1.6 p22, it is important to consider the temperature and the phase-space density of the sample to reach quantum degeneracy [2]. For this phenomenon a criti-

[2] In contrast to bosons, fermions (half-integer spin) cannot occupy the same quantum state. They are described by Fermi-statistics. Quantum degeneracy for fermions means that the lowest energy levels are all occupied by

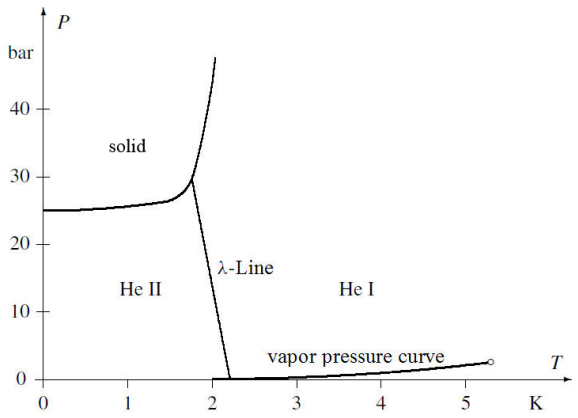

Figure 1.2: Phase diagram of ^{4}He, showing the special characteristics of He at low temperatures. Helium has two liquid phases, where the superfluid phase is denoted as He II (values given for ^{4}He, graphic modified from [48]).

cal temperature can be calculated at which the transition to this new phase happens. The same calculation applied to helium leads to a temperature reasonably close to the actual temperature of the λ-transition for superfluid He. Several other analogies in measured properties between He droplets and BECs are stated in [32], as well as several differences, most prominently the higher particle density in the droplets and the consequently higher particle-particle interaction.
Remarkable is the common theoretical background of both quantum fluids: The theory of the ideal Bose gas also leads to the two-fluid model and thus explains several effects of superfluidity.

The work done on both species fills numerous articles and books. For superfluid He, the corresponding chapter in [48] can be recommended to gain an understanding of the basics of the theoretical treatment, refs. [41, 42, 47] offer a more cursory introduction into the matter and explain some of the fascinating characteristics and experiments with superfluid helium. Ref. [32] deals with the comparison of BECs to superfluidity in detail. A short introduction into the topic of ultracold molecules will also be given in section 1.6 p22 of this work.

one particle. This leads to very different effects for quantum degenerate Fermi and boson gases, e.g. described in ref. [31])

1.4 ... Helium Droplet Beam Generation and Dopant Pickup

The standard method used for the creation of a continuous helium nanodroplet (or cluster) beam is called supersonic jet expansion [126,127,142,143] and has been demonstrated for the first time by Becker et. al. [15] .

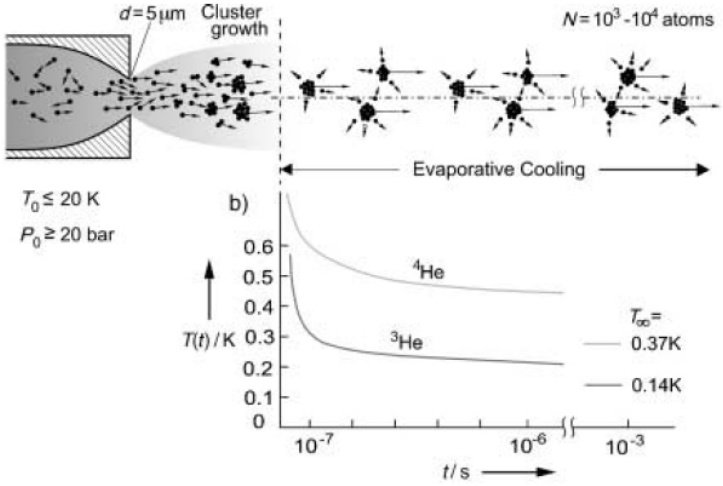

Figure 1.3: Helium droplet beam generation: The adiabatic cooling after the expansion through the nozzle leads to a condensation of the He atoms to clusters, the collisional cooling ceases after a distance of about 1000 times the nozzle diameter. The successive cooling is achieved by evaporating He atoms, taking away excessive energy, leading to a final temperature of 0.375 K (from [163]).

The underlying principle of this method lies in expanding pre-cooled helium gas through a small orifice under high pressure (common 'source conditions' used in the present work are T_0=15 K, p_0=60 bar and d_0=5 μm). The high pressure ensures that the mean free path of the He atoms is smaller than the orifice diameter, which is a crucial condition for this kind of molecular beam. The fast expansion of the helium together with the small mean free path of the gas causes adiabatic cooling. The cooling rate during this process is enormous (10^9-10^{11}K/s [162]) and the temperature of the gas reaches the fluid regime of the He phase diagram (subcritical expansion), i.e. the atoms condense to droplets. This depends on the source conditions and has been investigated e.g., in refs. [22,23]. At the expansion, the gas reaches supersonic speed which causes shock waves [126,127]. These occur laterally (barrel shock) and in beam direction (Mach disk) and compress the beam. The region within these shock waves is called the 'zone of silence'[3]. Close to the nozzle, the beam is viscous due to the high particle density, thus also the particle-particle interaction is high, i.e. a high number of collisions occurs, leading to an effective energy exchange between the particles and very effective cooling (and thus, in the present case to condensation). Farther away from the nozzle the expansion of the gas increases the mean free path and the viscous flow becomes a molecular flow. Here the collisions between the particles cease (at a distance of approx. 1000 orifice diameters[4]). However, the droplets are further cooled by helium atoms evaporating from the droplets and thus taking away excessive energy. The whole process including the corresponding temperature and timescale is given in Figure 1.3, obtained from liquid droplet calculations [19,57]. The initial rate of evaporation decreases

[3] A skimmer used to extract the droplet beam is mounted in the zone of silence.

[4] When describing atomic and molecular beams it is common to give the distance from the nozzle in 'orifice diameters', i.e. the distance from the nozzle divided by the nozzle diameter.

exponentially reaching a finite temperature of 0.37 K for ^{4}He droplets. This temperature has been determined by measuring the Boltzmann distribution of rotational levels of the SF_6 molecule in He droplets [59]. It has been further determined by our group that the surface temperature of the droplet is the same [12].
The average droplet size for the subcritical expansion lies in the order of 10^4 atoms per droplet, larger droplets can be produced by supercritical expansion, but this method is not part of this thesis and will therefore not be discussed here, see ref. [163] for more information. The droplet beam reaches a velocity of 400 m/s in the process and has - due to the special form of creation - a very narrow velocity distribution of $\Delta v/v \approx$0.01-0.03 [163].

1.4.1 Droplet Size Distribution

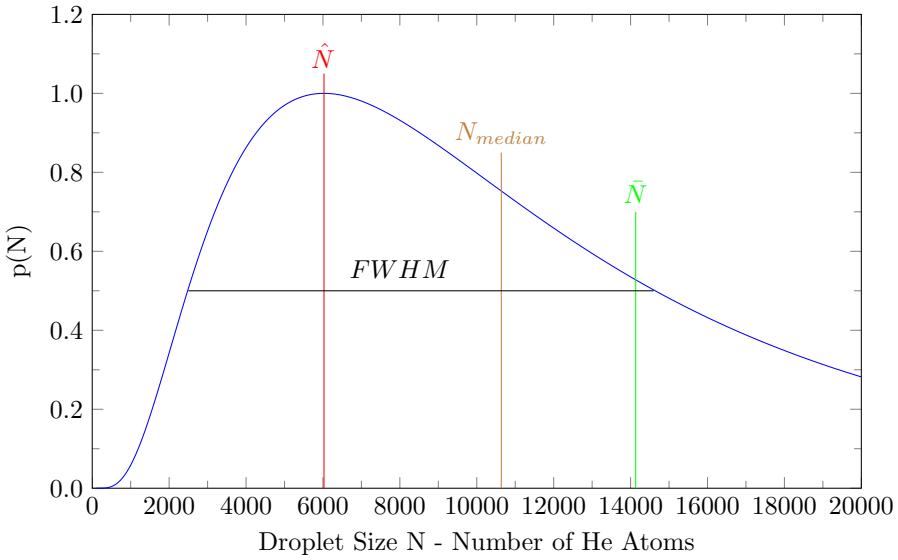

Figure 1.4: Example for the droplet size distribution with the common source conditions used in this work p_0 = 60 bar, $d_0 = 5\,\mu$m, $T_0 = 15$ K. The denoted parameters are the mean droplet size $\bar{N}_{60,15} = 14133$, the median droplet size $N_{60,15,median}$ =10638, the maximum of the droplet size distribution $\hat{N}_{60,15} = 6027$ and the full width at half maximum (FWHM) of the distribution $N_{60,15,1/2} = 12159$.

Obviously not all droplets formed in the supersonic gas expansion have the same size, but are spread statistically. The sizes depend on several He-specific and the three source conditions: The pressure of the helium gas at the nozzle p_0, the temperature of the He before the expansion T_0 and the diameter of the orifice or nozzle d_0. The latter is usually defined by the experimental setup and will not be treated as a variable here. The size distributions for different source conditions have been measured, e.g. by deflection of the droplet beam by a second atomic beam [52, 100] and found to follow a logarithmic normal distribution described by equation 1.2 and shown in fig. 1.4, with the most important parameters of the distribution denoted.

$$p_N(N) = \frac{1}{N\sigma\sqrt{2\pi}} \exp\left(-\frac{(\ln N - \mu)^2}{2\sigma^2}\right). \tag{1.2}$$

N gives the number of He atoms, μ the mean of the function and σ the standard deviation. Several publications list the measured mean droplet sizes $\bar{N}_{p_0,T_0}$ for different source conditions (e.g., [163]). Unfortunately, for spectroscopic investigations the maximum of the droplet size

distribution $\hat{N}$ is the more interesting value, because statistically most droplets in the beam will have this size. Thus, most of the recorded signal (REMPI-TOF or LIF) will originate from droplets with this size. My colleague Florian Lackner dedicated a part of his thesis to this problem [91] and conveniently also gives a solution as well as a list of all relevant distribution parameters for numerous source conditions.
To give a short account: He developed a model which allows to calculate the droplet size distribution for all combinations of temperature and pressure (down to 30 bar). Once the distribution is known, all parameters of the distribution (maximum size, FWHM, median) can be calculated. This means μ and σ have to be determined. In his model, Florian uses the fact that the mean μ of the distribution is a linear function of the temperature and also of the pressure (which only holds down to 30 bar). Thus μ can be obtained from the source conditions pressure p_0 and temperature T_0. The remaining variable σ can be calculated from μ and the mean droplet size $\bar{N}$, using the relation

$$\bar{N} = \exp\left(\mu + \frac{\sigma^2}{2}\right), \tag{1.3}$$

where $\bar{N}$ can be extracted from a fit to experimental data [163] according to the scaling law of Knuth [79].

For the present work the size of the nozzle is $\mathrm{d_0} = 5\,\mu\mathrm{m}$ and a constant pressure of $\mathrm{p_0} = 60\,\mathrm{bar}$ was used. For the investigation of alkali-doped droplets the temperature was altered in order to study droplet-size effects. During the experiments with Ak-Ake molecule doped droplets the temperature was held at a constant value of $\mathrm{T_0} = 15\,\mathrm{K}$. Figure 1.4 shows a graph of the lognormal distribution with these source conditions ($\mathrm{p_0} = 60\,\mathrm{bar}$, $\mathrm{d_0} = 5\,\mu\mathrm{m}$, $\mathrm{T_0} = 15\,\mathrm{K}$). Applying the model of Florian Lackner [91] the following four parameters of the lognormal distribution are obtained:

Mean droplet size	... $\bar{N}_{60,15} = 14133$
Median droplet size	... $N_{60,15,median}$ =10638
Maximum droplet size	... $\hat{N}_{60,15} = 6027$
Full width at half maximum	... $N_{60,15,1/2} = 12159$

The radius of the droplet can be calculated simply from equation 1.4, assuming the droplets are spherical [52].

$$R = \left(\frac{3N}{4\pi n_{LHe}}\right), \tag{1.4}$$

where $n_{LHe} = 2.1 \times 10^{28}$ [43] denotes the number density of liquid helium and N the number of atoms per helium droplet. For the standard source conditions given above, this results in a radius at the average droplet size of $\bar{R} = 5.4\,\mathrm{nm}$ and a droplet radius at the maximum of the distribution of $\hat{R} = 4.0\,\mathrm{nm}$.

1.4.2 Dopant Pickup

With the theoretical knowledge how the droplets are formed at hand, the next interesting question is how to efficiently dope them with the desired species. The doping process is rather straightforward: It simply suffices to let the droplet beam pass through a gas of the dopant

molecules. Depending on the pressure of the gas, the single He droplets pick up a certain number of atoms on average. Several experimental realizations are possible, the one used in our beam apparatus is a simple metal cylinder holding the corresponding alkali or alkaline-earth metal. The vapor pressure needed for a successful pickup is achieved by a resistive heating of the pickup cell. Naturally, the pickup of dopants is also a statistical process and follows a Poisson distribution [101]:

$$P(k|a,n,\sigma) = \frac{(an\sigma)^k}{k!}\exp^{-an\sigma}. \tag{1.5}$$

The equation states that the probability $P(k|a,n,\sigma)$ to pick up k dopant atoms depends on the length of the pickup cell a, the particle density n of dopant atoms in the pickup cell and the pickup cross section σ. The length of the cell is 26 mm in the present case. The pickup cross section can be approximated by the geometrical cross section of the He droplets, which in turn can be calculated from the droplet radius given above. The particle density $n\,[1/m^3]$ can be calculated by assuming an ideal gas $n = p/k_bT$, where k_b denotes the Boltzmann constant and p and T the pressure and temperature in the pickup cell, respectively. These two variables are connected via the vapor pressure. The vapor pressure curve for the materials used in this work is shown in figure 1.5 (a).

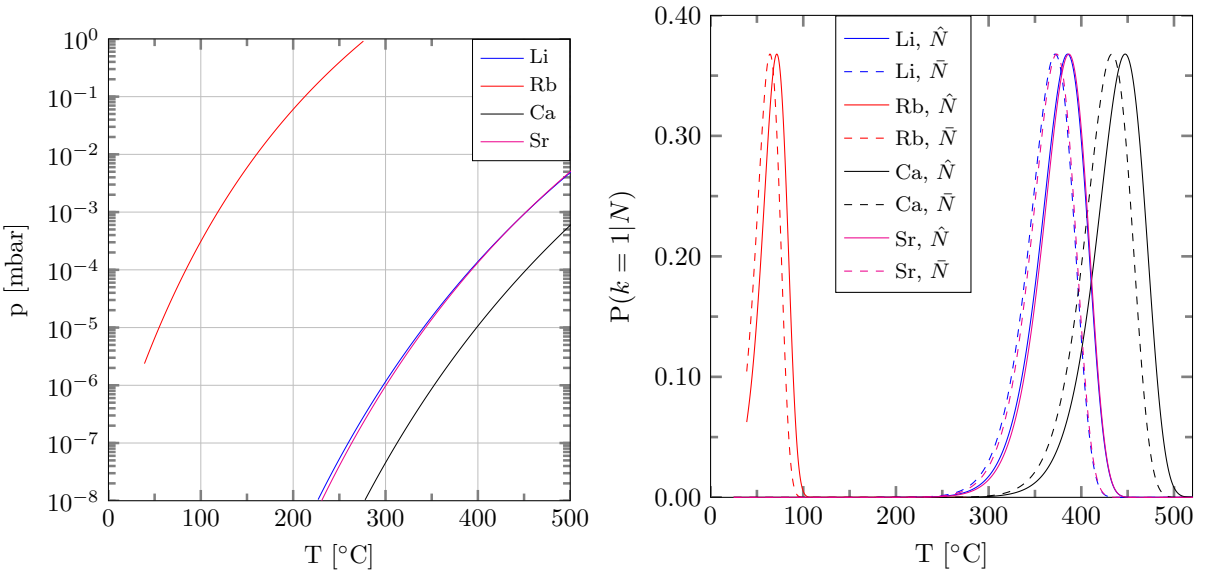

(a) (b)

Figure 1.5: (a) Vapor pressure curves for the materials used in this thesis. Data from [103]. (b) Poisson distribution over pickup temperature for a monomer pickup ($k = 1$) of the denoted materials at the maximum $\hat{N}_{60,15}$ and mean $\bar{N}_{60,15}$ of the droplet size distribution, obtained with the source conditions ($p_0 = 60$ bar and $T_0 = 15$ K) used in this thesis (cf. fig. 1.4).

With all these parameters known, the Poisson distribution for the single elements can be calculated. Figure 1.5 (b) shows these distributions for a monomer pickup ($k = 1$) over the pickup temperature for all materials used in this thesis. For each material the distribution at the mean and maximum droplet size ($\bar{N}_{60,15} = 14000, \hat{N}_{60,15} = 6000$) obtained with the standard source conditions is shown. The pickup maxima for all these materials lie in a pressure range of $10^{-5} - 10^{-4}$ mbar.

The theoretical distribution maxima and the experimentally used temperatures are given in table 1.1. The experimental data have been determined by an optimization for the mixed Ak-Ake molecule signal. For this purpose the ratio between the two vapor pressures is more important than the absolute value. This explains the deviation of the theoretical from the experimental values. For Li, Sr and Rb the experimental values are in the range theoretical maxima, within the experimental uncertainties. Only for Ca the experimental temperature is significantly below the theoretical value.
However, when comparing theoretical and experimental values, several facts have to be considered:

- The temperatures were measured at the pickup cell itself and do therefore not reflect the actual temperature of the material.
- Both Ak and Ake metals form a passivation layer which has to be cracked before the experiments. Depending on the efficiency of this process the ideal temperature may vary.
- The temperatures for Rb are much lower than for the other elements. Here, the main part of the heat transfer is conductance, while in the higher temperature region radiation predominates.
- Rb and Li are fluid at the given temperatures, while Sr and Ca are still solid. This may also account for differences, since e.g., the heat conduction from the pickup cell to a fluid is different than to a solid.

These considerations show that it is important to design the pickup cell and its heating for higher temperatures than theoretically necessary.

Table 1.1: Pickup temperatures, calculated for the maximum of a monomer pickup for $\hat{N}_{60,15} = 6000$ and experimentally determined values.

Material	th. value	exp. value
	C°	C°
Rb	72	80-90
Li	386	340-360
Sr	386	380-410
Ca	447	370-380

Some aspects are worth considering in respect of the successive pickup of two different atoms, such as an alkali and an alkaline earth atom: Each pickup is associated with a shrinking of the droplet. The atom picked up has to be slowed and cooled, i.e. energy has to be dissipated, which happens by the evaporation of atoms from the droplet, where each atom carries away approximately $5\,\mathrm{cm}^{-1}$ of energy [26,101]. The exact process is theoretically challenging to model, see e.g., ref. [111] for calculations on the pickup of a silver atom. Animations of the simulation are given in the electronic supplementary information of the publication and can also be viewed on youtube [110]. For the pickup of Ak and Ake atoms the droplet shrinking is usually in the order of several 100 He atoms [91], since both are surface located and only weakly bound to the droplet.
The fact that both atoms are cooled to the droplet temperature of 0.37 K and the presence of He atoms as scattering partners which carry away the binding energy, allow the formation of molecules - due to the low droplet temperature - in their ground state. This formation again shrinks the droplet according to the binding energy of the molecule. For the Ak-Ake molecules

presented in this work this lies in the range of ∼100-1000 He atoms, thus, the overall droplet shrinking can be neglected in comparison to the size of the droplets in this respect.
Apart from the droplet shrinking it has to be taken into account that both the droplet size and the pickup process obey a statistical distribution, the convolution of both giving a relatively broad function. Hence the probability to pick up dimers along with monomers is quite high. Figure 1.6 shows the calculated monomer (solid line) and dimer (dotted line) pickup distribution for Ca for the maximum droplet size ($\hat{N}_{60,15} = 6000$ - red) and the mean droplet size ($\bar{N}_{60,15} = 14000$ - blue). This behavior is the same for all materials used. It can be seen that the maximum of the dimer pickup for the mean droplet size nearly coincides with the maximum of the monomer pickup for the maximum droplet size. This means that if the doping of the droplets is optimized for a monomer pickup at $\hat{N}_{60,15}$, it is at the same time optimized for a dimer pickup at $\bar{N}_{60,15}$. Especially when investigating Ak-Ake molecules with LIF, this is a large disadvantage since the Ak or Ake dimers might contribute to the fluorescence signal if dimer transitions are excited as well.

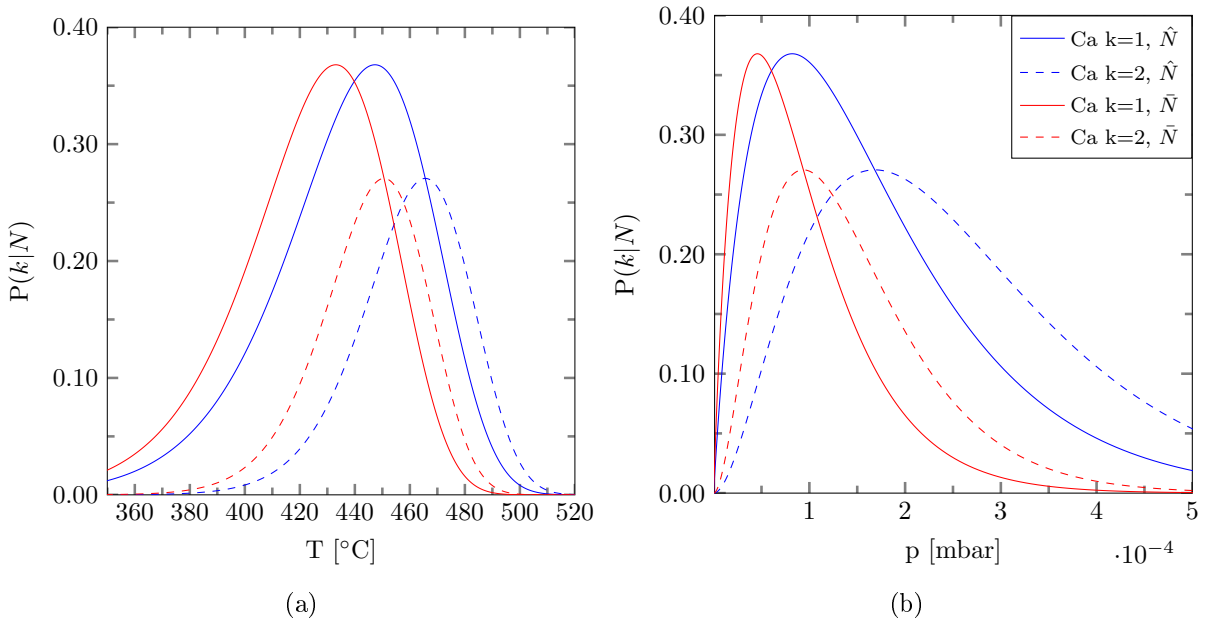

Figure 1.6: Pickup distribution of calcium over temperature (a) and vapor pressure (b) for monomer ($k = 1$) and dimer ($k = 2$) pickup at the mean and maximum of the droplet size distribution ($\hat{N}_{60,15}$, $\bar{N}_{60,15}$).

The best way to prevent this is to lower the temperature of the pick up cells below the monomer maximum. Also, prior recording of molecular transitions with REMPI-TOF spectroscopy (see section 3.1 p42), as performed in this thesis, has proven beneficial, since the mass-resolved spectra allow a temperature optimization for the desired signal (monomer, dimer, molecule). Another option would be to decrease the size of the droplets, by e.g. choosing a higher starting temperature T_0. This leads to smaller droplets and a smaller size distribution. However, this also decreases the pickup cross section on the one hand and on the other hand small droplets might be destroyed by the successive pickup and molecule-formation of the dopants.
A more refined analysis of the pickup processes for Rb has been presented by Florian Lackner [91].

A Note to the Experimentalist:
A recently developed experimental amendment also helps the cause. As explained in the experi-

mental section 2.3.1 p37, the cell temperature of one pickup cell can be recorded as a function of the ion yield during a REMPI-TOF experiment. Thus, by altering the pickup temperature and tracking the signal of the desired mass, one can easily optimize the signal. Only materials which require a low pickup temperature (e.g., all Ak metals) pose a problem, because the response time of the pickup cell to a temperature change on the control is too slow to efficiently optimize a signal. In this case it is recommended to take several mass spectra at different temperatures. It also has to be mentioned that an ideal set of temperatures found in one experiment might not be ideal in another experiment. This can have various reasons: Usually both Ak and Ake metals form an oxide layer which has to be cracked by a slight overheating of the cell. depending on the efficiency of this process, the vapor pressure of the dopant at a given temperature might vary. Additionally, the temperature measurement by the thermocouples is only reliable in a range of about ± 4°C and the actual temperature of the dopant material within the pickup cell is unknown. Also the droplet size distribution might not be exactly the same between two measurements. All these experimental uncertainties speak for a temperature optimization at the beginning of an experiment.

1.5 ... Molecular Spectroscopy

Molecular Spectroscopy is a field that fills several books, as examples refs. [38, 63, 64] can be recommended. The following chapter will merely give the inclined reader enough insight into this wide topic to comprehend the results presented in chapter 4 p49. Fortunately, the molecules investigated in the scope of this thesis are all diatomic, which significantly simplifies the following description.

1.5.1 Quantum-Mechanical Concepts

This section will help to gain a deeper understanding of the energetic structure of a molecule. The explanation is meant to be detailed enough to explain the concept, but also cursory enough not to lose itself in details. It will also provide the basis for the subsequent sections.

Richard P. Feynman once stated that a problem can be understood better by firstly describing it without mathematics before giving the related equations (analogous quotation). According to this statement: The energetic structure of a molecule is more complex than that of an atom, mostly due to the presence of several nuclei and the influence of their configuration and motion on the energy of the whole molecular system. A common approach is to apply some, physically sensible, approximations in order to simplify the system: The nuclei are much heavier than the electrons and hence their dynamics is much slower. Therefore we can assume that we can find a well-defined energy for the electrons for one certain configuration (i.e. position) of the nuclei - which is in the case of the diatomic molecule simply the distance between the two nuclei. Calculating this energy for different sets of the internuclear distance for a certain electron configuration (state) leads to the potential energy curves (PECs) described below (see fig. 1.7), i.e. an energy over the distance of the nuclei. If such a PEC has a minimum it is called a binding state. The energetic minimum of the system is located at the equilibrium distance R_e. This binding state can then be seen as the potential (provided by the electrons) in which the motion of the nuclei takes place (generally vibration and rotation, where the latter is disregarded in the respect of this work).
For large nuclear distances the energy of the PEC will asymptotically approach the energy of the combination of two atomic states, i.e. each PEC corresponds to an atomic asymptote.

The mathematical perspective of the verbal description above is presented in a short version in the following: A molecular system consisting of two nuclei and a number of N electrons can be described by the Schrödinger equation:

$$\hat{H}\Psi = E\Psi, \tag{1.6}$$

where E denotes the total energy of the system, Ψ the total wavefunction and $\hat{H}$ the Hamiltonian. The complete Hamiltonian for a molecular system is not given here, but it is easy to see that it is quite complex: The kinetic energy part of $\hat{H}$ has to take the movements of all electrons as well as those of the nuclei into account and the potential part has to treat the Coulomb-repulsion of the nuclei, the repulsion of the electrons and the attraction of electrons and nuclei.
The Schrödinger equation for a molecular system can only be calculated numerically. Several methods are available, a closer description in the context of Ak-Ake molecules can be found in the Master thesis of Johann Pototschnig [132], who did the theoretical calculations for the present work, further details will be given in his PhD thesis [133].
However, a qualitative understanding can be gained without going too deep into the theoretical

detail[5]. Applying the approximation explained above, i.e. using the fact of the much faster electron dynamics in comparison to the nuclei, we can separate the electronic ϕ and the nuclear χ wavefunction ($\Psi = \phi\chi$). If we disregard every interaction between the nuclear and the electronic wavefunctions we can also separate the Schrödinger equation. This is called the Born-Oppenheimer (BO) approximation and leads to two equations separately treating the electrons and the nuclei:

$$\hat{H}_0\phi_n(\vec{r}) = E_n^0(R)\phi_n(\vec{r}) \tag{1.7}$$

$$(\hat{T}_k + E_n^0(R))\chi_{n,\nu}(\vec{R}) = E_{n,\nu}\chi_{n,\nu}(\vec{R}) \tag{1.8}$$

Equation 1.7 represents the electronic Schrödinger equation. The wavefunction of the electrons $\phi_(\vec{r},\vec{R})$ (in a certain electronic configuration $|n\rangle$) depends on the position of the nuclei $\vec{R}$ but not on their motion. The Hamiltonian H_0 only contains the kinetic energy of the electrons and the potential energy provided by the nuclei. This leads to the same conclusion as given in the beginning of this section: Since there is one defined energy value $E_n^0(\vec{R})$ for every electron configuration $|n\rangle$ and nuclear configuration $\vec{R}$, the calculation of these energies for a set of values for the internuclear distance $\vec{R}$ will lead to the potential energy curve for the given electron configuration (see fig. 1.7). $E_n^0(\vec{R})$ can be seen as the potential provided by the averaged electron distribution for different distances of the nuclei [6].

Equation 1.8 represents the nuclear Schrödinger equation. χ_n denotes the wavefunctions of the nuclei. The equation basically describes the motion of the nuclei ($\hat{T}_k$ is the operator of the kinetic energy of the nuclei) in the potential provided by the electrons $E_n^0(\vec{R})$. This means that the averaged kinetic energy of the electrons $E_n^0(R)$ in the configuration $|n\rangle$ (basically one potential energy curve in fig. 1.7) can be seen as a potential in which the motion of the nuclei takes place. For each electronic state ϕ_n, several nuclear wavefunctions $\chi_{n,\nu}$ with the energy $E_{n,\nu}$ can be found, corresponding to the vibrational wavefunctions and energies belonging to the electronic configuration $|n\rangle$.
This provides a quantum mechanical explanation of what will be shown below.

1.5.2 Potential Energy Curves

Figure 1.7 shows the theoretically calculated potential energy curves (PECs) for the RbSr molecule. The quantum-mechanical origin of these PECs has been discussed above, the actual calculations make use of intricate numerical techniques. Some concepts will be presented in the PhD thesis of Johann Pototschnig [133] who provided the calculations shown in figure 1.7. The principles of molecular spectroscopy relevant for this thesis can be explained on the basis of this figure.
We introduced the development of the PECs with the help of a qualitative quantum-mechanical description in the section 1.5.1 p13, here we will only consider how to read and understand a PEC. The PEC diagram shows the interaction energy of the two atoms (e.g., Rb and Sr) for different separations of the nuclei R. For large internuclear separation this converges to the energy levels of the separated atoms. At a distance of $R = 0$ the energy becomes infinite

[5] Note that interactions related to the electronic or nuclear spin are not considered here and can only be calculated in a relativistic model (mentioned in the context of SO couplings in section 1.5.6 p19).

[6] Note that for the calculation of potential energy curves for this work (by Johann Pototschnig), e.g. fig. 1.7, only equation 1.7 has been solved numerically.

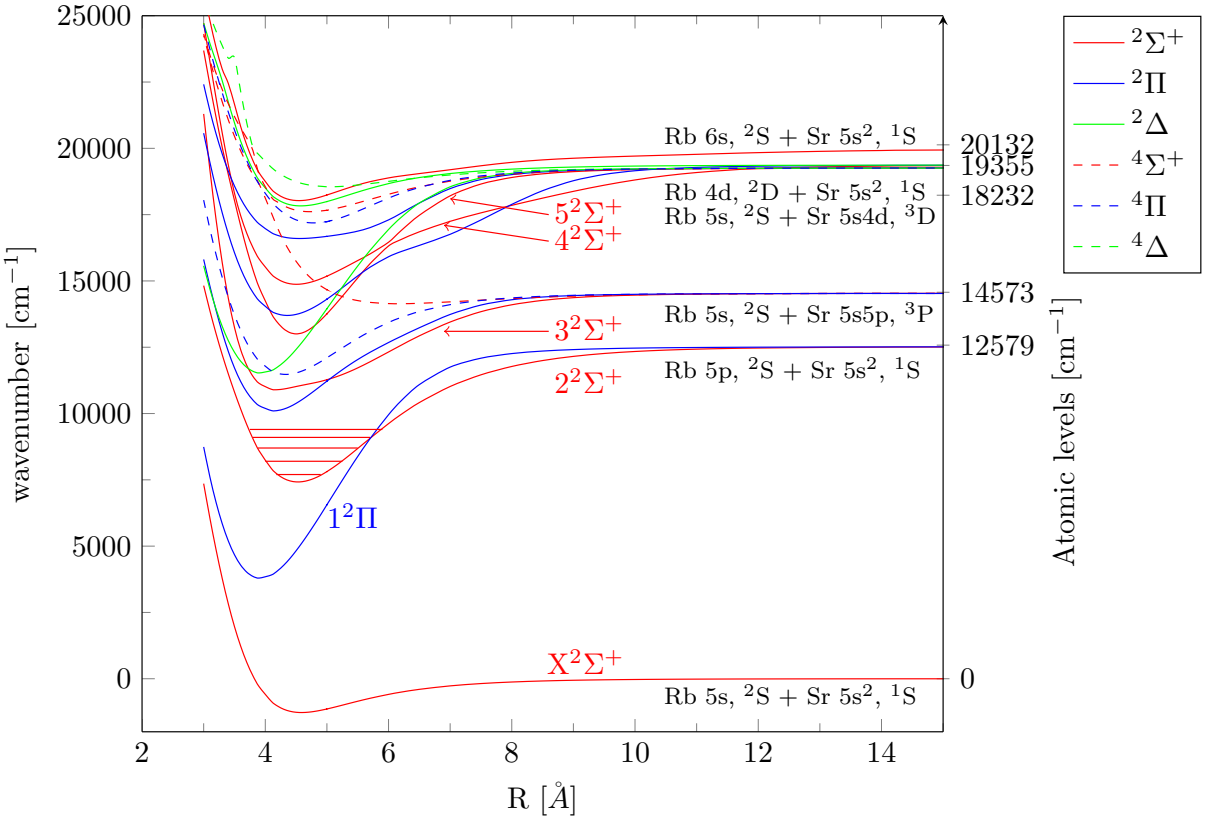

Figure 1.7: Example of molecular potential energy curves for RbSr as calculated for the publication ref. [87]. All values are given as calculated, the vibrational levels in the $3^2\Sigma^+$ state are only sketched. The line style denotes the multiplicity (solid-doublet, dashed-quartet) and the color the projection of the orbital angular momentum Λ (Σ-red, Π-blue, Δ-green). SO coupling has not been taken into account in the calculations.

due to the Coulomb repulsion. As explained in detail above, every point between these two extremes gives the interaction energy at the corresponding distance, leading to the potential energy curve. If the PEC contains a minimum, it is a binding state, otherwise it is repulsive. Each combination of atomic energy levels splits into several molecular levels - table 1.2 shows this on the example of RbSr. Please note that only states relevant for the explanation of this thesis are shown, higher excitations as well as atoms with a more complex electronic structure lead to more complex molecular structures, see e.g., ref. [38] for a more thorough treatment. The experimental spectrum is simplified by the fact that not all of the states are accessible from the ground state due to selection rules for the transitions (see below), states which cannot be reached from the ground state are grayed out in table 1.2.

Table 1.2: Rb and Sr atomic states and their corresponding RbSr molecular states, given in the Hund's case (a) notation without SO interaction. States which cannot be reached from the ground state are grayed out. A closer description of the notation is given in the text below.

Rb	**Sr**	**RbSr**
$5s^1\ ^2P$	$5s^2\ ^1S$	$X^2\Sigma^+$
$5p^1\ ^2P$	$5s^2\ ^1S$	$2^2\Sigma^+$
		$1^2\Pi$
$5s^1\ ^2S$	$5s^15p^1\ ^3P$	$3^2\Sigma^+$
		$2^2\Pi$
		$1^4\Sigma^+$
		$1^4\Pi$
$4d^1\ ^2D$	$5s^2\ ^1S$	$4^2\Sigma^+$
		$3^2\Pi$
		$1^2\Delta$
		$2^4\Sigma^+$
		$2^4\Pi$
		$1^4\Delta$

1.5.3 Spectroscopic Denotation

The denotation used to describe the molecular states of RbSr in table 1.2 is called Hund's case (a) notation, where the spin-orbit coupling has not been taken into account [7]. The Hund's coupling cases reflect the coupling strengths of:

- the total orbital angular momentum $\vec{L}$ to the internuclear axis (imaginary axis connecting both nuclei, commonly labeled as z-axis)
- the spin-orbit (SO) coupling - orbital $\vec{L}$ to spin (angular momentum) $\vec{S}$
- the rotational angular momentum $\vec{R}$ to $\vec{L}$ and $\vec{S}$

For the present cases only the first two couplings and only the Hund's cases (a) and (c) are relevant.

Hund's case (a) is sketched on the left side of fig. 1.8. Here, the coupling of $\vec{L}$ and $\vec{S}$ to the molecular axis z is stronger than the SO coupling, i.e. both $\vec{L}$ and $\vec{S}$ independently couple to the molecular axis z. The projection of $\vec{L}$ and $\vec{S}$ onto z is denoted with Λ and Σ, respectively. The values of Λ are (analogue to the notation for $\vec{L}$) expressed in Greek letters: $\Lambda = 0, 1, 2, ... \hat{=} \Sigma, \Pi, \Delta, ...$ The multiplicity $(2S + 1)$, giving the number of SO split states, is denoted as a prefix superscript. If the spin-orbit interaction is taken into account, the absolute value of Λ and Σ is denoted as $\Omega = |\Lambda + \Sigma|$ as a subscript, resulting in the notation for a molecular state:

$$X^{2S+1}\Lambda_\Omega \tag{1.9}$$

The preceding X labels the number of the state in energetic order, where the ground state is denoted by a 'X' and the successive states by numbers, as indicated for some states in figure 1.7 (convention used in this work, they may also be labeled with letters). The superscript + at the Σ^+ states originates from the parity of the atomic states involved in the molecular states.

[7] As mentioned in section 1.5.1 p13, a treatment of the spin-orbit interaction would require a relativistic approach, which has not been necessary to explain most of the results of the experiments. SO coupling has to be mentioned here to give a thorough description of the Hund's cases.

Hund's case (c) is sketched on the right side of fig. 1.8. Here the SO coupling is strong, hence $\vec{L}$ and $\vec{S}$ couple to a total electronic angular momentum $\vec{J}_a$ which in turn couples to the molecular axis z . In this case the only good quantum number is Ω, which makes the description of states a little confusing. In complete relativistic treatments of diatomic molecules (e.g. ref. [81]) the states are numbered in energetic order and Ω is given in brackets:

$$n(\Omega) \tag{1.10}$$

Taking the rotational angular momentum into account may lead to a splitting of the states which is then denoted by a superscript plus or minus, e.g. $1(0^+)$.

A thorough (and historical) discussion of Hund's cases and their denotations is given in refs. [64, 116]. Note that Hund's case (c) is only relevant for the explanation of the RbSr emission spectra. For the sake of completeness, it should be noted that in order to obtain the total angular momentum $\vec{J}$ of the molecule, for every Hund's case the rotational angular momentum of the molecule $\vec{R}$ has to be taken into account.

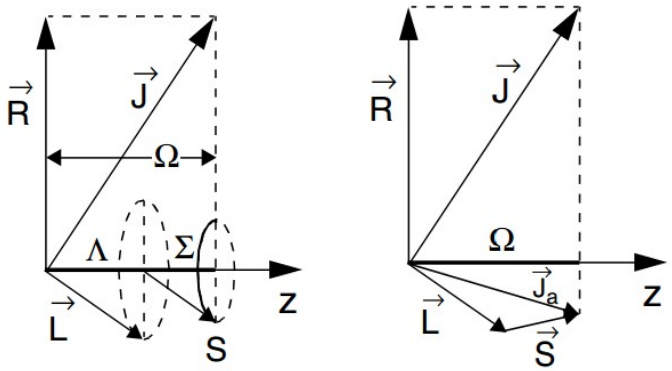

Hund's case (a) Hund's case (c)

Figure 1.8: Hund's coupling cases (a) and (c). The following parameters are given: The total spin angular momentum $\vec{S}$, the total orbital angular momentum $\vec{L}$ and the total angular momentum $\vec{J}$, as well as their respective projections onto the molecular axis z: Σ, Λ and Ω and the rotational angular momentum $\vec{R}$ of the molecule (from [38]).

1.5.4 Selection Rules

Similar to atoms some selection rules apply to molecular transitions:

- $\Delta\Lambda = 0, \pm 1$
- $\Delta\Omega = 0, \pm 1$
- $\Delta S = 0$

Each of this rule holds whenever the respective quantum number is good. Hence all three rules hold for Hund's case (a) but only the second for Hund's case (c), since only Ω is a good quantum number. Some rules also apply for vibrational and rotational transitions, but they are not considered here.
Taking these rules into account, not all states given in table 1.2 can be reached from the ground states, those which cannot be reached have been grayed out.

1.5.5 Vibrations, Rotations and Transition Probabilities

Apart from the additional electronic molecular states in comparison to atoms, it is important to consider the additional degrees of freedom of a molecule: Both its vibrational and rotational movement are quantized and result in a subset of energy levels for each electronic molecular state.
Vibrational excitations are in the infrared region, they are labeled with a quantum number ν. For a transition, ν'' denotes the vibrational levels in the lower (electronic) state and ν' those in the upper electronic state. Some vibrational levels have been sketched for the electronic $3^2\Sigma^+$ state in figure 1.7 (not to scale).
Rotational excitations are in the microwave region, no such states have been resolved in the course of this work, hence they are not explained here.

Transition Probabilities

While the sections above describe the different molecular states and their denotation, transitions between these states are not considered. The following gives a description of vibronic (coupled electronic and vibronic) excitations and their transition probabilities. In the context of this work, pure vibronic transition within one electronic state have not been excited, so they are not treated here explicitly.

As explained in section 1.5.1 p13, the wavefunctions for the electrons ϕ_{el} and the nuclei $\chi_{n,\nu}$ can be separated, within the BO approximation.

Electronic Part of the Transition:
Considering the electronic wavefunction, the probability for the transition of a molecule from one electronic state $|m\rangle$ into another $|n\rangle$ is described by the absolute square of the electronic transition dipole moment (TDM) $\left|D^{el}_{mn}\right|^2$, where the electronic dipole moment

$$D^{el}_{mn} = \int \phi_m(\vec{r}, R) \sum_i (e\vec{r_i}) \phi_n(\vec{r}, R) d\tau_{el} \tag{1.11}$$

depends on the dipole moment of the i electrons ($\sum_i e\vec{r_i}$). $\phi_m(\vec{r}, R)$ describes the electronic wavefunction, R denotes the distance between the nuclei and $\vec{r} = [\vec{r_1}, \vec{r_2}, ...]$ the positions of the electrons. The function is integrated over the space coordinates of the electrons τ_{el}.

Vibrational Part of the Transition:
Similar to the mathematical treatment of electrons in single atoms, the nuclear wavefunction can be separated into a radial part χ_ν (vibrational motion) and an angular part χ_r (rotational motion), where the latter is disregarded here. The transition probability from one vibrational band to another is then given by the integral:

$$q_{mn,\nu',\nu''} = \left| \int \chi_{m,\nu}(\nu'') \chi_{n,\nu}(\nu') dR \right|^2 \tag{1.12}$$

where the nuclear wavefunctions of the two vibronic states involved in the transition are given by $\chi_{m,\nu}(\nu'')$ and $\chi_{m,\nu}(\nu')$. This is called the Franck-Condon-Factor (FCF).

Transition Probability:
Putting these two components together, the transition probability for a vibronic transition of a

molecule is given by the absolute square of the transition dipole moment (TDM) and the FCF $q_{\nu',\nu''}$, written as:

$$\left|D^{el}_{mn}(R_{\nu'',\nu'})\right|^2 q_{mn,\nu',\nu''}, \tag{1.13}$$

where the first gives the strength of the electronic transition[8] and the second the probability for the vibrational transition. A more refined calculation according to this principle results in the transition probabilities given in the results for LiCa, RbSr and RbCa in form of colored bars in the excitation spectra, see sections 4.1 p51, 4.3 p67 and 4.5 p87. In this respect, the FCFs for transitions into a range of upper vibrational levels are calculated, resulting in a band of transitions. The distributions and relative strengths of the calculated transition probabilities can then be compared with the experimental results.

1.5.6 Perturbations

Some details of figure 1.7 cannot be explained by the simple picture provided in section 1.5.1 p13. A closer look shows some irregularities, e.g., slight kinks in the PECs of the upper $^2\Pi$ and $^2\Sigma^+$ states. These arise from interactions between different electronic states. The interactions depend on the symmetry of the electronic states and on their distance from each other. Due to the latter, they mainly occur for electronically excited molecular states, since the distance between electronic states to each other decreases for higher excitations (cf. fig. 1.7).

Electrostatic Interactions - Avoided Crossings

Two electronic molecular states can show an avoided crossing if they have the same quantum numbers Λ, Σ and S and their energetic distance decreases. This interaction of electronic states prevents that the two potential energy curves cross, hence the name 'avoided crossing'. At points where these two states come close to each other, they are both deformed. In the example of RbSr, an avoided crossing can be observed for the $4^2\Sigma^+$ and the $5^2\Sigma^+$ state at an internuclear distance of $R_e \approx 6\,$Å, see figure 1.7.
It is important to consider that at an avoided crossing the character of the molecular wavefunctions change. On the example of the RbSr $4^2\Sigma^+$ and the $5^2\Sigma^+$ state: The $4^2\Sigma^+$ PEC asymptotically approximates the Sr 5s4d ^{3}D state and the $5^2\Sigma^+$ asymptotically approximates the Rb 4d ^{2}D state. At $R_e \approx 6\,$Å they are very close to each other and experience an avoided crossing (slight kink in both PECs). At this point, the wavefunctions describing both states are strongly mixed. For smaller internuclear distances ($R_e <$ Å) the energy between the PECs increases. Here the wavefunction describing the $4^2\Sigma^+$ state shows a larger contribution of the Sr 5s4d ^{3}D orbital. For large internuclear distances ($R_e >$ Å) the wavefunction describing the $4^2\Sigma^+$ state shows a larger contribution of the Rb 4d ^{2}D orbital.
A detailed description on the example of LiF is given in ref. [72].

Spin-Orbit Coupling

A mathematical treatment of the SO coupling requires a relativistic model, however, a qualitative picture is provided by the Hund's cases. Note that the strength of the interaction has to be considered in order to apply the correct Hund's case. In any case, the interaction of the angular

[8] The dependence of the electric dipole moment on the distance of the nuclei has been added in equation 1.13 for the sake of completeness. Mathematically this is treated in the R-Zentroid approximation and is not explained in detail here. See [38] for more information.

momentum of the electrons and their spin will lead to a splitting of the electronic molecular states.
On the example of the LiCa $3^2\Pi$ state, taking the SO coupling into account in Hund's case (a) will lead to a splitting into two sub-bands $3^2\Pi_{1/2}$ and $3^2\Pi_{3/2}$ ($\Omega = |\Lambda + \Sigma| = |1 \pm 1/2|$).
In case of Hund's case (c) the term 'spin-orbit splitting' is not accurate, a relativistic treatment leads to different PECs for the molecule, which relate to the Hund's case (a) PECs but are not the same.
The size of the splitting depends on the (atomic) spin-orbit constant A. Effects of the SO coupling have been observed for LiCa and it has been necessary to include SO coupling (Hund's case (c)) for the description of the RbSr emission spectrum, see section 4.3.7 p79.

Predissociation

Predissociation refers to the dissociation of a molecule upon the excitation into a binding electronic state. The concept is easier to understand by taking RbSr as an example (see fig. 1.7). The $5^2\Sigma^+$ state serves as an example for an excited binding state, as can be seen in the figure, it is crossed by the $1^4\Sigma^+$ state (red, dotted line). An interaction of the two states ($5^2\Sigma^+$ and $1^4\Sigma^+$) may lead to a 'predissociation' of the RbSr molecule upon the excitation of the $5^2\Sigma^+$ state. The rate of predissociation depends on the interaction of the two crossing states, the maximum of this interaction occurs at the point of intersection. Note that, even though the $1^4\Sigma^+$ state is (weakly) bound, the part of the potential where it crosses the $1^4\Sigma^+$ state is not bound and may lead to predissociation. However, on He droplets it is also possible that some molecules relax into the vibrational ground state of the $1^4\Sigma^+$ state. A detailed discussion of predissociation cases can be found in refs. [99,117]
In the present work, predissociation of Ak-Ake molecules, e.g. explains the occurrence of atomic fragments upon certain molecular excitations (see section 4.1 p51)

1.5.7 Alkali-Alkaline Earth Specific

Applying the selection rules above to the states given in table 1.2 reduces the possible final states from a transition of the $X^2\Sigma^+$ ground state to $^2\Pi$ and $^2\Sigma^+$ states. As shown in table 1.2, only doublet ($\Sigma = 1/2$) and quartet ($\Sigma = 3/2$) states arise from the combination of the alkali doublet and the alkaline earth singlet or triplet system, respectively. The quartet states cannot be reached from the doublet ground state, but may cause predissociation (see LiCa 4.1). The same is valid for Δ states, which cannot be reached from the Σ ground state. This leads to a rather clear spectrum for the Ak-Ake molecules.

1.5.8 The Interaction Potential of Experiment and Theory

As will be shown in the results section, an unambiguous assignment of the single peaks to molecular transitions in a recorded spectrum is hardly possible by experiment alone. Theoretical physicists use various calculation methods to approach the energetic structure of a molecule from the theoretical side. All PECs given in the results section, including that for RbSr in fig. 1.7 have been calculated by Johann Pototschnig. A description of the theoretical methods and their working principle will be given in his thesis. A short overview of the used methods is given in the theory section of the LiCa publication [88]. From these theoretical calculations arise the potential energy curves of the respective molecule as well as other important parameters such as the Franck-Condon-factors and the transition dipole moments for the single transition.
These theoretical results are usually more extensive than experimental results, but cannot be

tested for their correctness without the latter. From a spectrum of a molecule several parameters can be extracted, depending on whether the rotational and vibrational structure are resolved and how many lines are resolved. For the present case of Ak-Ake molecules on He droplets, as noted above, only vibrational lines could be resolved for certain states. In the case of a resolved state, the progression of energies for the single vibrational levels can be fitted to the function given in eq. 1.14 [64]. The equation results from the solution of the Schrödinger equation with a Morse potential. The anharmonicity of the potential results in an additional (quadratic) factor in the energy eigenvalues:

$$T(\nu') = T + \omega_e \left(\nu' + \frac{1}{2}\right) - x_e\omega_e \left(\nu' + \frac{1}{2}\right)^2 \tag{1.14}$$

A least-squares fit of the experimentally obtained energy values for a series of vibrational transitions to this function gives the molecular parameters: Excitation energy T_e (energy between the absolute minima of the two potentials), harmonic constant ω_e and anharmonicity $x_e\omega_e$. These parameters can then be compared to the theoretical results. Theoretically, knowing the anharmonicity $x_e\omega_e$ would allow to calculate the equilibrium distance of the nuclei R_e, but since only few vibrational lines were available in the present results, the uncertainty for $x_e\omega_e$ was too large to obtain reliable results.

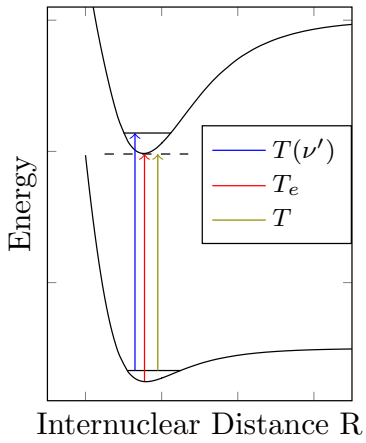

Figure 1.9: Schematics of different molecular parameters explained in the text.

Please note that different values for T can be given (see fig. 1.9): $T(\nu')$ usually refers to the energy between the zero point energy (vibrational ground state) of the lower and the given vibrational level of the upper molecular state, which is the value obtained in experiments[9]. T is the energy between the vibrational ground state of the lower state $\nu'' = 0$ and the absolute minimum of the upper state PEC. To obtain the energy between the minima of both PECs T_e from $T(\nu')$ the energy of the vibrational ground state ($\nu'' = 0$) has to be subtracted. This is usually done for a better comparison to theoretical calculations.
In the case of unresolved spectra the experimental results can still be used to draw qualitative conclusions about the molecular structure and the correctness of the theoretical results.

[9] For $\nu' = 0$, $T(\nu')$ may also be given as T_0, denoting the energy difference between the zero point energies of the upper and lower molecular state.

1.6 ... Cold and Ultracold Molecules

Since the molecules investigated in the course of this thesis are in the spotlight of ultracold molecular physics, this section will give a short and cursory introduction into this field. The main focus will be on the connection to spectroscopy on helium droplets, and some reasons for the interest in ultracold molecules, their application and their creation will be presented. Readers interested in a more thorough discussion of the subject are referred to the book in ref. [166], or reviews in refs. [27, 141, 164].

At first some definitions have to be given for clarification: In this respect 'cold' refers to temperatures in the range of ($1\,\mathrm{K} > T > 1\,\mathrm{mK}$), while ultracold means temperatures ($T < 1\,\mathrm{mK}$) [10]. Another important parameter is the phase-space density ρ. As the name implies, it is the density of states in phase-space (of momentum and position), therefore it is a measure of both the spatial density and the momentum (and thus temperature) of the single particles in the sample. This makes it a convenient parameter, since for the creation of quantum degenerate gases not only low temperatures, but also a sufficient spatial density of the sample is necessary. For a gas of cold atoms ρ is defined by [166]:

$$\rho = n\lambda_{dB,th}^3, \tag{1.15}$$

where n denotes the spatial density of atoms and $\lambda_{dB,th}$ the thermal de Broglie wavelength. The latter can be seen as the average de Broglie wavelength of the gas particles of a sample at a certain temperature. While the particle de Broglie wavelength is defined as $\lambda_{dB,p} = h/p$, for the thermal de Broglie wavelength the momentum of the particles p is replaced by the kinetic energy of the particles $E_{kin} = p^2/2m$. Additionally considering the average kinetic energy of free particles leads to:

$$\lambda_{dB,th} = \frac{h}{\sqrt{2mE_{kin}}} \overset{E_{kin}=3/2k_bT}{\rightarrow} \frac{h}{\sqrt{3mk_bT}} \overset{E_{kin}=1/2m\bar{v}^2}{\rightarrow} \frac{h}{m\bar{v}}, \tag{1.16}$$

h and k_b denote the Planck and Boltzmann constant respectively, m the mass of a particle and $\bar{v}$ the average particle velocity. This shows quite distinctly that ρ can be increased by either increasing the density of particles n or decreasing their average velocity $\bar{v}$ and hence temperature T.
$\lambda_{dB,th}$ also provides a measure for the range where quantum effects begin to dominate: This is the case when $\lambda_{dB,th}$ becomes in the range of the mean free path of the particles. In other words, in this region $\lambda_{dB,th}^3$ is on the order of the spatial density of atoms n and the phase-space density ρ near unity. Indeed, the transition to a BEC for a non-interacting gas happens at $\rho = \xi(3/2) \approx 2.6$. The phase-space density of a gas at room temperature is in the order of $\sim 10^{-17}$. To steer ρ over ~17 orders of magnitude is a challenging procedure, still BECs have been experimentally achieved in 1995 [5, 18, 35]. This was definitely an important event in the upsurge of cold and ultracold atom and molecular physics and was eventually even acknowledged by the award of the Nobel prize to Cornell, Ketterle and Wieman. This field has considerably grown in size since then and has produced a remarkable amount of valuable publications, a fact that only highlights that this is an important, intriguing and ongoing field of study.
An important step which led to this development and allowed access to the ultracold range came

[10] In some cases, to be physically correct, no actual temperature could be assigned to the system (if no thermodynamic equilibrium is reached), in such cases the temperature is used to describe the kinetic energy of the system, via the Maxwell-Boltzmann distribution of the velocities of the particles ($E_{kin} \approx k_bT$) [141, 166].

with the invention of the laser and the realization of the interaction between light and particles, leading to the methods of laser cooling and trapping. Although this is a very interesting topic itself, it would go beyond the scope of this work to deal with it in detail, hence, the inclined reader is again referred to literature such as ref. [166].
Laser cooling makes use of the fact that photons carry a momentum which can be used to apply a force on atoms. The search for an efficient cooling method for atoms has been going on for a long time, initially to achieve high resolution spectra by lowering the effect of Doppler broadening. However, most methods engaged before laser cooling had the disadvantage of reducing the number of atoms in the sample (phase-space density), leading to a lower signal. With laser cooling it is possible to lower the temperature of the atomic sample without changing the number of atoms, allowing to achieve cold samples with a high phase-space density[11]. This opened a whole new field in physics known as 'laser cooling and trapping' and has led to several research divisions:

- The aforementioned achievement of a *BEC* is mostly realized with laser cooling and trapping[12].
- Ultracold samples can be used for research in the *ultracold collision regime*. Here systems can be probed during the collision due to the long interaction time of the cold atoms.
- *Optical traps* only work for atoms which have a low enough energy to be held by small potentials but are essential for many experiments in the field of cold and ultracold atoms.

Based on the initial idea of achieving high resolution spectra by cooling atoms, the same scheme can be applied to molecules. The richness of molecular characteristics in comparison to atoms, such as the additional degrees of freedom, resulting in rotational and vibrational motion, allows for a wealth of new experiments. Several review papers, e.g. refs. [27,141], give whole lists of current and future applications of cold and ultracold molecules. They span from new ideas to create new atomic or molecular lasers [27] over high-resolution spectroscopy [168] to advances in quantum computation [37]. Most suggested applications make use of quantum control, for instance, ultracold molecules can be trapped in optical lattices and single interactions of molecules can be investigated. Furthermore, it may be possible to coherently control the collisions of ultracold molecules. Additionally, ultracold molecules allow efficient population transfer between different molecular quantum states [27]. These facts lead to the new field of ultracold chemistry [85].
However the complexity of molecules also complicates the cooling process. The common closed transition cycles used to laser-cool atoms can generally not be applied to molecules due to their complex energy level structure [141]. Nevertheless, plenty of methods have been developed to cool molecules to cold and even ultracold temperatures. In short:

Direct cooling methods:
These methods shall only be mentioned for completeness. The most prominent methods are sympathetic cooling methods (e.g. buffer gas cooling) and Stark magnetic field deceleration. Basically, they rely on a direct slowing of molecules with the help of other atoms, electric, magnetic or optical fields. For detailed information see [27]. These methods are not limited to atoms which can be caught in laser traps but only lead to temperatures in the cold regime and to low phase-space densities. It is interesting to mention that He droplets can also be grouped in this category, since they can be used to efficiently cool versatile dopant atoms down to the droplet temperature of 0.37 K.

[11] This requires a careful selection of atomic transitions to use in the cooling process.
[12] Other methods to create BECs are possible, see ref. [49] and [44].

Indirect cooling methods:
These make use of the effective cooling schemes developed for atoms and associate ultracold atoms to ultracold molecules. With these methods it is possible to reach much lower temperatures and high phase-space densities, so that even molecular BECs become possible (further cooling steps are necessary for this, see below). However, this also restricts these methods to a handful of atoms, since only few species can be laser-cooled and trapped due to the requirements set by the experimental methods [131]. Consequently, this also limits the selection for the creation of ultracold molecules to alkali metal atoms and a few other species such as Sr [150] and Ca [84]. The key terms in the concept of indirect cooling methods are photo-association and magneto-association (via Feshbach resonances) and further cooling with coherent population transfer methods (e.g. STIRAP) [33, 123, 124, 165]. A short overview of the concepts of these methods is given below.

1.6.1 Photo-Association (PA)

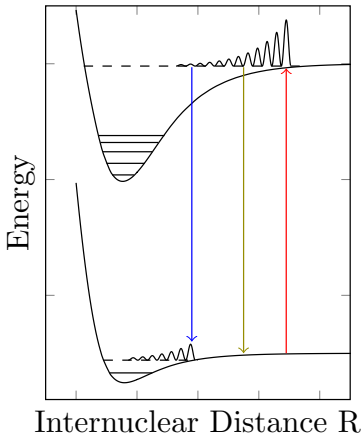

Figure 1.10: Concept of photo-association: An excitation of two atoms close to each other may lead to the formation of a molecule in an excited state, the excited molecule can either dissociate into to atoms or relax into its bound molecular ground state.

The collision of two atoms only leads to the formation of a molecule if they have a binding potential and if the excess energy resulting from the molecule formation can be carried away. On He droplets this is done by evaporating He atoms, but it is also possible to use a photon [74,164]:

$$A + B + h\nu \rightarrow (AB)^* \tag{1.17}$$

In this simple equation, the sum of the photon energy and the kinetic energies of the atoms must add up to the transition energy of the molecule. The absorption of the photon therefore leads from two atoms with a thermal energy E_{th} to an excited molecular state $(AB)^*$, depicted in figure 1.10. The excited molecule will then quickly decay and either dissociate into two atoms again or decay into its bound electronic ground state, indicated by the blue decay arrow in figure 1.10. This is called a radiative stabilization process and can be described by:

$$(A + B)^* \rightarrow AB + h\nu' \tag{1.18}$$

This scheme is widely used to associate two ultracold atoms to an ultracold molecule (e.g., LiCs [36]), as illustrated in the reviews in ref. [74,164]. In the case of ultracold atoms, the probability to find two atoms at a close enough interatomic distance to apply photo-association is particularly high. However, the drawback of this method are the high radiative losses at the relaxation of the excited molecule. The efficient application of this method requires a detailed knowledge of the energy level structure of the atoms as well as of the molecule, since both the association and the radiative stabilization depend on the Franck-Condon windows between ground and excited states [27]. As explained in ref. [27], a profound knowledge of the molecular structure might reveal possibilities to enhance the formation of bound molecules, since irregularities in the molecular potential, such as avoided crossings, may cause an advantageous overlap of the excited and ground state wave function.

1.6.2 Magneto-Association (MA)

MA uses a so called 'Fano-Feshbach' resonance to form a weakly-bound Feshbach molecule from single atoms with the help of a sweeping magnetic field. KRb [123] has been successfully brought to the ultracold temperature range with this method (and subsequent STIRAP, see below). Feshbach resonances are a widely used concept in ultracold physics and several reviews deal with this subject, e.g. refs. [29,80]. Especially ref. [29] provides a good and understandable overview and gives several useful references to related topics in ultracold physics.

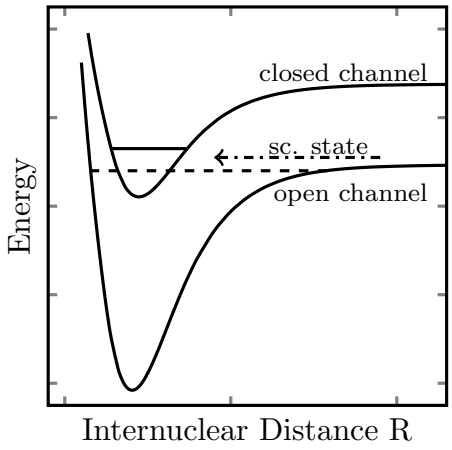

Figure 1.11: Concept of magneto-association: Tuning over the Feshbach resonance of a molecule couples the bound state of the closed channel with the scattering state of the open channel, leading to the formation of a weakly bound Feshbach molecule.

The following gives a short account of the physical principle, following the line of argument in [29]: Fig. 1.11 shows the overlapping potential energy curves. In this context, the lower curve is usually referred to as 'open channel' and converges to the atomic energy levels of two atoms in an ultracold gas. The upper channel (closed channel) has bound molecular states close to the last bound state of the lower state (indicated in the figure by horizontal solid and broken lines). Two atoms colliding with a low energy E, which is reasonable in a sample of ultracold atoms, can be described by a scattering state. If the energies of the scattering state of the open channel and the bound state of the closed channel come close, a Feshbach resonance occurs. This leads to a strong mixing of the two states and can result in a bound Feshbach molecule. The energy difference of the coupling states can be controlled by a magnetic field. The magneto-association of atoms is performed by sweeping a magnetic field over the Feshbach resonance. Of course,

the prerequisite of magneto-association is the existence of a Feshbach resonance, i.e. one of the atoms or the molecule needs to have a magnetic dipole moment.

It is interesting to mention that with Feshbach resonances, a connection of quantum degenerate gases of bosons and fermions can be found. The phenomenon arises with ultracold Fermi gases. The gas of the single particles is a quantum degenerate Fermi gas, a formation of molecules via the Feshbach resonance, however, leads to a molecular BEC [29]. A more detailed explanation would go beyond the scope of this work, ref. [28] presents the topic in an easily comprehensible way and is recommended for reading, while a more detailed description is provided in ref. [29] and references therein.

1.6.3 Stimulated Raman Adiabatic Passage (STIRAP)

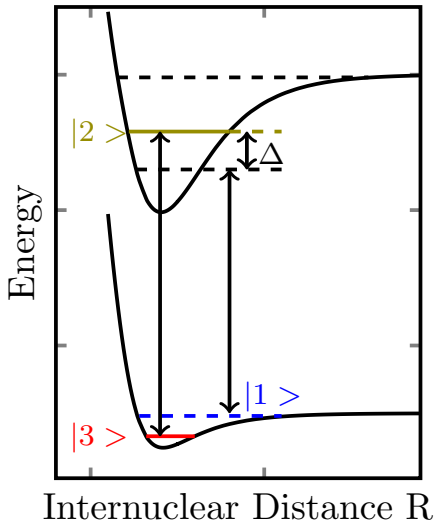

Figure 1.12: Concept of stimulated Raman adiabatic passage: The original state $|1\rangle$ and final state $|3\rangle$ are coupled via the intermediate state $|2\rangle$. Δ denotes the detuning of the laser frequency to the transition frequency. This method allows to efficiently transfer the population of $|1\rangle$ to $|3\rangle$.

In both PA and MA the resulting bound molecules are generally not in their ro-vibronic ground state. To further 'cool' the molecules, stimulated processes like STIRAP can be applied. This method has also been used to directly form molecules, when MA was not applicable - see the formation of ultracold Sr_2 in ref. [149].
Figure 1.12 illustrates the principle of the process. STIRAP allows to efficiently transfer molecules from a vibrationally excited state $|1\rangle$ (initial state) to a low rovibronic or even the ground state within the electronic ground state $|3\rangle$ (target state). This is done by coupling the two states via an electronically excited state of the molecule $|2\rangle$ (intermediate state) with two laser beams.
A detailed and understandable description of different methods of laser-induced population transfer by adiabatic passage techniques has been provided by Vitanov et al. in ref. [165]. In short, STIRAP uses a few quantum-mechanic facts: Firstly, an excitation of molecules by a coherent light source (laser) leads to an oscillation of the populations, where the population of both involved states theoretically varies between 0 and 1. This can also be applied to a three-level scheme as indicated in fig.1.12, in this case it is also referred to as pump-dump scheme, state $|2\rangle$ is excited by resonant laser light and a second laser induces stimulated emission into the target

state $|3\rangle$. However, this method (SEP- stimulated emission pumping) is subject to several forms of losses, induced for example by intensity fluctuations of the laser, the velocity distribution of the molecules and radiation losses of the intermediate state. The transfer rate can be increased significantly by using an adiabatic transfer scheme. In general, sweeping the detuning Δ of the laser frequency to the transition frequency can lead to an avoided crossing of the two involved states (for a detailed description see ref. [165]). This can be used to adiabatically transfer the population from one state to another. It is also possible to couple three states in this way leading to the method of STIRAP. A special peculiarity of this method is that the laser pulse coupling the states $|2\rangle$ and $|3\rangle$ is applied before the laser pulse coupling the states $|1\rangle$ and $|2\rangle$. Effectively this results in a coupling of the initial to the target state ($|1\rangle$ to $|3\rangle$) without populating the intermediate state $|2\rangle$. This leads to a very efficient coherent population transfer, e.g. for KRb a transfer efficiency of 83% has been achieved [123].
Please note that a thorough and careful treatment of this method in its full scope is not possible here, a great review about this topic is provided by ref. [165] including a theoretical explanation and notes concerning the experimental realization of STIRAP.

1.6.4 Summary

The methods of photo-association, magneto-association and STIRAP have led to the successful formation of homonuclear [34, 155] and heteronuclear [123, 124] diatomic alkali molecules in the ultracold temperature regime (see e.g. table 1 in ref. [134]). Very recently also the homonuclear alkaline earth metal dimer Sr_2 could be prepared in an ultracold state [149]. In this context interest has been raised in mixed ultracold diatomic Ak-Ake molecules. These molecules are of interest, because they possess not only an electric dipole moment but also a magnetic dipole moment due to the unpaired electron. This provides an additional experimentally accessible parameter, opening the door for a whole set of new experiments and applications [75,112]. Several different molecules are currently under investigation, theoretically [55,56,76] and experimentally [58], one of the most promising candidates among this molecular species being RbSr [7, 125, 169, 170] and also RbCa [54].
The main point of this short presentation of these methods is to show how important a profound knowledge of the molecular structure of the corresponding molecule is. Especially for RbSr and RbCa such knowledge is hard to access, since they are difficult to investigate. This is how helium nanodroplet isolation spectroscopy is connected to ultracold molecules: With the help of helium nanodroplet isolation spectroscopy these molecules can be formed and investigated, allowing to revise theoretical calculations and potentially providing important information for ultracold molecular physics.

CHAPTER 2

Experimental Setup

The cluster beam apparatus used for the experiments presented in this thesis has gone through several alterations, amendments and updates since its relocation from Penn State University to Graz University of Technology in 2003. Many master and PhD theses have been written on experiments performed with this machine and in each a detailed description of the momentary status of the setup is given. In the beginning of this section the most important works and the corresponding amendments and methods performed and described in the course of these works are listed. The subsequent sections will give a short overview of the principal of function of the current experimental setup, in order to provide the inclined reader with a better understanding of an experiment with HENDI spectroscopy.

Table 2.1: List of works in detail describing the experimental setup and amendments to it. 'Previously used' marks experimental techniques which have been performed with the apparatus but are currently not implemented.

Author and Year	**Title and exp. setup related contents of the work**
Johann Nagl MSc thesis 2004 Ref. [118]	*Aufbau und Test einer Düsenstrahlapparatur zur Spektroskopie an alkalimetalldotierten Edelgasclustern* Thorough description of room layout and assembly of apparatus as well as the cluster beam generation. Technical details of cluster beam alignment, beam chopper and LIF system. Previously used: Argon Cluster Beam. *Laser systems:* Argon Ion laser (pump laser) and Coherent 599, 699 and 899 ring lasers.
Johann Nagl PhD thesis 2008 Ref. [119]	*Spectroscopic Investigations of Homo- and Heteronuclear Molecules of K and Rb on the Surface of Argon and Helium Clusters* QMS and Langmuir Taylor detector added. Detailed description of the cw laser system and optics. Previously Used: Depletion spectroscopy with Langmuir Taylor detector. *Laser system:* Ar^+ Ion pump laser, Coherent dye lasers and Ti:Sa ring laser.
Gerald Auböck PhD thesis 2009 Ref. [8]	*Spectroscopy of Alkali-Metal Atoms and their High-Spin Oligomers on Helium Nanodroplets in External Magnetic Fields* Description of LIF (photomultiplier tube and spectrograph) and beam depletion spectroscopy. *Previously used:* Magnetic Circular Dichroism.
Alexandra Pifrader MSc thesis 2009 Ref. [129]	*Pulsed Laser Spectroscopic Investigations of Rubidium Atoms Attached to Helium Nanodroplets.* Detailed description of the Coherent Indigo-S pulsed Ti:Sa laser system.
Florian Lackner MSc thesis 2009 Ref. [90]	*Laserspektroskopie und Flugzeitmassenspektrometrie an Rubidium-dotierten Heliumnanotröpfchen* Time-of-flight mass spectrometer added to the apparatus. Detailed outline of implementation and handling. Description of the LIF system.
Günter Krois MSc thesis 2011 Ref. [86]	*Heavy Alkali and Alkaline Earth Metals on Cold Helium Droplets: First Comparison of Excitation Spectra* Redesign of the pickup oven. Detailed description of the Lambda Physik pulsed dye laser system. *Laser system:* XeCl pump laser, Lambda Physik FL3002 pulsed dye laser.
Moritz Theisen PhD thesis 2011 Ref. [156]	*Agglomeration and Examination of Alkali Clusters on He Nanodroplets* Overview of detection methods, thorough description of time-of-flight mass spectroscopy and ZEKE spectroscopy.
Florian Lackner PhD thesis 2012 Ref. [91]	*Rydberg States of Alkali-Metal Atoms on Superfluid Helium Nanodroplets* Thorough description of cluster size distribution and pickup statistics, as well as LIF and REMPI-TOF spectroscopy and pulsed field ionization.
Thomas Buchsteiner MSc thesis 2014 Ref.	*Spectroscopy of Cold Atoms and Molecules Prepared with Helium Nanodroplets*

2.1 The Experimental Setup in a Nutshell

This section aims at giving the reader a quick and intelligible overview of the experimental setup and its working principle. Technical details to the single parts of the experimental setup are listed in the next section.
Figure 2.1 shows the life cycle of a helium droplet beam, the images are taken from an animation prepared during my master thesis [86]. (a) shows an overview of the droplet beam apparatus, generally it is sectioned into three parts, from right to left: The *source chamber* where the droplets are created, the *pickup chamber* where the droplets are doped and the *detection chamber* where the experiments take place. The following pictures show close ups of the droplet production, pickup and detection in a chronological order (b)-(f). Considering a droplet speed of 400 m/s on average, the lifetime of a droplet from creation to termination at the end of the apparatus is in the order of 5 ms. (b) shows a close-up of the source chamber: Here liquid helium from a dewar is used to cool the helium reservoir and the nozzle via a heat exchanger. All these elements are mounted at the end of a steel tube system through which the cooling helium is guided. The liquid helium is also used to pre-cool the high purity helium used for the droplet production, this is indicated by the blue coil in image (b). Image (c) zooms further in on to the heart of the source chamber: The 5 μm nozzle, a small silver disc at the end of the brown helium reservoir. The pre-cooled (15 K) high purity helium (indicated by blue dots) is expanded under high pressure (in our experiments 60 bar) through this small nozzle into the vacuum of the source chamber. As described in section 1.4 p6, these source conditions lead to the supersonic jet expansion which creates the helium droplets. The continuation of the droplet beam is shown in (d): On the right side of the picture, the 400 μm skimmer can be seen, which is used to extract the droplet beam from the helium atoms in the source chamber. Once the droplet beam is skimmed, it transcends via a valve into the pickup chamber, where it passes a chopper and then enters the pickup cell. This is shown in (e): Provided the temperature of the pickup cell is set correctly, the helium droplets pick up one dopant atom on average when flying through a pickup cell. In the course of this work two pickup cells were aligned after each other, allowing a doping of the droplets with two different species. The doped droplet then enters the detection chamber (f), where it first passes through the LIF tube, then through the extraction plates of the time-of-flight mass spectrometer and finally the beam terminates in a QMS mass spectrometer.

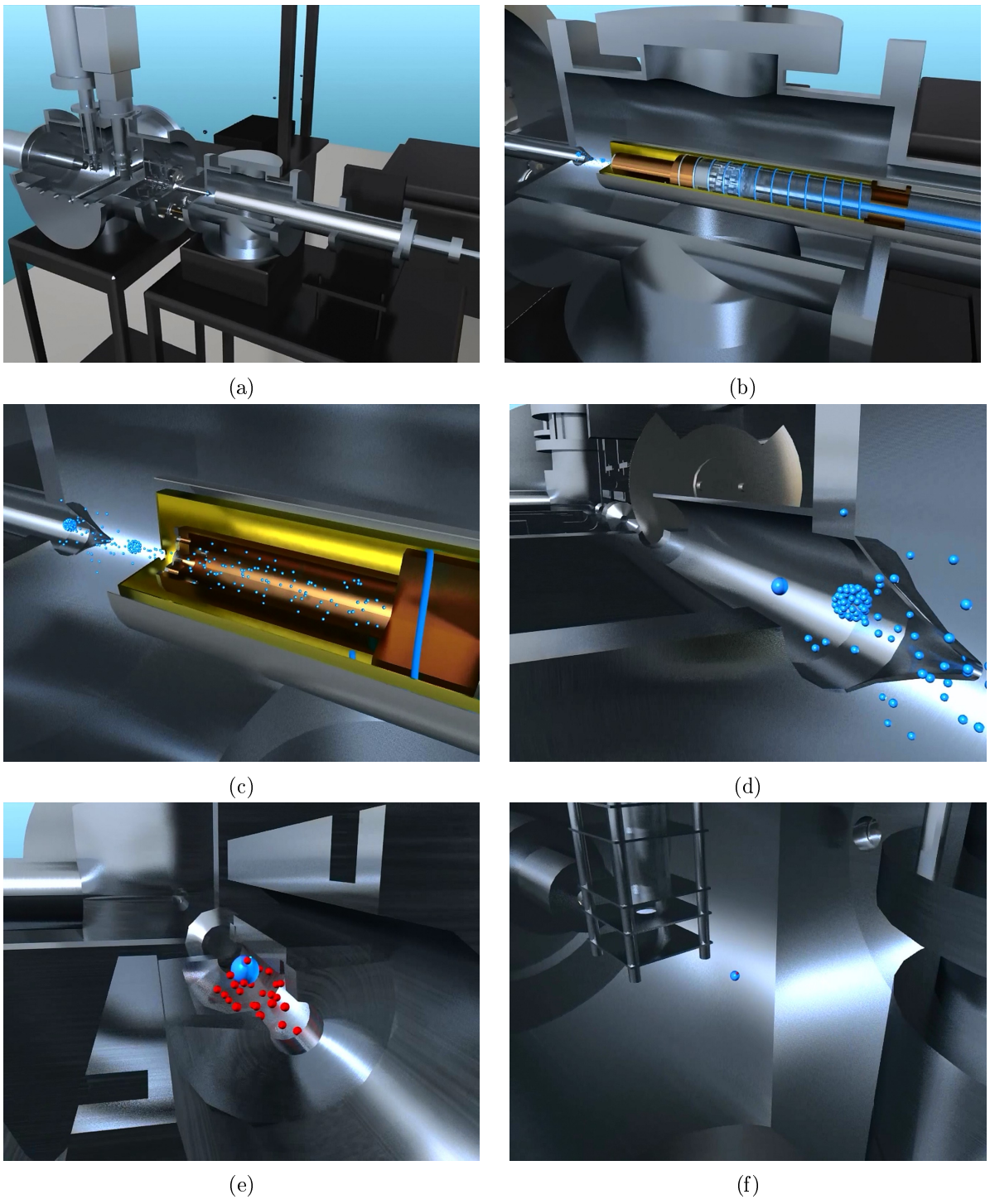

Figure 2.1: Screenshots of an animation showing the helium cluster beam production and its path through the apparatus including the pickup of an atom.

2.2 Technical Details to the Experimental Setup

Some relevant data of the single parts of the experimental setup are stated in the following

2.2.1 Source Chamber

The source chamber holds the nozzle setup and the skimmer, here the He droplet beam is produced.
Pressure: $< 10^{-3}$ mbar or $\sim 10^{-6}$ mbar with and without the He cluster beam, respectively.
Pumps: A rotary vane and a roots forepump create a pressure in the foreline of 4.2×10^{-2} mbar which increases to 6.2×10^{-2} mbar when the droplet beam is established. The main pump is an oil diffusion pump with a pumping speed of 6000 l/s. This is necessary because of the huge amount of helium gas expanding from the nozzle. Note that the forepressure can act as an indicator for a clogged nozzle - if the pressure is significantly below 6×10^{-2} mbar at source conditions of p_0 =60 bars and T_0 =15 K, the nozzle is most probably clogged.
In the source chamber the droplet beam is established, a general description is given in section 1.4 p6. In short: High purity helium gas (grade 6.0) is expanded under high pressure ($p_0 = 60$ bar) through a nozzle ($d_0 = 5\,\mu$m), held at a temperature of $T_0 = 15$ K through liquid helium cooling. The excessive helium gas is cut off by the 400 μm skimmer at the end of the source chamber (cd fig.2.1 (b)). The given source conditions lead to a mean droplet size of $\hat{N}_{60,15} = 6000$, corresponding to a mean droplet radius of $\hat{R}_{60,15} = 40\,\mathring{A}$ (assuming spherical droplets [163]).
The nozzle temperature can be changed in order to achieve different droplet sizes as described in section 1.4 p6.

2.2.2 Pickup Chamber

The pickup chamber contains the pickup cells, here the He droplets are doped with the desired species.
Pressure: 10^{-7} mbar in general and up to 10^{-5} mbar at high pickup temperatures.
Pumps: A turbomolecular pump with a rotary vane forepump.

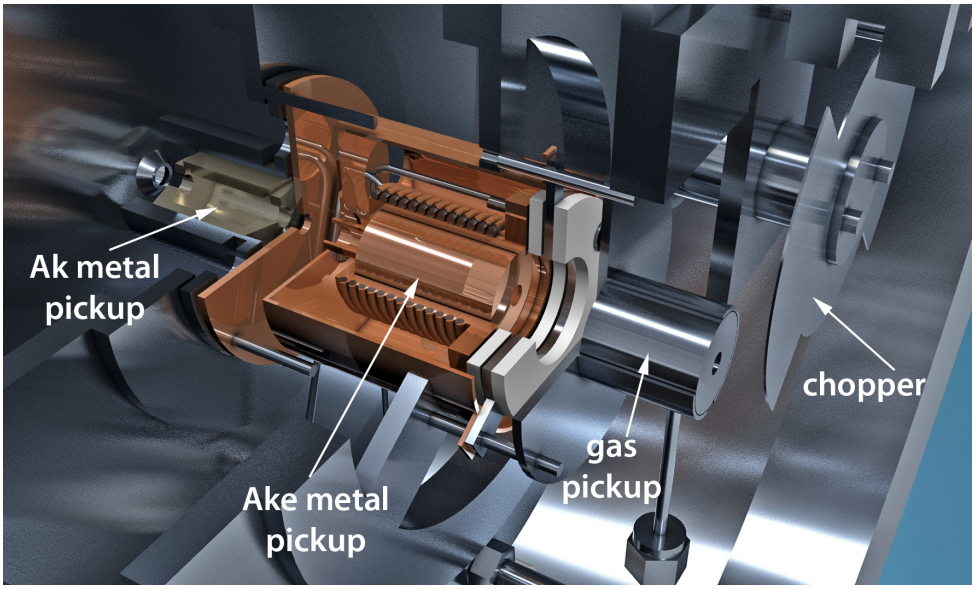

Figure 2.2: Drawing of the pickup chamber containing all currently available pickup designs.

Figure 2.2 shows a CAD drawing of the pickup chamber containing three versions of pickup cells. From right to left, following the direction of propagation of the droplet beam: After the chopper, the He beam passes through a gas pickup cell, a simple metal cylinder attached to a gas pipe, which is connected to a valve system via a feedthrough. The pickup of a certain gas is simply established by connecting the gas and carefully adjusting the pressure in the pickup cell, this system is described in more detail in [91]. The next pickup cell has been designed for the pickup of alkaline earth metals during my Master thesis [86]. To reach an appropriate vapor pressure, Ake metals have to be heated to relatively high temperatures, hence the oven and thermal shielding had to be redesigned. The current system uses a high quality steel cylinder as a pickup cell and a copper cylinder wrapped with a thermocoax (special resistive heating wire). To prevent a heating of the surrounding, a thermal shield made of copper has been added and connected to a copper feedthrough by a thick copper cable for heat conductance. The oven has been tested up to 600 °C, however, for a short time it is possible to heat to higher temperatures (according to the specifications of the thermocoax up to 1000 °C at atmospheric pressure), though that will lead to a heating of the surrounding. The last pickup cell shown in Figure 2.2 is the old design build for alkali metal pickup. To reach the appropriate vapor pressure for Ak metals, only $\sim 100\,^{\circ}\mathrm{C}$ are necessary, hence the oven design was kept simpler but also smaller, which is an advantage in the case of the very limited space in beam direction, in the pickup chamber.
Through most of the measurements performed during this thesis, two of the copper ovens were installed in the pickup cell. The advantage of the copper oven design besides the higher reachable temperature, are the thermal shields, so that the hot Ake oven does not heat the Ak oven, which usually has $\sim 200\,^{\circ}\mathrm{C}$ less.
During the experiments the first pickup cell was always loaded with the Ak metal and the second with the Ake metal. This way the less critical Ake can be loaded first and the pickup chamber can be closed quickly after loading the Ak metal. Both materials are loaded in the pickup cell under Argon atmosphere within a glove bag. The pickup cell is filled with n-hexan before it is taken out of the glove bag. This prevents the formation of an oxidation layer on both Ak and Ake. The Ake materials are quite uncritical to treat, but it is necessary to take care that they are not exposed to air. It also helps to cut the Ake metal into smaller pieces when loading the pickup cell, so that at least the cut edges are free of possible oxide layers.

It has been shown by Florian Lackner [91] that the theoretical temperature for an optimized monomer pickup deviates from the experimentally determined optimum for the oven temperature. Due to technical reasons and mainly because of the non-heat-conducting vacuum there is a temperature gradient between the thermocoax and the temperature of the dopant material. It is not possible to run the Eurotherm controller of the oven via the temperature of the oven itself, since the reaction time of cell to a temperature change of the oven is too slow. Hence a set of thermocouples has been attached to the pickup cells, so that their actual temperatures can be read out.
According to [91], the maximum of the monomer pickup of Rb is reached at a temperature around 60-70 °C. The former oven setup had to be set to a temperature around 100-110 °C to reach this maximum. The new setup can be held at slightly lower temperatures ($\sim$90-100 °C) and the pickup cell temperature is around 70-80 °C for an optimized monomer pickup of Rb. The small deviation is explained by the temperature gradient of the pickup cell and the dopant material therein on the one hand and by some idealized assumptions of the theoretical model on the other (e.g. that each droplet-dopant collision leads to a pickup).

2.2.3 Detection Chamber

The detection chamber holds the various detection devices used for the spectroscopic investigations.
Pressure: 10^{-7} mbar
Pumps: Two turbomolecular pumps, the larger one with a rotary vane forepump sits at the bottom of the detection chamber and a small pump is mounted on the time-of-flight mass spectrometer.

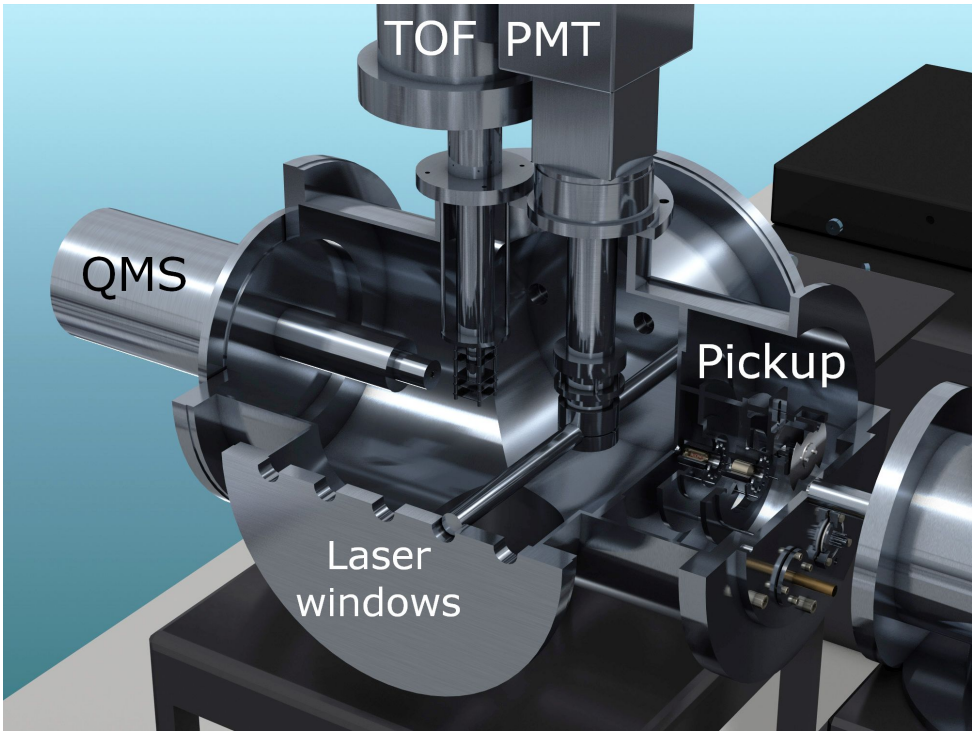

Figure 2.3: Drawing of the pickup and detection chamber, showing the different detection devices.

On each side of the chamber four sets of windows are mounted in order to let laser light interact with the droplet beam. Following the propagation direction of the He beam, firstly the baffle tube system for beam depletion and then the baffle tube system for laser induced fluorescence (LIF) experiments are mounted. A lens system (described in [118]) collimates the photons emitted from excited atoms or molecules through a vertical pipe up to the detection device. This can either be a photomultiplier tube (Hamamatsu R943-02) or a grating spectrograph (McPherson EU-700) with a CCD camera attached (LOT-Andor iDUS DU401ABR-DD). In case of the grating spectrograph the fluorescent light is either guided through a fiber into the spectrograph or via a mirror system. Latter leads to a better signal but is more time consuming to set up, a closer description is given in the LIF section 3.2 p46.
After the LIF system, the He beam passes through the extraction field plates of the time-of-flight (TOF) mass spectrometer (Jordan D-850 AREF). The TOF is described in detail in ref. [90]. It can be operated in linear and reflectron mode. As for most measurements during this thesis a high resolution for lower masses was interesting, generally the reflectron mode was used.
At the end of the detection chamber a quadrupol mass spectrometer (QMS) is mounted (Extrel C50-Q). It has been used for beam depletion before, but is currently mainly used for the alignment of the He beam. The beam has to be aligned after the initial cooling of the setup to the desired

nozzle temperature, and it is advisable to realign the beam for an optimized signal after every change of the nozzle temperature.

2.2.4 Laser Systems

For the sake of a better overview, the laser systems, as well as the laser dyes, used in the course of this thesis and their most important specifications are listed in table 2.2 below.

Table 2.2: Specification of the available laser systems and used laser dyes.
λ... Wavelength range of this type of laser in the corresponding mode or with the corresponding dye.
$P_{\max}$... Maximum power of the corresponding laser system.
pumped by... pumping laser;

Type	**Name**	**Mode**	**λ / nm**	**P_{max}**[a]		**pumped by**
XeCl Excimer	Radiant Dyes RD-EXC-200	pulsed	308	200	mJ	
Nd:YAG	Coherent Verdi V10	cw; SHG	532	10	W	
Nd:YAG	Coherent Verdi V18	cw; SHG	532	18	W	
Ti:Sa	Coherent 899 Ring Laser	cw[c]	770-900[b]	5	W	Verdi V18
Dye	Coherent 699 Ring Dye Laser	cw[c]				Verdi V10
	Pyridine 1		680-750	1.0	W	
	DCM		617-699	1.0	W	
	Rhodamin B		588-644	1.5	W	
	Rhodamin 6G		575-626	2.8	W	
Dye	Lambda Physik FL3002	pulsed				XeCl (40-60 mJ)
	Coumarin 2		435-470	2.5	mJ	
	Coumarin 102		465-495	1.5	mJ	
	Coumarin 307		485-530	1.6	mJ	
	Coumarin 6		507-542	0.9	mJ	
	Coumarin 153		525-575	2.0	mJ	
	Rhodamine 6G		571-605	4.3	mJ	
	Rhodamine B		600-635	3.4	mJ	
	DCM		615-680	1.5	mJ	
	Pyridine 1		675-735	1.6	mJ	
	Pyridine 2		705-765	2.0	mJ	
	Rhodamine 800		770-810	2.0	mJ	
	Styryl 9		800-855	2.0	mJ	

[a] Values are taken from experiments, not from a book, but should only to be taken as guideline, since they strongly depend on the current dye solution and pump laser power.
[b] Valid for the mid-range mirror set used.
[c] Operated in multi-mode.

2.3 Detection and Data Acquisition Devices

In order to be able to concentrate on the spectroscopic techniques in the next chapter, the devices used for the corresponding methods are listed here (cf. tab. 2.3). The data analysis and evaluation is performed with Matlab programs.

Table 2.3: List of applied spectroscopic methods with the corresponding detection and data acquisition devices.

Spectroscopic Method	**Detection Device**	**Data Acquisition**	**Data processing**
LIF excitation spectra	PMT (Hamamatsu R943-02)	amp, SR400-disc, Chopper control[a]	LabView program
LIF dispersed emission spectra	Grating spectrograph[b] (McPherson EU-700, LOT-Andor iDUS DU401ABR-DD)	Andor software (LOT Andor Solis)	
REMPI-TOF spectra	TOF (Jordan D-850 AREF)	amp, SR400	LabView program
REMPI-TOF spectra	TOF (Jordan D-850 AREF)	amp, SR400-disc, MCA	Matlab program

[a] homemade chopper and counter control, separating the SR400 input into chopper open and closed signal.
[b] Grating spectrograph with attached CCD camera.

Abbreviations:

LIF	... laser induced fluorescence
REMPI-TOF	... resonance enhanced multi-photon time-of-flight ionization spectroscopy
SR400	... Stanford Research Model 400 gated photon counter 'disc' means the SR400 is only used as a discriminator to cut off noise.
PMT	... photo multiplier tube
TOF	... time-of-flight mass spectrometer
amp	... homemade 100x amplifier
MCA	... homemade multi-channel analyzer (see below)

2.3.1 Multi-Channel-Analyzer

In this paragraph a closer description of the homemade multi-channel-analyzer (MCA) is given, on the one hand, because it was used in the majority of the experiments relevant to this thesis and on the other hand, because the Matlab readout software was completely redesigned in the course of this thesis. It was built by the in-house electronic workshop and its first readout software was programmed by Markus Krug [89].

The MCA is a counter, its core is a register counter (FPGA) chip with 4096 time windows, each of which has a width of 50 ns, hence, the whole time range spans 200μs. The acquisition time is set to 1 s, then the data are sent to the PC via a RS232 interface. The basic functions are reflected by the three inputs: The trigger signal which starts the counting process is connected to

'Start', the signal that is to be counted to 'Signal' and in case the signal is chopped, the chopper is connected to 'Chopper', so that light and dark counts can be separated. In the present case the MCA is only used as a counter for the time-of-flight signal, as explained in section 3.1 p42. The reasons for the redesign of the software were required extensions on the one hand and speed problems on the other hand. While the data acquisition lasts 1 s the transfer process of the whole time range lasts up to 4 s due to the low baud rate of the RS232 interface. In a REMPI-TOF experiment this would mean that each data point takes 5 s to record. Considering the number of steps necessary for an appropriate signal, this leads to very long measuring times, which is not only inconvenient, but also causes problems in keeping all measuring parameters (especially temperatures) stable. Therefore, the Matlab MCA control has been extended in the course of this thesis, optimizing the speed of the program and adding several features, which made REMPI-TOF experiments possible (see section 3.1 p42). A detailed explanation and the source code are included on the CD enclosed to this work. The program has been completely redesigned and a GUI has been added for an easier control, cf fig. 2.4. The main features added concerning the experiments are:

1. Several time (i.e. mass) windows to be measured can be selected (panel 'First-Last Window in μs' in the GUI)

2. The signal for one or several mass windows ('Counts over Wavelength Plot') can be plotted over:
   - the wavelength of the laser measured by the Coherent Wavemaster
   - the wavelength of the laser measured by the Burleigh WA-1500 Wavemaster
   - a simple vector
   - the system time

The first amendment allows to select several narrow time windows corresponding to either a single mass or a whole mass range, for example, which considerably lowers the amount of data to transfer and hence the transfer time. Additionally, the measured windows can be shown as a function of the laser wavelength, providing the user with a REMPI-TOF signal for all masses selected in the 'Counts over Wavelength Plot' section of the GUI.
As an example from the measurements performed on Ak-Ake doped He droplets, the measured time range was set to extend from the lightest monomer to the heaviest trimer (e.g., RbCa: $\sim$33.5 s-90 s, corresponding to $\sim$35 amu-290 amu). Additionally, several mass ranges for the single atoms and molecules of interest were selected for the signal over wavelength plot. With this method the behavior of the signal of single atoms and molecules of interest can be traced during one measurement while all masses of interest are recorded simultaneously.
Several wavelength measuring devices can be selected ('Wavemeter'). Usually, the Coherent Wavemaster is used. However, in some cases it is not possible to record the wavelength with the Wavemaster, e.g. when the laser intensity is too low or out of range for the wavemeter. In the case of the Lambdaphysik FL3002 dye laser the wavelengths can be read out from the laser directly. Please note that it is more accurate to use the wavemeter when possible. The wavelengths of the laser cannot be directly read by the MCA control due to software incompatibilities, hence the wavelength data is written to a file together with the system time for each wavelength step. Correspondingly the option 'Time' in the wavemeter section of the GUI offers the possibility to label each data point of the REMPI data with the system time. A Matlab routine can be used to read and merge both files, so that the correct wavelength is found for each data point.
The same routine can be used to record the signal over the pickup temperature. A LabView

program allows to record the pickup temperature from a Voltcraft datalogger and write it to a file, again as a function of the system time. This can be used to find the ideal temperatures for monomer, dimer or mixed molecule pickup.
As a suggestion, for a future improvement: A considerable speedup of the system can be achieved by implementing a USB connection of the PC to the MCA.

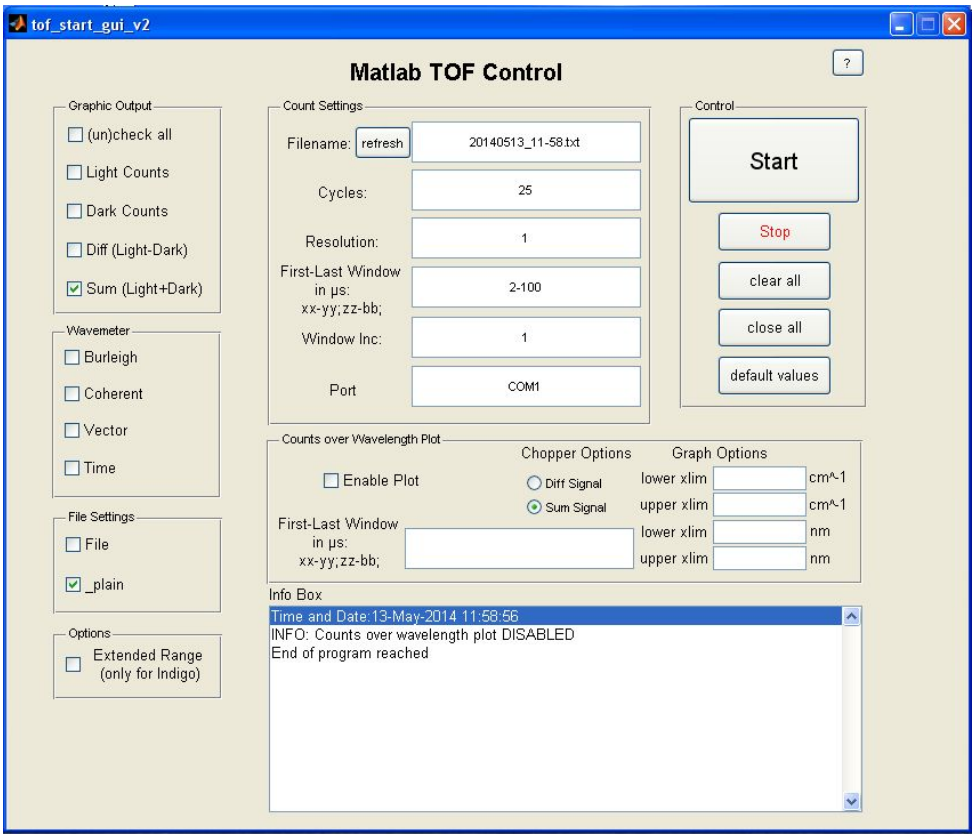

Figure 2.4: Screenshot of the GUI for the control of the MCA.

CHAPTER 3

Experimental Methods

In this section the two spectroscopic methods used to investigate doped He droplets will be introduced. The main focus will lie on the differences between the two methods and their respective advantages and disadvantages. In the second part of each section, the workflow of each experiment specific to our laboratory will be explained, including references to the devices and settings used.

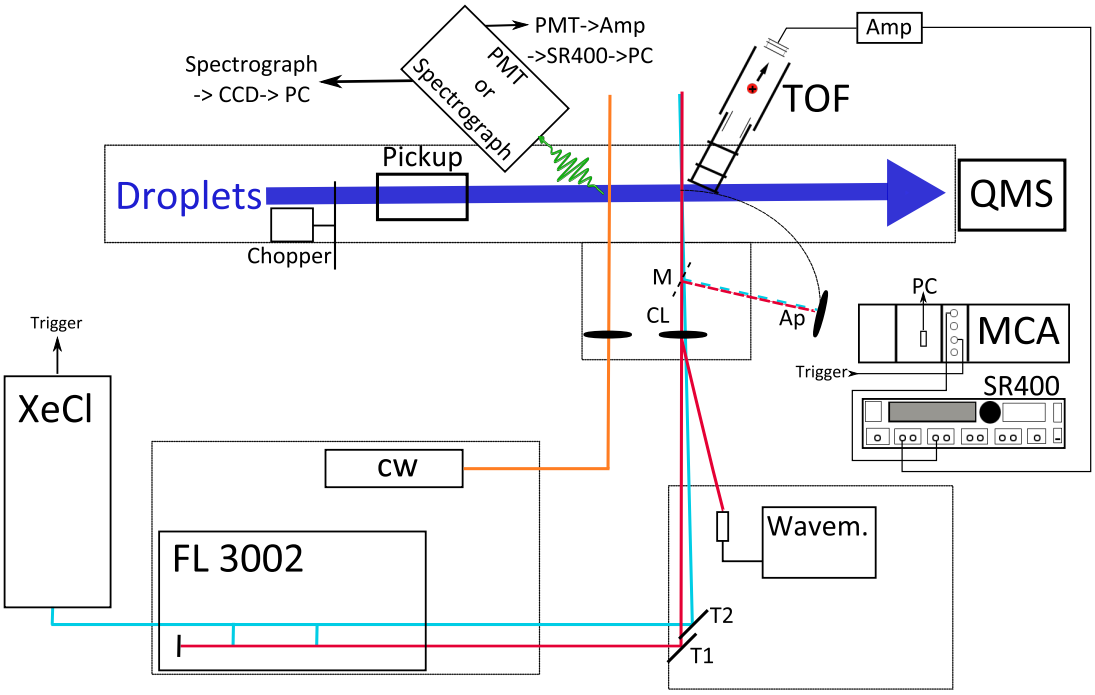

Figure 3.1: Schematics of the experimental setup for REMPI-TOF and LIF experiments.

3.1 Resonance Enhanced Multi-photon Ionization Time-of-flight Mass (REMPI-TOF) Spectroscopy

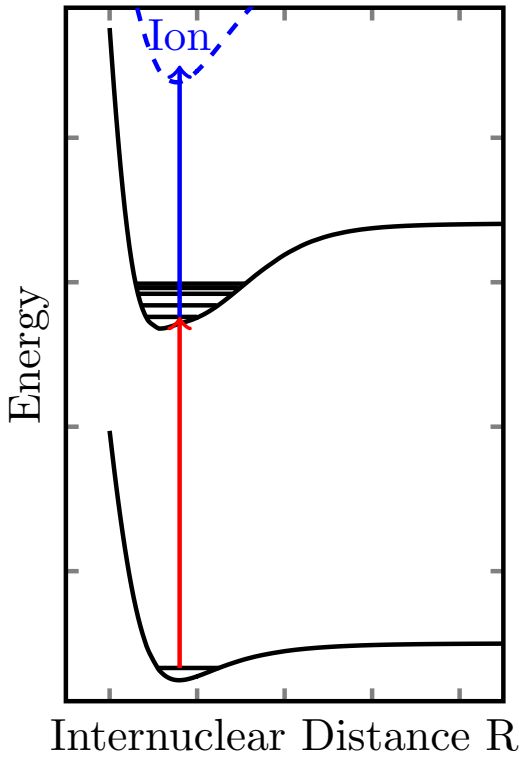

Figure 3.2: Schematics of Resonance Enhanced Multi Photon Ionisation Time-Of-Flight mass spectroscopy. A photon of one laser excites the molecule and a second photon of the same or another laser ionizes it. The ion yield is detected by a time-of-flight mass spectrometer.

3.1.1 General

In short REMPI-TOF means the (resonant) excitation of an atom or molecule to an excited state and the subsequent ionization (direct or via intermediate states), as sketched in fig. 3.2. Depending on the number of photons involved in the ionization process, it can also be referred to as R2PI, R3PI, etc. The ion yield is then detected by a time-of-flight mass spectrometer. A mass-selective detection requires a pulsed laser, where the rising edge of the laser pulse is used as the starting point of the time-of-flight measurement. For the sake of completeness it has to be mentioned that, in principle, the use of a cw laser is possible for the ionization, but in this case the TOF would only act as an ion counter and the mass-selectivity would be lost.
The huge advantage of REMPI-TOF spectroscopy is its mass-selectivity, which easily allows to separate the signals of various excited molecules. This is especially important for Ak-Ake molecules on He droplets, since the statistical pickup process always entails a probability of a dimer pickup (Ak_2 or Ake_2). Due to the broad molecular excitations on the droplet, the excitations of the Ak-Ake molecule and one of the dimers might overlap. However, since REMPI-TOF is mass selective, the contributions of the different molecules can be separated, and in some cases one measurement does not only give valuable information about the primarily investigated molecule but also about dimers, as shown for Li_2, Sr_2 and Ca_2 in the results section.
Another benefit of this method is the large accessible wavelength range. With the help of a

set of laser dyes, a range from 11600 cm^{-1} (lower range of the FL3002 pulsed dye laser) up to 24000 cm^{-1} and farther can be reached. Additionally, the present pulsed laser setup is more flexible allowing a fast and efficient change and optimization procedure for laser dyes. Hence a large wavelength range can be covered in a single experiment and a reasonable timeframe, which in turn allows a better maintenance of experimental conditions.
The limited resolution of the REMPI-TOF method, due to the bandwidth of the pulsed dye lasers, can be neglected here. Considering the application, the broadening of the lines by the helium droplet always exceeds the laser bandwidth. To give some numbers as an example: For the pulsed laser system engaged, the factory calibration gives a linewidth of 0.06 cm^{-1} at 520 nm, which is huge in comparison to the linewidth of the cw ring dye laser (Coherent 699) used for LIF ($<$1 MHz$\sim 10^{-5}$ cm^{-1} in single mode, calibrated with Rh6G). The linewidhts of the vibrational lines of molecules on the He droplet were usually in the range of several tens of cm^{-1}. Thus, the cw lasers were also only used in the broadband mode, showing a nominal linewidth of 8-12 GHz $\sim$0.2-0.4 cm^{-1}.
When interpreting a REMPI-TOF excitation spectrum, it is important to consider that it is always at least a two photon process. I.e., in order to get an ion, the molecule has to be excited into an upper state and then ionized. It is important to keep in mind that both processes underlie a transition probability (see section 1.5 p13), so not only the transition probability from the ground state to the excited plays a role, but also the transition probability into the ionic potential, see fig. 3.2. If more than two photons are involved, the complexity of the process further increases since the transition probabilities and lifetimes of all involved states have to be considered. Experimentally this means that, if two lasers are used, the correct ratio of lasers to sufficiently excite one state while not saturating the other has to be found. If only one laser is used in a multi-photon absorption experiment, this optimization of the laser pulse energy is not possible and might lead to saturated signals.

3.1.2 Specific

The experimental setup as implemented in our laboratory is sketched in figure 3.1. The pulsed laser (FL 3002) is guided through appropriate mirrors to the optical platform in front of the entrance windows of the apparatus, a 700 mm collecting lens (CL) is used to focus the laser onto the droplet beam. A reflex of CL is used to measure the wavelength of the laser (W). In case of a two photon ionization with the XeCl pump laser, a fraction of the pump laser is coupled out before the amplifier of the FL3002 (magenta line) and guided to the optical platform via mirrors. The easiest way to overlap the lasers has proven as follows: T1 and T2 in fig 3.1 label two towers where the guiding mirrors for both lasers are mounted. At first, the dye laser has to be guided through the apparatus horizontally (checked by the position of the laser reflex on entrance and exit window). In a second step, the XeCl laser is guided as closely as possible to the dye laser from T2 to the collection lens (CL). With the help of a mirror (M) and an aperture (Ap) mounted at the distance lens-droplet beam, the overlap of the lasers can be achieved. Due to the long distance between T1 and T2 to CL the overlap is easily possible at the point of the droplet beam.

The doped helium droplet beam is intersected by the laser beam at an angle of 90°. The laser light ionizes the dopant on the droplet via a resonant state. Upon ionization, the ion is extracted by the field plates of the TOF, see figure 3.3: The potential difference between the repeller plate (VA1) and the extraction plate (VA2) accelerates each ion equally. Depending on their mass, the ions reach different velocities. Once the ions pass a grounded field plate, they fly through the field-free drift zone with the velocity they have gained. It is easy to see that the longer the flight

time, the larger the distance between the single ions becomes - hence, the better the resolution. A longer drift zone, without changing the size of the TOF, can be accomplished by a reflectron, as indicated in figure 3.3. Here, the propagation direction of the ions is reversed by a set of field plates (VR1 and VR2) at the top of the TOF mass spectrometer and directed towards the multi-channel-plate (MCP) detector, located at the bottom of the TOF. Another set of plates is arranged parallel to the propagation direction of the ions, so that small corrections to the flight path can be made to optimize the signal (VXY). For all the results presented in this thesis the TOF has been operated in reflectron mode, using the voltages noted in table 3.1, where VXY may be adjusted slightly for a better signal. This is a very simplified account of the process, for a detailed description including an explanation of the resolution limiting factors of the Jordan D-850 AREF TOF mass spectrometer, the Master thesis of Florian Lackner is a recommended reading [90].

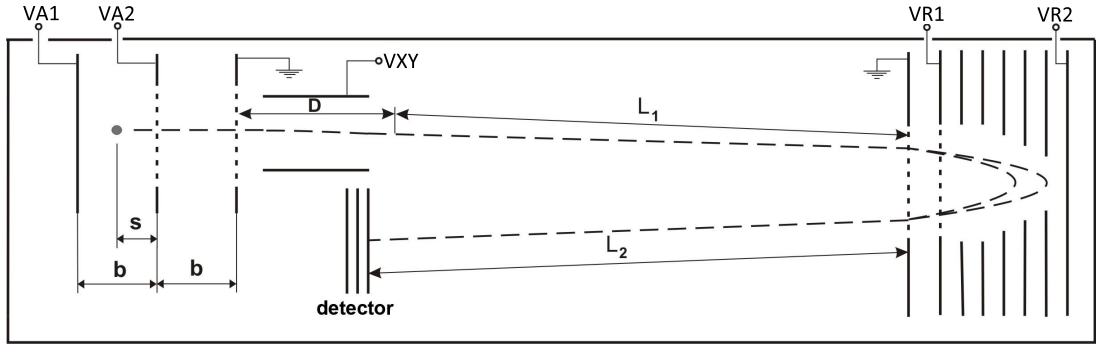

Figure 3.3: Schematics of the TOF in reflectron mode. The ions are extracted by the potential between the extraction plates (voltages U_R and U_B), their direction is reversed by the reflection plate system, (voltages U_R1 and U_R2). The vertical horizontal drift of the ions can be corrected by the voltage U_XY (modified from [90]).

Table 3.1: Voltages used for the time-of-flight mass spectrometer during the experiments in this thesis.

Detector (VD)	3700 V
Extraction plate 1 (VA1)	1000 V
Extraction plate 2 (VA2)	700 V
Vertical plates 2 (VXY2)	50 V
Reflection plate 1 (VR1)	700 V
Reflection plate 2 (VR2)	1200 V

Once the ions reach the MCP, the further data acquisition takes place as follows: The MCP creates a millivolt signal from the ion impact, this signal is amplified by a homemade 100x amplifier (Amp) and passed on to a Stanford Research 400 (SR400) counter. At this point, there are two possibilities to process the data:

a) SR400

The first possibility is to use this counter as a measuring device. In this case the trigger signal of the XeCl laser is connected to the SR400, the trigger is set to external and and 'T SET' is set to 100, i.e. 100 rising edges are accumulated. This corresponds to an acquisition time of 1 s at a repetition rate of 100 Hz of the XeCl laser. A LabView program allows to control the SR400 via a GPIB bus. Two time windows (gates) corresponding to a certain mass range can be defined by

giving the starting point (gate delay) and interval (gate width). Unfortunately, only two mass ranges can be measured simultaneously. The advantage of this method is that the SR400 is fast, mostly due to the GPIB bus, and can thus be more easily used for signal optimization.

b) MCA

The other option is to use the SR400 as a discriminator only, cutting off some of the noise (generally set to -12.8 mV) and feeding the signal into the MCA (see section 2.3 p37). In this case the SR400 trigger is set to 10 MHz and the acquisition time 'T SET' to 1 s. The discriminator output of the SR400 and the laser trigger are connected to the MCA ('Signal' and 'Start').
The huge advantage of the MCA is that the whole time range is measured simultaneously, so that, in contrast to the SR400, with each measuring cycle the whole time range from 0-200μs is available - correlating to a mass range of 0-700 amu for the given settings, see table 3.1. This way, during a REMPI-TOF experiment the signals of e.g. RbSr, Rb, Sr as well as Rb_2 and Sr_2 can be recorded simultaneously.

3.2 Laser Induced Fluorescence Spectroscopy

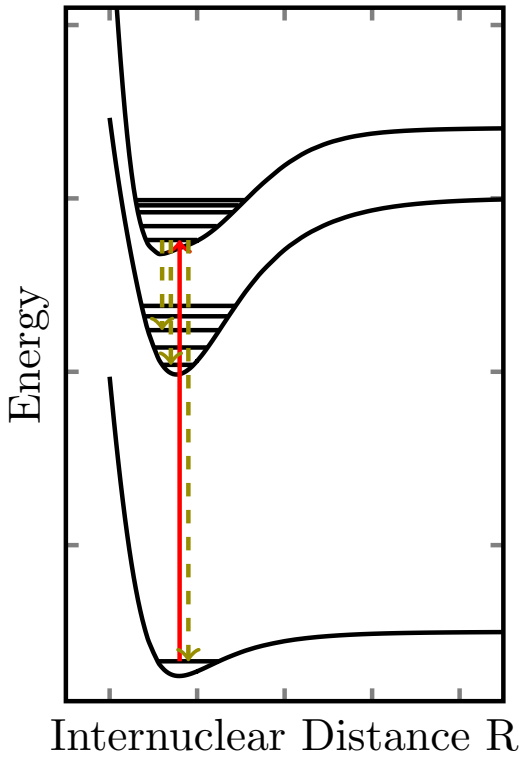

Figure 3.4: Schematics of Laser Induced Fluorescence spectroscopy. A cw dye laser is used to excite the molecule, from there fluorescent light from various relaxation channels will contribute to the fluorescence signal as long as the wavelength is within the detection limit of the photomultiplier.

3.2.1 General

Two different LIF spectroscopy methods were applied in the experiments performed, in the course of this thesis. In order to obtain an excitation spectrum the molecules on the He droplets were excited by a tunable cw laser and a photomultiplier tube (PMT) was used to detect fluorescence. In another type of experiment dispersed emission spectra were recorded by setting a cw laser to a certain transition, found in the REMPI-TOF or LIF signal, and by recording the emission spectra via a spectrograph and a CCD camera.
There is a very important difference between those two approaches: During the recording of the excitation spectrum, the dye laser is tuned over a wavelength range. A fluorescence signal will be detected by the PMT only if a transition is excited, but regardless of the fluorescence channel of the relaxation. At least, as long as the fluorescence photons are within a wavelength range where the quantum efficiency of the PMT is sufficient. For the present device (Hamamatsu R943-02) the quantum efficiency linearly decreases from its maximum ($>$20 %) at 300 nm ($\sim$33300 cm^{-1}) to $\sim$10 % at 850 nm ($\sim$11750 cm^{-1}) and then rapidly decreases to 0 % at 930 nm ($\sim$10750 cm^{-1}). The result is an excitation spectrum of the corresponding molecule on the helium droplet, similar to the REMPI-TOF spectrum but obtained via a different physical process (one-photon excitation instead of two- or multi-photon ionization) and a different detection method (photons instead of ions).
In the case of the emission spectra, the dye laser is set to a fixed wavelength, exciting a certain

transition. Upon excitation the molecule desorbs from the droplet. The excited free molecule will then relax via various relaxation channels to its ground state, emitting fluorescent light. A spectrograph is used to cover a wavelength range where fluorescent light is detected. The resulting spectra are frequency-resolved and give information about the fluorescence channels of the relaxing molecules. Since in most cases the relaxation of the molecule will not only lead to the population of the lowest vibrational level of the ground state, the emission spectra allow to draw conclusions about the ground state of the desorbed free molecule. The limiting factor of the linewidth is the grating spectrograph (in the order of $\sim$6 cm^{-1} with our spectrograph, depending on the slitwidth).

For LIF spectroscopy of this thesis cw lasers were applied, since they excite the atoms or molecules continuously, i.e. have a higher duty cycle. This is the reason why LIF excitation spectra in general show a much higher signal to noise ratio than REMPI-TOF spectra, and the excited transitions are less likely to be saturated, which may lead to more accurate molecular parameters.
Even though REMPI-TOF and LIF both give an excitation spectrum, the underlying physics is quite different. For REMPI-TOF the transition dipole moment into the excited state and the life time of the excited state as well as the TDM to the ionic state are important to consider. For LIF the TDM into the excited state is important too, but the probability for relaxation process is less important, since the molecule will relax into its ground state and the emitted photon will be detected[1]. But this also means that the origin of the light detected with the PMT cannot be identified and will most probably come from different fluorescence channels of the investigated atom (each again underlying selection rules and transition probabilities), or may also stem from other excited molecules. Especially for Ak-Ake molecules on He droplets the probability of exciting an Ak or Ake dimer along with the Ak-Ake molecule is high. To prevent this, either the pickup temperature can be lowered, and in consequence considerably lowering the probability of a dimer pickup, or the resulting spectra can be compared to known dimer transitions.

3.2.2 Specific

Several different cw lasers were used in the LIF experiments. Most prominently a Nd:YAG pumped (Coherent Verdi V10) dye ring laser (Coherent 699) and a Nd:YAG pumped (Coherent Verdi V18) Ti:Sa (Coherent 899) laser, were engaged. The sketch of the setup in fig. 3.1 only shows the ring dye laser. The wavelength ranges of the dye laser are given in table 2.2. In the case of LIF excitation spectra the fluorescence light was detected by a Hamamatsu R943-02 photo-multiplier tube, the signal was amplified by a 100x homemade amplifier and fed into the SR400 counter. A LabView program was used to read and process the data. In the case of dispersed emission spectra, a grating spectrograph (McPherson EU-700) with a CCD camera attached (LOT-Andor iDUS DU401ABR-DD) was used to record the signal. There are two ways to feed the fluorescent light from the LIF setup of the apparatus into the spectrograph: Either via a fiber bundle (Oriel 77538) or via a 200 mm collecting lens mounted directly atop of the output of the LIF setup on the droplet apparatus and a mirror guiding the light into the spectrograph (cf. fig. 3.5). The data processing was performed by the camera specific software (LOT Andor Solis).

[1] Note that this does not consider special cases such as metastable excited states, non-radiation emission process and fluorescent light outside the detection limit of the detection device engaged.

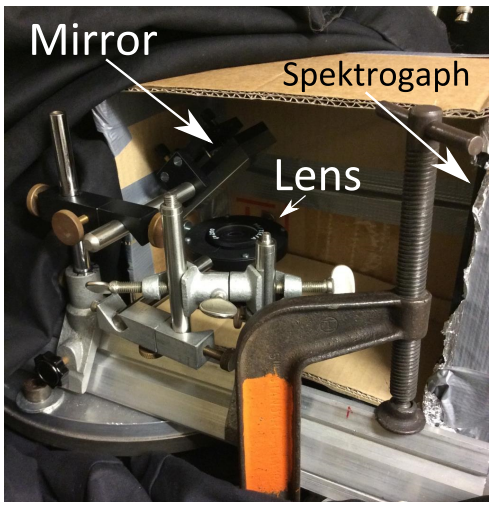

Figure 3.5: Guiding fluorescent light into the spectrograph: The light exits the apparatus and is guided through a 200 mm collecting lens and via a mirror into the grating spectrograph.

Note to the Experimentalist: Guiding the Light into the Spectrograph
Experience has shown that the lens-mirror setup offers better results: However, the initial setup is challenging, therefore, some tipps are given in the following: The easiest way to find a first signal is to use stray light of the Verdi V8 guided through the LIF baffle tube. The stray light can be seen by the naked eye, but the room needs to be darkened and a darkened housing needs to be created around the lens-mirror setup. The process still requires some adjustments, so some patience may be needed as well. It works best to guide the laser light well through the baffle tube and to slightly tilt it upwards. The stray light is best seen on a white sheet of paper. Acquisition times of 1 s are be sufficient to see a signal in the Solis software.
Once this signal is established, the second step is to use a strong atomic transition on the He droplet (e.g. Rb-D lines at 12579 and 12817 cm^{-1}) to optimize the signal. If possible, it is convenient to use the Ti:Sa laser for the excitation, since the laser is easy to set up and can be kept at hand during the measurements, in case a realignment is necessary. For the example of the Rb-D line on He droplets, the signal can be optimized, so that the laser peak of the Ti:Sa laser is at the same height or even smaller than the emission line. It is recommended to mount two iris diaphragms on the optical platform in front of the entrance window of the apparatus to mark the optimum laser pathway through the apparatus. This allows a faster adjustment of the other lasers used in the experiments.

3.3 Conclusion

In conclusion, the sequence REMPI-TOF, LIF and dispersed fluorescence experiment proved very efficient, since with REMPI-TOF finding transitions is easy and fast due to the broad and easily accessible wavelength range. A more detailed recording with a better signal-to-noise ratio is usually achieved with LIF. This is also a great precursory experiment for emission spectra, since it shows that fluorescence from the excited state exists. Its frequency can than be searched with dispersed emission spectroscopy in a subsequent experiment. This set of three experiments allows an efficient characterization of molecules on He droplets.

CHAPTER 4

Results

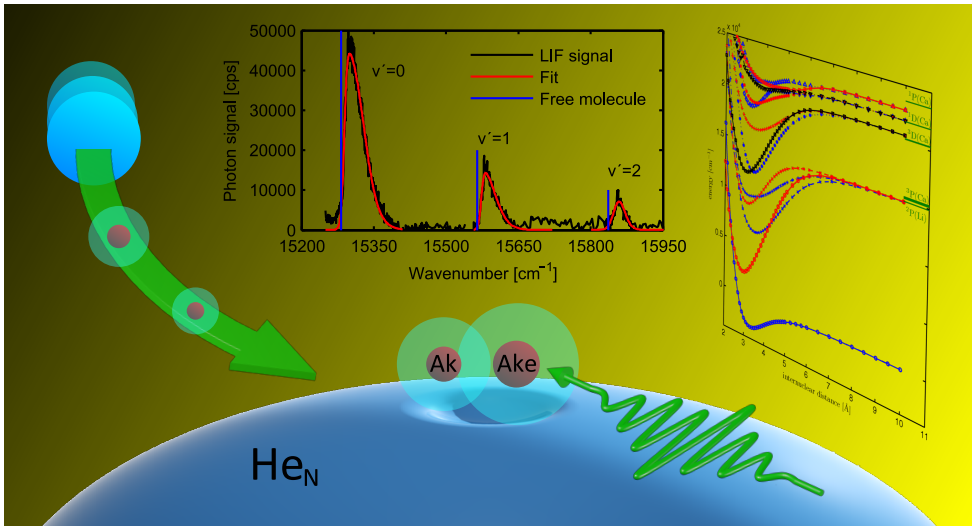

This chapter contains the experimental results related to Ak-Ake molecules on He droplets (He_N) obtained in the course of this thesis. Three molecules have been investigated: lithium-calcium (LiCa), rubidium-strontium (RbSr) and rubidium-calcium (RbCa). The experimental approach was identical for all three molecules, at first the formation of the molecule on the He droplet was determined by a REMPI-TOF mass spectrum. The advantage of mass selectivity of the REMPI-TOF method was then used to efficiently optimize the pickup for the Ak-Ake molecule signal. Secondly, a REMPI-TOF spectrum was taken over a wide wavelength range to gain an overview of the energetic landscape of the molecule. Here, the wide available wavelength range for the pulsed laser systems and the rather simple laser adjustment and signal optimization allowed an efficient recording of the signals. For both, LiCa and RbSr the REMPI spectra showed at least one vibrationally resolved transition. These transitions were investigated with LIF spectroscopy, resulting in a complementary excitation spectrum and proving that emission from the excited states is detectable. In a next step these transitions were studied with dispersed emission spectroscopy. The results of the latter allowed to deduce information about the ground state of both LiCa and RbSr. For RbSr a strong emission signal via an intermediate state was found. The experimental data of the molecules were then compared with theoretical calculations performed

by Johann Pototschnig and in the case of LiCa with other reference data. The REMPI-TOF spectrum of RbCa did not show a vibrationally resolved state, still two selected transitions were investigated with LIF spectroscopy. Since no theoretical data for excited states of RbCa are available at this point it is compared to RbSr. The data for each of the three molecules is presented in a respective section of this chapter.
Beside the investigation of Ak-Ake molecules, for every studied molecule some interesting transitions for Ak or Ake dimers where found, for Li and Li_2 the data were processed and published in [96] by Florian Lackner and for Sr_2 and Ca_2 a publication is in preparation at this point of time. The results are briefly presented in separate sections following the corresponding Ak-Ake section.

The experimental data presented in this thesis have been published in several articles (LiCa [88], RbSr [87, 92], Li_2 [96]) and some articles are still in preparation. Parts of these articles are contained in the following sections, a closer explanation is given at the beginning of each section.

4.1 Lithium-Calcium

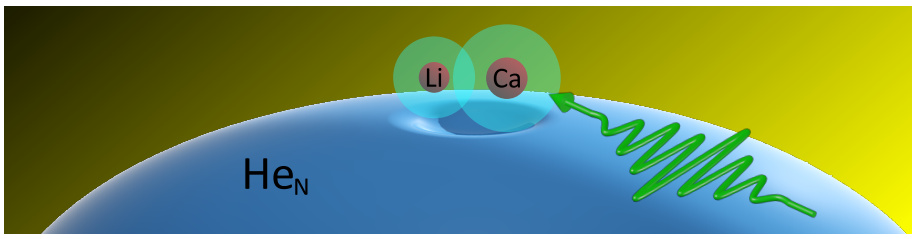

In this section the results of the investigation of LiCa on He_N are presented. LiCa was chosen as the first Ak-Ake molecule to investigate on He_N because theoretical [3, 13, 53, 55, 56, 83, 139] and experimental reference data from heatpipe [70, 146] and molecular beam [139] experiments were available. The available theoretical calculations mainly deal with the ground state, some calculation of excited states have been presented by Gopakumar et al. [53] quite recently. The most extensive studies were presented by Russon et al. [139] and Allouche et al. [3]. Our own calculations, performed by Johann Pototschnig (see fig. 4.3) extend these works to higher excited states, which allowed the assignment of previously unobserved transitions.
The experimental effort to create LiCa in a heatpipe or a molecular beam is rather large. In the latter an alloy of LiCa was formed and then vaporized by a laser, the molecular LiCa beam was then formed by a supersonic jet-expansion [139]. In the heatpipe experiments a three section heatpipe was used with Ca loaded in the center and Li in the other sections [70]. Especially for the heatpipe experiments the large background signal of singlet Li_2 was a problem. These hardships in creating the molecules and separating their signal from dimer signals are easily overcome with helium nanodroplet isolation spectroscopy. All desired combinations of Ak-Ake molecules can be formed by simply loading the successive pickup cells with the corresponding material. The signal for the Ak-Ake molecule, or the dimers (as desired) can be dynamically optimized by changing the pickup temperatures and checking the relative ion yields in a REMPI-TOF mass spectrum[1].

Within the scope of the investigation of LiCa on He_N we were able to record a REMPI-TOF spectrum in the spectral range of 15000-24500 cm^{-1}. Six transitions were found, two of which ($4^2\Sigma^+$ and $3^2\Pi$) are vibrationally resolved, which enabled the extraction of molecular parameters. The $4^2\Sigma^+$ state was additionally investigated with LIF spectroscopy and dispersed fluorescence spectroscopy.

The following text has been taken from the publication [88], except the section about the mass spectrum. The article is a joint work of Florian Lackner, Johann Potoschnig and me. The experiments were performed and the data processed by Florian Lackner and me, the theoretical calculations were done by Johann Pototschnig. Florian Lackner wrote the introduction of the paper and supervised the whole article. The theoretical section was written by Johann Pototschnig and the part about the experimental results by myself. In the following only the experimental results are presented, including only an overview of the potential energy curves of LiCa and the calculated transition probabilities to compare the theoretical and experimental data. The conclusion of the article has also been added here.

[1] A proper combination of detection devices also allows to record the respective mass signals versus the pickup temperature.

This account of the LiCa results is structured as follows: At first a mass spectrum, showing the efficient formation of LiCa on He_N is shown. The following sections contain the publication [88] and start with the description of the REMPI-TOF overview spectrum. Then the most interesting features in the spectrum are analyzed in detail. The vibronically resolved $4^2\Sigma^+ \leftarrow X^2\Sigma^+$ transition was investigated with LIF and dispersed fluorescence spectroscopy, allowing to deduce information about the LiCa ground state. A comparison of the experimental data to theoretical calculations illuminates more details of this Ak-Ake molecule. In the end the conclusion provides a short summary and outlook.

4.1.1 Mass Spectrum

Fig. 4.1 shows a mass spectrum in the range of 0-100 amu taken at different pickup temperatures for Li and Ca. The spectrum was obtained by a two-photon ionization with a DCM dye laser and a fraction of its XeCl pump laser. The spectra were recorded at a wavelength of 15299 cm^{-1} which corresponds to the maximum of the $4^2\Sigma^+, \nu' = 0 \leftarrow X^2\Sigma^+, \nu'' = 0$ transition.

Concerning the isotopes, Li has two stable isotopes at 6 amu and at 7 amu with an abundance of 7.4 % and 92.6 %, respectively. Calcium has only one significant isotope at 40 amu (96.9 %). These facts in addition to the different mass ranges of Li and Ca make the mass spectrum simple to analyze.

In fig. 4.1 the relevant masses are denoted, these are the masses which are usually seen in a REMPI-TOF mass spectrum of doped He droplets: The monomers and dimers of the dopants and monomers with one or several He atoms attached. As can be seen in fig. 4.1 the pickup temperatures $T_{Li} \sim 350\,°C$ and $T_{Ca} \sim 370\,°C$ provide an optimal signal of the LiCa molecule at 47 amu and the dimer signals are rather low (Li_2-14 amu and Ca_2-40 amu). When lowering the pickup temperature for e.g. Li, the LiCa signal rapidly decreases and the Ca dimer rises. This can be seen clearly by comparing the blue and black curve in fig. 4.1, where blue denotes the signal without Li and black without Ca. Note that for the optimized signal (red) a small contribution of $^6Li^{40}Ca$ can be seen in the mass spectrum.

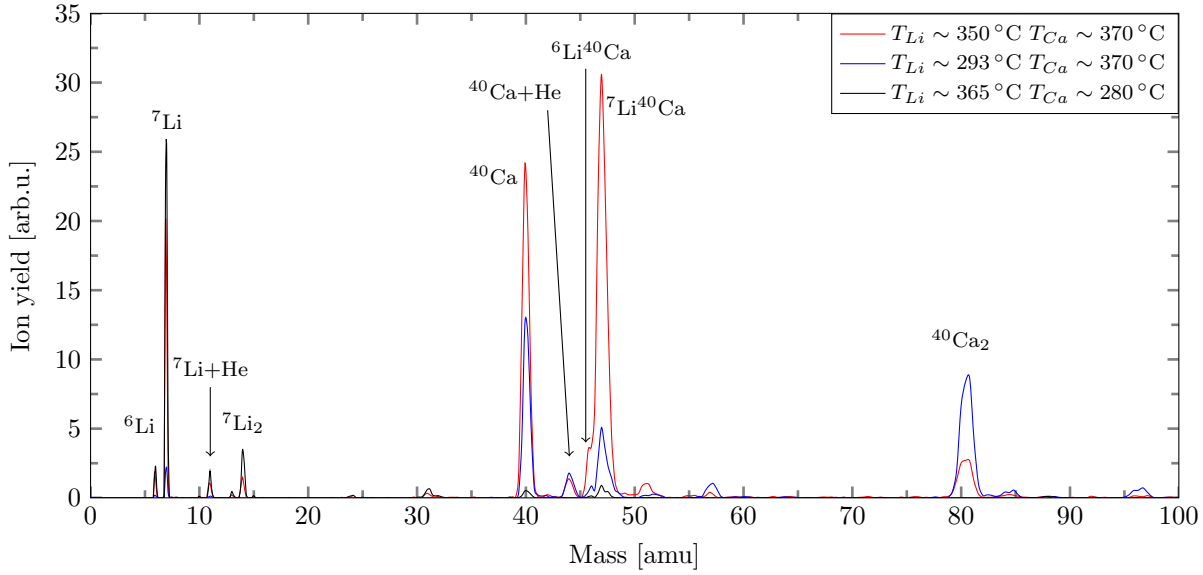

Figure 4.1: Mass spectrum of LiCa on He_N recorded at different pickup temperatures for Li and Ca.

4.1.2 REMPI-TOF Overview Spectrum

The excitation spectrum of LiCa on He_N, shown in Figure 4.2, was recorded with REMPI-TOF spectroscopy in the range of 15200 - 25500 cm^{-1}. The two lowest recorded band systems (the $4^2\Sigma^+ \leftarrow X^2\Sigma^+$ and $3^2\Pi_{1/2,3/2} \leftarrow X^2\Sigma^+$ transitions) consist of a progression of vibrational bands with a lambda-shaped peak form. For transitions into higher states the vibrational spacing could not be resolved and the bands appear as broadly extended, structureless features in the spectrum. As the density of states increases, the vibrational bands start to overlap and the complexity of the spectra increases. For three transitions, experimental data from molecular beam spectroscopy experiments are available and can be compared to our results [139]. This allows to draw conclusions on the interaction between the LiCa molecule and the droplet and the perturbation of molecular states by the droplet. In the following we discuss the recorded transitions in detail, followed by a presentation of calculated potential energy curves and transition dipole moments for LiCa as well as a comparison of calculations and experiments which allows the assignment of the higher excited states.

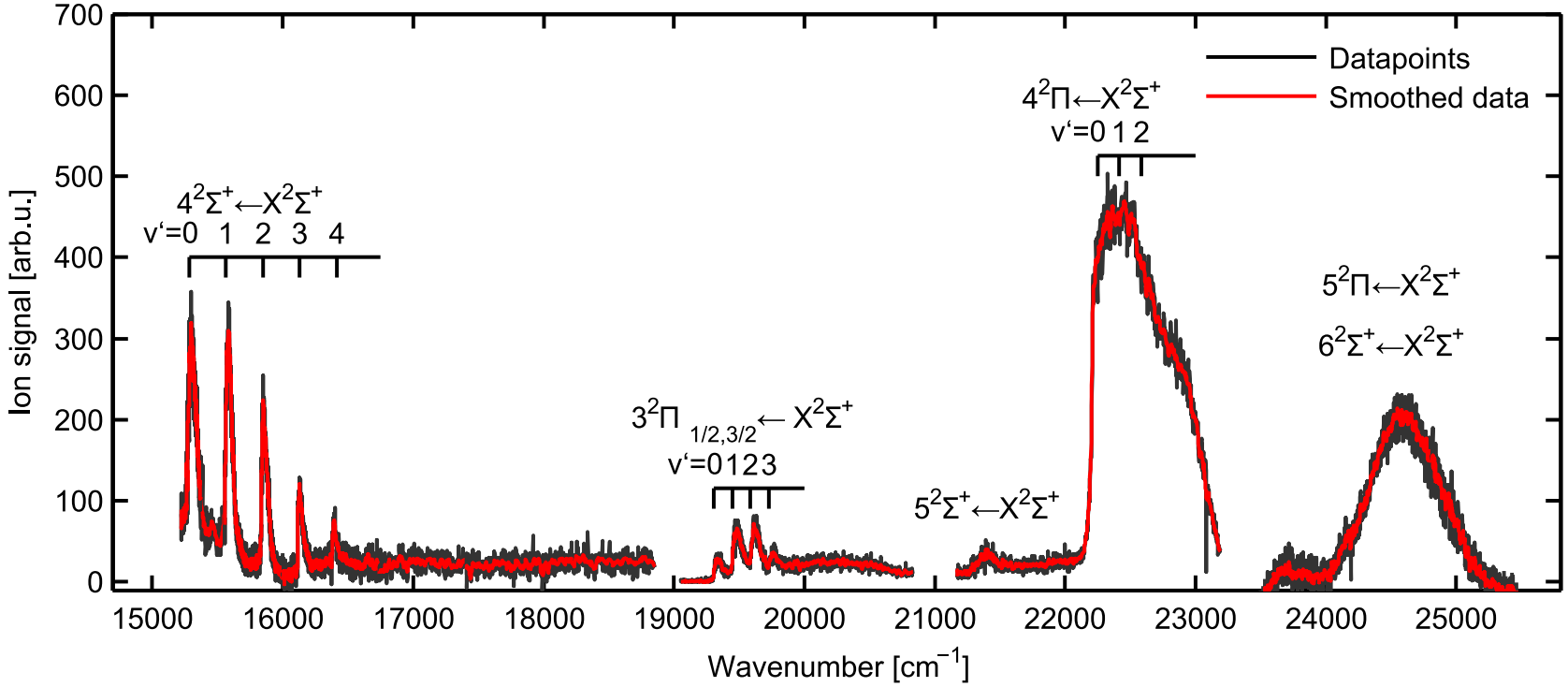

Figure 4.2: Excitation spectrum of LiCa on He_N as recorded by REMPI-TOF spectroscopy from 15200 cm^{-1} to 25500 cm^{-1}. Four band systems have been assigned to the $4^2\Sigma^+ \leftarrow X^2\Sigma^+$, $3^2\Pi_{1/2,3/2} \leftarrow X^2\Sigma^+$, $5^2\Sigma^+ \leftarrow X^2\Sigma^+$ and $4^2\Pi \leftarrow X^2\Sigma^+$ transitions of LiCa on He_N and the peak at 24500 cm^{-1} is assigned to the two overlapping $6^2\Sigma^+ \leftarrow X^2\Sigma^+$ and $5^2\Pi \leftarrow X^2\Sigma^+$ transitions. Molecular beam spectroscopy results [139] are shown on top of the signal where available.

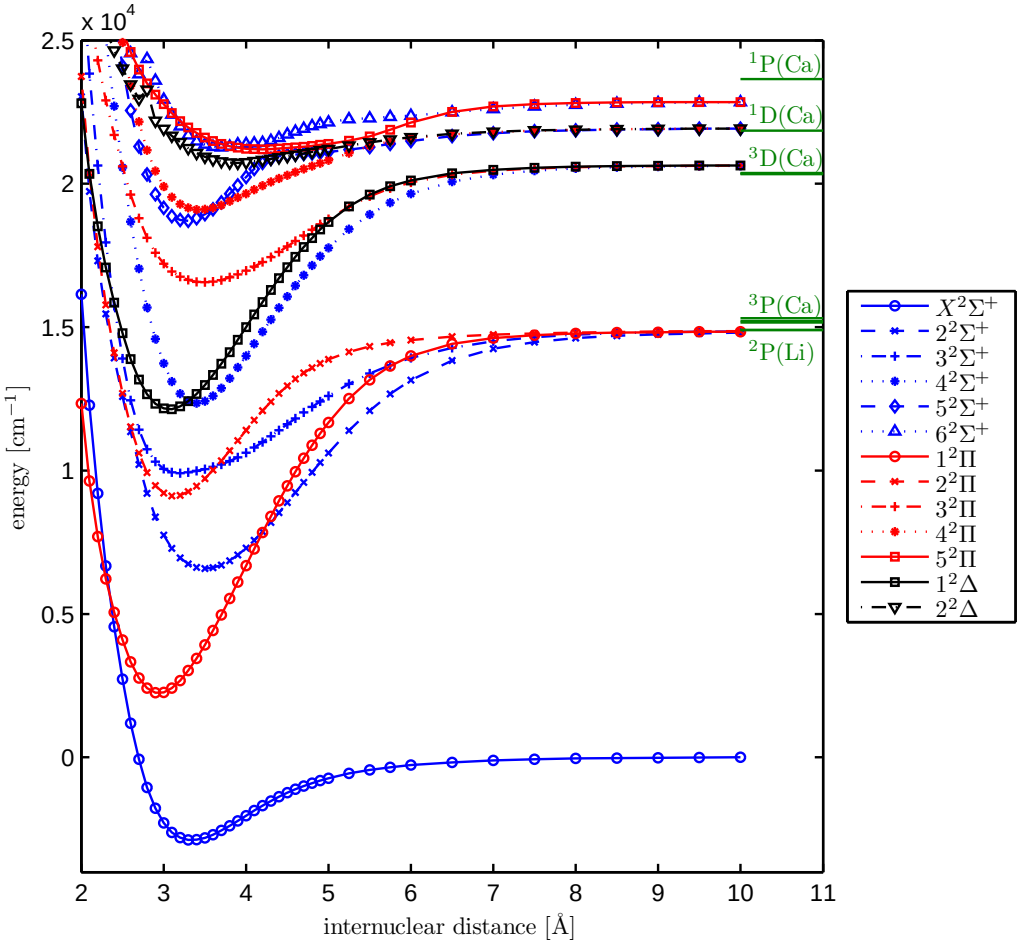

Figure 4.3: LiCa potential energy curves of the doublet manifold. The calculated asymptotes show a slight deviation from experimental atomic excitation energies (taken from the NIST-database [135]). Figure from the theory section of ref. [88].

4.1.3 Analysis of the Spectrum

The $4^2\Sigma^+ \leftarrow \mathrm{X}^2\Sigma^+$ transition

The R2PI excitation spectrum of the ^{7}Li^{40}Ca $4^2\Sigma^+ \leftarrow \mathrm{X}^2\Sigma^+$ transition is shown in Figure 4.2 in the range of 15200 - 16300 cm^{-1}. The corresponding excited LiCa molecular state correlates to the Li $2s^1$, ^{2}S + Ca $4s^1 3d^1$, ^{3}D atomic asymptote. The vibrational levels could be resolved and can be followed from $\nu' = 0$ to 4. The absence of hot bands reveals that in the presence of the low-temperature He_N environment the LiCa molecules are cooled efficiently to the lowest vibrational level $\nu'' = 0$. Hence, upon doping with Li and subsequently with Ca, the molecule is formed in the vibronic ground state $\mathrm{X}^2\Sigma^+ (\nu'' = 0)$ and the gained bond formation energy is released into the droplet. The efficient formation of LiCa demonstrates that the two surface bound species, Li [140] and Ca [138, 153], find each other on the droplet surface and a large fraction does not desorb despite the released binding energy of 2605.3(100) cm^{-1} [146]. The excess energy is carried away by evaporated He atoms, causing a droplet shrinking of about 520 He atoms, if 5 cm^{-1} binding energy of a He atom to the droplet is assumed [26]. The LiCa

molecule is more strongly bound than the alkali triplet molecules, but weaker than, for example, the sodium singlet dimers ($5942.6880(49)\,\mathrm{cm}^{-1}$ [73]) which have been investigated on the helium droplet surface extensively [65]. The observed peak structure is characteristic for surface located molecules [65,67,68,154] with strongly coupled vibrational motion to the surface of the helium droplet. Because of the similarities between Li- and Ca-helium interaction energies and the similarities between the spectra of surface bound alkali triplet molecules and the LiCa spectra we expect the LiCa molecule to reside on the surface of the helium droplet.
In order to increase the signal-to-noise ratio and in order to avoid saturation effects we investigated the $4^2\Sigma^+ \leftarrow X^2\Sigma^+$ transition additionally with LIF spectroscopy. Saturation effects can occur due to the relatively high pulse energy of the pulsed dye lasers which is needed for a reasonable R2PI signal of the molecule on the helium droplet. The LIF excitation spectrum is shown in Figure 4.4 and was recorded with a cw ring dye laser operated with DCM (∼500 mW). With LIF spectroscopy only the lowest three vibrational states could be recorded. The LIF spectrum can be compared with the spectrum in Figure 1 in reference [139]. The intensities of the $\nu' = 0$ and $\nu' = 1$ peaks in Figure 4.4 match the relative intensities in ref. [139], which demonstrates that the Franck-Condon factors (FCF) are not influenced by the interaction with the droplet for this transition. The vibrational levels obtained for the $4^2\Sigma^+$ state can be compared to spectroscopic data of free LiCa molecules [139,146]. Band origins for the free molecule are shown as vertical blue lines in Figure 4.4. It can be seen that the onset of the rising edge of the lambda-shaped peaks coincides with the free molecule value. The vibrational bands are broadened and shifted to the blue. The broad "phonon-wing" is caused by the interaction of the excited molecule with the helium droplet. The peaks have a FWHM of 30 to $40\,\mathrm{cm}^{-1}$ and no zero-phonon line could be observed. The peak structure is very similar to the shape of alkali triplet transitions with resolved vibrational levels [65,96,152]. Also the band-widths compare to alkali triplet transitions (e.g. for the Na_2 $1^3\Sigma_g^+ \longleftarrow 1^3\Sigma_u^+$ $\sim 30\,\mathrm{cm}^{-1}$ was reported [65]). For the case of alkali triplet molecules [65,67,68,154] it was concluded that a phonon-wing without zero-phonon lines suggests a stronger coupling of the vibrational motion of the molecule to the surface of the helium droplet. Hence we conclude that the LiCa molecule is also strongly coupled to the helium droplet.
The peaks in the LIF spectrum were fitted with an asymmetric 2σ-function [11,96]:

$$L(\bar{\nu}) = I(1 + e^{(\bar{\nu}-\bar{\nu_0}+w_1/2)/w_2)})^{-1}[1 - (1 + e^{(\bar{\nu}-\bar{\nu_0}-w_1/2)/w_3))^{-1}}] \tag{4.1}$$

The maximum of the second derivative of the fit function corresponds to the onset of the rising edge of the peak and hence to the origin of the vibrational band. As has been shown in reference [96] for lithium triplet molecules on helium droplets, this procedure can be used to determine molecular parameters of free molecules and the values for the origins of the vibrational bands agree within a few wavenumbers. In Table 4.1 we compare the experimentally determined vibrational band origins from references [139] and [146] with our fit results. We include the values obtained from the R2PI spectra for the 3-0 and the 4-0 band origins since they agree well with the literature values, indicating that they are not affected by high photon densities of the pulsed laser. As shown in Table 4.1, the results from helium droplet isolation spectroscopy agree very well with the molecular beam [139] and heat-pipe oven [146] experiments, demonstrating the suitability of our method for the determination of molecular parameters and for testing calculated potential energy curves of free Ak-Ake molecules. The molecular parameters T_e, ω_e and $x_e\omega_e$ have been calculated from a least squares fit to the standard expression given in Equation 2 [64].

$$T(\nu') = T + \omega_e\left(\nu' + \frac{1}{2}\right) - x_e\omega_e\left(\nu' + \frac{1}{2}\right)^2 \tag{4.2}$$

Table 4.1: Vibrational bands and molecular parameters of $^7Li^{40}Ca$ for the $4^2\Sigma^+ \leftarrow X^2\Sigma^+$ transition. One standard deviation uncertainties are given in parenthesis.

Band $\nu' - \nu''$	Energy (cm^{-1}) This work	Energy (cm^{-1}) Russon *et al.* [139]	Energy (cm^{-1}) Stein *et al.* [146]
0 - 0	15282(1)[a]	15282.2	15282.2
1 - 0	15569(3)[a]	15565.7	15562.8
2 - 0	15840(3)[a]		15836.7
3 - 0	16112(2)[b]		16104.3
4 - 0	16374(1)[b]		16366.3
T_e	15241(15)	15237.6	15240.06
ω_e	288(14)	283.5	287.84
$x_e\omega_e$	3.2(2.8)	3.57	3.86

[a] Values obtained from LIF spectroscopy. [b] Values obtained from R2PI spectroscopy.

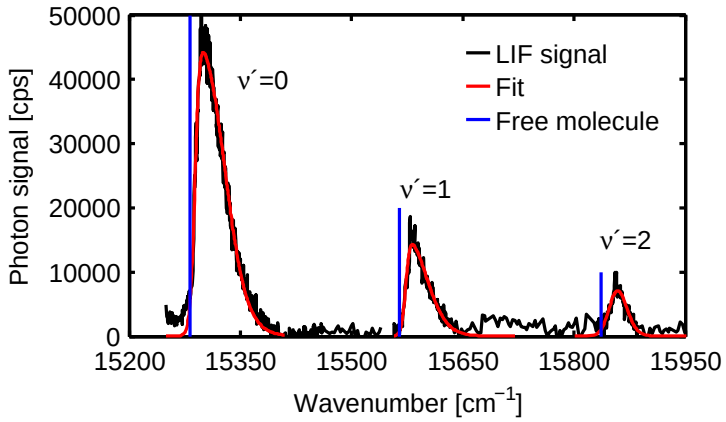

Figure 4.4: Excitation spectrum of the LiCa $4^2\Sigma^+, (\nu' = 0-2) \leftarrow X^2\Sigma^+, (\nu'' = 0)$ transition. The signal was fitted with the asymmetric 2σ function given in Equation 1. The data has been offset corrected and the red line has been smoothed. The blue lines denote the free molecule transitions as found in ref. [139]

Figure 4.5 shows the $4^2\Sigma^+ \rightarrow X^2\Sigma^+$ emission of LiCa molecules upon excitation of the $4^2\Sigma^+$ $\nu' = 1$, 2 and 3 vibrational levels at 15585, 15857 and 16130 cm^{-1}, respectively. The cw laser was tuned to the phonon-wing maximum of each transition on the helium droplet. Four peaks corresponding to the molecular 0 - 1, 0 - 0 and 1 - 1 transitions and the Li $2p \rightarrow 2s$ transition can be seen in the spectra. The observed fluorescence light in the spectrum originates only from free molecules which leave the droplet upon laser excitation. Fluorescence light could only be detected from the lowest two vibrational levels, indicating a droplet mediated cooling of the LiCa molecules in the excited states prior to the emission. Similar results have been reported for the emission spectra after the excitation of alkali dimers [20, 65]. The observation of the Li $2p \rightarrow 2s$ emission indicates that a considerable fraction of the molecules fragments into Ca and excited Li atoms. Note that excited Ca atoms could not be detected in this experiment because, in this energy range, only the lowest metastable triplet P states can be populated upon fragmentation. Their long lifetime (e.g. $\sim$4.2 μs for the Ca $^3P_1$ state [135], the upper state of the strongest inter-combination line) forbids a detection in our experiment. A comparison of the three recorded spectra shows that the two signals recorded upon excitation of the $\nu' = 1$ and $\nu' = 2$ levels do not differ strongly, except for an increased Li atomic emission at the former. As can be seen from the spectra, the majority of molecules from which fluorescence light could be detected, are in the vibrational ground state $\nu' = 0$. We conclude that the cold helium environment induces a relaxation of the molecules before they leave the droplet. This

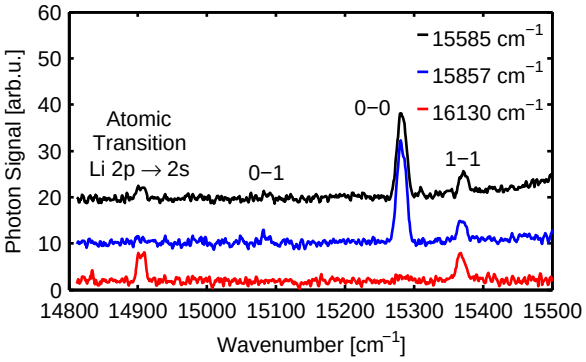

Figure 4.5: Spectra of the $4^2\Sigma^+ \rightarrow X^2\Sigma^+$ emission of LiCa molecules formed on helium nanodroplets. Emission was collected upon excitation of $\nu' = 1$, 2 and 3 in the $4^2\Sigma^+$ state which is shown as black, blue and red line, respectively. Four peaks corresponding to the molecular 0 - 1, 0 - 0 and 1 - 1 transitions and the Li 2p → 2s transition can be seen in the spectra.

demonstrates that the cooling mechanism is very efficient in this case. The striking difference at the excitation of $\nu' = 3$ is the absence of transitions originating from $\nu' = 0$, i.e. the 0-0 and 1-0 line, accompanied with an increased Li atomic emission. This suggests that in this case for the two competing underlying processes, relaxation and desorption, the latter is faster and prevails. The observation of an increased Li atom signal from the D lines is unexpected because predissociation of the $4^2\Sigma^+$ state upon interaction with the crossing $1^4\Sigma^+$ state was reported to occur above $\nu' = 9$ [146]. We think that this observation is related to the interaction between molecule and helium droplet, where due to the presence of the droplet it could also be possible that the $1^2\Delta$ state affects the dynamics of the excited molecule. Our recorded emission spectra demonstrate that the helium droplet isolation technique can be used for the preparation and investigation of free molecules, that have desorbed from the droplets upon excitation. Most importantly, the recorded emission spectra give insight into the vibrational levels of the ground state. We think that in further experiments these free molecules can be investigated upon formation on the droplet with additional lasers, allowing spectroscopy of cold tailored molecules without restricted resolution due to the interaction with the droplet.

The $3^2\Pi_{1/2,3/2} \leftarrow X^2\Sigma^+$ transition

Figure 4.6 shows a detailed view of the $3^2\Pi_{1/2,3/2} \leftarrow X^2\Sigma^+$ transition of LiCa on He_N. The $3^2\Pi$ excited molecular state adiabatically correlates to the same separated atom limit as the $4^2\Sigma^+$ state discussed above (Li $2s^1$,^{2}S + Ca $4s^1 3d^1$, ^{3}D). The data has been fitted with Equation 1, the band origins of the vibrational bands correspond to the free molecule transitions and have been obtained by calculating the maximum of the second derivative of the fit. The FWHM of the peaks is in the range of 80 cm^{-1}. In Table 4.2 we compare our results with those of a molecular beam experiment [139], which are, to our knowledge, the only existing experimental data for this transition. The vibrational spacing as obtained by the fits is within several wavenumbers of the literature values. Please note that the values for the vibronic transitions are compared to the $3^2\Pi_{1/2}$ molecular data, which follows from the fit. The molecular constants have been obtained by a least squares fit to the standard expression [64], Equation 2. In this case the parameter $x_e\omega_e$ was set to zero, since an inclusion of this parameter resulted in large uncertainties of the molecular parameters. The free molecule values for the parameters T_e and ω_e were calculated from the values given in Table II in ref. [139] As can be seen from Table 4.2, the determined parameters

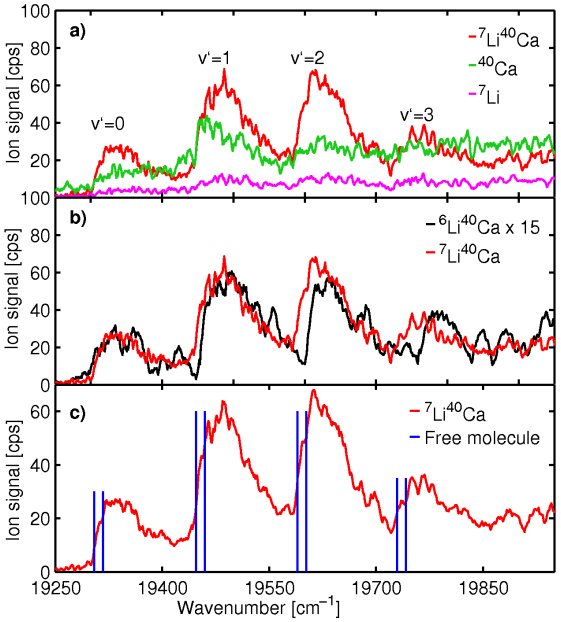

Figure 4.6: Close-up of the REMPI-TOF signal of the $3^2\Pi_{1/2,3/2} \leftarrow X^2\Sigma^+$ transition. Plot a) shows a comparison of the atomic ^{7}Li and ^{40}Ca ion signals to the molecular $^7Li^{40}Ca$ ion signal. Plot b) shows the signal for the different isotopomers of LiCa: $^7Li^{40}Ca$ and $^6Li^{40}Ca$, where the latter signal has been scaled by a factor of 15 because of the low abundance of the ^{6}Li isotope. In c) the effect of spin-orbit splitting can be seen in the form of a slight kink in the rising edge of each vibrational level, which is situated between the corresponding spin-orbit split $^2\Pi$ components of the free molecule transitions, indicated by vertical blue lines.

lie well within the one σ standard deviation interval and differ only a few wavenumber from the free molecule values. The relative intensities of the peaks do not allow to draw conclusions about the Franck-Condon factors in this case, since the signal has not been normalized with the relative laser pulse energy over the wavelength range.
To highlight the effects which can be seen in the recorded signal, Figure 4.6 has been divided into three sections. Plot a) shows a comparison of the atomic Li and Ca ion signal to the LiCa molecular ion signal. Atomic calcium follows the trend of LiCa, whereas the atomic Li signal shows only a very weak structure. The $3^2\Pi$ potential energy curve is crossed by the $1^4\Sigma^+$ curve which gives rise to a predissociation of the LiCa molecule, as has been suggested in

Table 4.2: Vibrational bands for the $3^2\Pi_{1/2} \leftarrow X^2\Sigma^+$ transition of $^7Li^{40}Ca$ and $^6Li^{40}Ca$ and molecular parameters for the $3^2\Pi_{1/2}$ state of both isotopomers. One standard deviation uncertainties are given in parenthesis.

	$^7Li^{40}Ca$		$^6Li^{40}Ca$	
Band	Energy (cm^{-1})	Energy (cm^{-1})	Energy (cm^{-1})	Energy (cm^{-1})
$\nu' - \nu''$	This work	Russon *et al.* [139]	This work	Russon *et al.* [139]
0 - 0	19302(2)	19304.6	19295(2)	19302.9
1 - 0	19436(2)	19447.8	19449(3)	19456.0
2 - 0	19581(1)	19589.6	19600(6)	19607.0
3 - 0	19721(2)	19729.3	19757(1)	19757.3
T_e	19330(15)	19330.6[a]	19325(8)	19330.6[a]
ω_e	140.2(6.6)	144.5	153.7(3.6)	154.2[a]

[a] Calculated from values given in Table II in ref. [139]

ref. [70, 139, 146]. The $1^4\Sigma^+$ curve is purely repulsive above the lowest vibrational level of the $3^2\Pi$ state (case c$^-$ according to Mulliken's classification of predissociation cases [99,117]) leading to ground state Li atoms and Ca atoms excited into their $4s^14p^1$,^{3}P state in the separated atom limit. As suggested in ref. [146] the predissociation rate seems to be relatively high. We attribute the observation of the high Ca ion signal that follows the LiCa ion signal, to predissociated molecules. However, helium droplets are known to induce relaxation processes, which have been observed in form of intersystem crossings in alkali triplet dimers [65] and quartet trimers [66] or spin relaxation in atoms doped to helium droplets [78, 105]. The LiCa molecules will interact with the helium droplets during the predissociation which can lead to atomic fragments in states differing from the products expected from the adiabatically correlating atomic states of the $1^4\Sigma^+$ molecular state. Hence predissociation of the LiCa molecule on a helium droplet can give rise to both, excited Ca and Li fragments. A contribution of ground state Li atoms to the Li^+ signal is unlikely, because we do not observe a background signal caused by the free atom beam, which is always present in our detection chamber due to our pickup design. In light of this discussion we think that the following effects are responsible for the signals in Figure 4.6 a): The majority of molecules is ionized in a two-photon ionization process and form a stable molecular LiCa ion. A fraction of molecules predissociates, resulting in a Ca ion signal and also a weak Li ion signal caused by the interaction with the droplet. In both cases, for the excited Li and Ca, two photons are necessary for the ionization. A competing process is the fragmentation of the molecule upon absorption of a third photon, which will also contribute to both the Li and the Ca ion signal.
At the $3^2\Pi \leftarrow X^2\Sigma^+$ LiCa transition we were able to separate the signals of $^6Li^{40}Ca$ and $^7Li^{40}Ca$ and thus obtain a spectrum for both isotopomers, which is shown in Figure 4.6 b). Despite the very weak $^6Li^{40}Ca$ signal, due to the low abundance of ^{6}Li (7.4 %), the isotope shift can be clearly seen and the trend of an increasing shift for higher excited vibrational levels is obvious. The isotope shift is well comparable to the values given in ref. [139] as shown in Table 4.2. Also the molecular parameters T_e and ω_e for both isotopomers are in good accordance with the literature values.
As has been shown in ref. [139] the $3^2\Pi$ state has a fairly large spin-orbit (SO) constant and Hund's case (a) is appropriate for the description of the coupling of spin and orbital angular momentum with the molecular axis. The $3^2\Pi$ state splits into two spin-orbit sub-bands. Due to the broadening of the lines by the interaction with the He droplet, they are hard to resolve. Despite this, in our data a small effect of the spin-orbit splitting (SO constant A'$_0$ =13.3 cm^{-1}, for $\nu' = 0$ [139]) can be seen in form of a slight kink in the rising edge of each vibrational band in the $^7Li^{40}Ca$ spectrum. This effect is highlighted in the Figure 4.6 c), where the kink can be seen for each vibrational level $\nu' = 0 - 3$ between the band origins of the two spin-orbit split $^2\Pi$ components of the free molecule, indicated by the vertical blue lines.
It is remarkable that the value of the spin-orbit constant seems to be conserved despite the presence of the droplet. Assuming the molecule lies flat on the surface of the droplet, the symmetry of the system will be reduced and an effect on the SO constant would be expected [12]. However the coupling of spin and orbital angular momentum to the intermolecular axis seems to be much stronger than the influence of the droplet which would make the effect very small. If on the other hand the molecular axis of the LiCa molecule was aligned perpendicular to the droplet surface, the symmetry around the internuclear axis would also be conserved. This would be another explanation for the observed SO splitting.

Higher excited states

In this section the single structures which can be seen in Figure 4.2 in the energy region above 21250 cm^{-1} are discussed. The band at 22000 cm^{-1} has been assigned to the $4^2\Pi \leftarrow X^2\Sigma^+$ transition, where the upper level adiabatically correlates to Li $2s^1$,^{2}S + Ca $4s^13d^1$, ^{1}D in the separated atom limit. The transition extends from 22150 cm^{-1} to 23100 cm^{-1}, shows a steep rising edge and a high signal on the low energy side and a broad shoulder to the high energy side. The transition is not vibrationally resolved. The $4^2\Pi$ state correlates to a Ca singlet state, in contrast to the $4^2\Sigma^+$ and $3^2\Pi$ states described above, which correlate both to the same Ca ^{3}D state. This is noteworthy considering the interaction of Ca with He. Calculations have shown that the CaHe potential for the Ca $4s^13d^1$, ^{1}D state has a pronounced minimum for its molecular Π sub-state, while all molecular sub-states corresponding to Ca $4s^13d^1$, ^{3}D are repulsive or very weakly bound [30]. The lack of vibrational resolution in the $4^2\Pi \leftarrow X^2\Sigma^+$ excitation spectra indicates a stronger interaction of the excited molecule with the droplet surface. The steep rising edge of the peak indicates that the laser excitation starts at the lowest vibrational transition, which is confirmed by our calculations. The onset of the rising edge is shifted to the red by $\sim$ 100 cm^{-1} as compared to the values found in ref. [139]. Our calculations show that the $4^2\Pi \leftarrow X^2\Sigma^+$ transition has a very high transition dipole moment with a maximum of the Franck-Condon envelope at the $0-0$ transition, which could cause an easy saturation of this transition. We have recorded this transition with various laser pulse energies. While the shoulder on the high energy side does broaden with increasing laser energy, the steep rising edge does not show a significant energy dependence.
An analysis of the atomic signals again shows that Ca follows the LiCa signal, however at this level of excitation there is a large number of crossings and avoided crossings of molecular potentials which, together with the influence of the He_N environment increase the possibility of the LiCa molecule being predissociated. The REMPI-TOF signal shows a weak CaHe ion signal which follows the LiCa ion signal in the region of the $4^2\Pi \leftarrow X^2\Sigma^+$ transition (not shown). We explain this in accordance with the detection of fragments in the $3^2\Pi_{1/2,3/2} \leftarrow X^2\Sigma^+$ transition: He droplets could act as an intermediate and lead from an excited LiCa*-He_N system via a LiCa*-He-He_N transition state to the formation of Ca*He exciplexes. Similar exciplex formation processes have been found for Ak-He_N systems. [137,151] The fact that a CaHe ion signal is only detected at the $4^2\Pi \leftarrow X^2\Sigma^+$ transition implies that the binding character of the Ca*(^{1}D)He $^1\Pi$ potential is responsible for the formation of Ca*He.
Two more LiCa transitions have been found, one weak transition between 21250-21500 cm^{-1} and a strong transition between 24000-25250 cm^{-1}. The assignment of these states to molecular transitions is based on our calculations and will be treated in detail below.

4.1.4 Comparison of Theoretical to Experimental Results

The calculated potential energy curves (PECs, see fig. 4.3) and transition dipole moments (TDMs, see fig. 5 in ref. [88] and ref. [133]) for the $4^2\Sigma^+ \leftarrow X^2\Sigma^+$ transition confirm our interpretation of the experimental data. We find good agreement between calculated and experimentally determined band origins with deviations below 20 cm^{-1}. The trend of decreasing transition probability with increasing vibrational quantum number ν' is in accordance with the experimental findings.
The theoretical prediction for the $3^2\Pi_{1/2,3/2} \leftarrow X^2\Sigma^+$ transition is too high: The calculated potential energy curve (see Figure 4.3) lies above the atomic value in the separated atom limit. Despite this inaccuracy in the absolute position the vibrational spacing and the isotope shifts

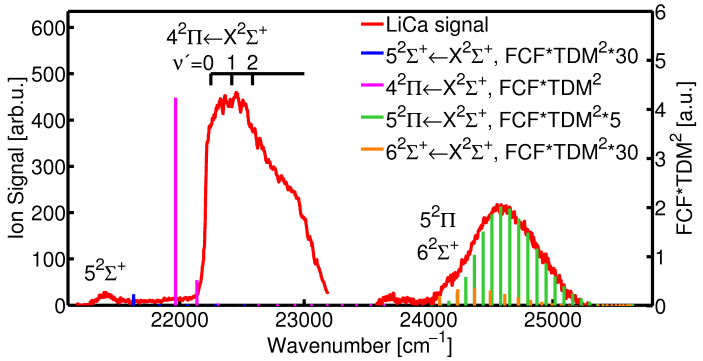

Figure 4.7: REMPI-TOF signal in the range of 21100-25800 cm^{-1}. The red curve shows the smoothed data, the colored vertical lines represent the calculated Franck-Condon factors weighted with the respective transition dipole moments. The FCFs have been scaled in order to fit to the signal, the scaling factors are given in the legend. The transitions into the $5^2\Sigma^+$, $5^2\Pi$ and $6^2\Sigma^+$ states have not been observed before and are assigned with the help of our calculations. The short black vertical lines above the $4^2\Pi \leftarrow X^2\Sigma^+$ transition refer to values from ref. [139] The red vertical line near 22000 cm^{-1} represents our calculated 0-0 band position.

are well reproduced by the calculations.
Figure 4.7 shows the experimental and the calculated excitation spectra in the range between 21100 to 25500 cm^{-1}. The theoretical spectrum was obtained by multiplying the FCF with the (TDM)^2 of the respective state at 3.4 Å. The observed bands have been assigned to the $5^2\Sigma^+$, $4^2\Pi$, $6^2\Sigma^+$ and $5^2\Pi$ states, respectively. Although calculations predict an extremely low TDM for the $5^2\Sigma^+ \leftarrow X^2\Sigma^+$ transition, a weak signal originating from this transition is experimentally observed. This state did not occur in previous experiments. Its transition probability might be enhanced by interactions with the helium environment. The theoretically predicted values are at slightly higher wavenumbers than the experimental values. The next structure in the spectra could clearly be associated with the $4^2\Pi$-state. This state was also investigated experimentally by Russon *et al.* [139], but due to the interaction with the droplet the vibrational states could not be resolved in the experiment. For the $4^2\Pi$-state the interaction between the helium and the diatomic molecule is relatively strong, which is indicated by the deep potential between a Ca atom in this excited state and a He atom, as can be seen in the diatomic potential curves in reference [30]. The deviation between the theoretical and experimental line positions can be explained by taking a look at Figure 4.3. The two highest $^2\Pi$-states show an avoided crossing, which means that the $4^2\Pi$-state is associated with the ^{1}P Ca atomic limit. The potential at large internuclear separation is about 300 cm^{-1} below the atomic value [135], which corresponds to the difference between the theoretical and experimental values for the $4^2\Pi \leftarrow X^2\Sigma^+$ transition. Based on our calculations, we can assign the structure between 24000 and 25000 cm^{-1} to the $6^2\Sigma^+$ and $5^2\Pi$ states. The calculated Franck-Condon factors are in excellent agreement with the experimentally observed structure and the deviation of the position is less than 100 cm^{-1}. This good correspondence is probably related to the good reproduction of less than 100 cm^{-1} of the atomic ^{1}D (Ca) state at large internuclear separations. Due to the avoided crossing, this agreement is transferred to these states. The main features of this transition can be explained by the $5^2\Pi$-state which has a strong transition dipole moment. The vibrational states of this transition are not resolved because of the narrow vibrational spacing of ω_e =75 cm^{-1}. The rising edge deviates from the prediction, which can be explained by the additional contribution of the $6^2\Sigma^+$ state to the signal. For this structure a significant Li ion-signal was obtained, in contrast to

all other recorded transitions. This can be explained by the interaction with even higher states. For the limit of separated atoms the states Li $3s^1$, ^2S + Ca $4s^2$, ^1S and Li $2p^1$, ^2P + Ca $4s^14p^1$, ^3P would follow, both including an excited Li atom. The PECs of states converging to excited Li approach the $6^2\Sigma^+$ and $5^2\Pi$ states and for the $6^2\Sigma^+$ state an avoided crossing is indicated by the potential form and a discontinuity in the transition dipole moment (Figures 4.3, TDMs are not shown in this work, see ref. [88]).

4.1.5 Conclusion

We have presented a comprehensive experimental and theoretical study of the LiCa molecule. We show that these molecules can be formed very efficiently on helium nanodroplets by using a sequential pickup scheme. Our results represent the first experimental observation of mixed alkali-alkaline earth molecules on helium nanodroplets. A comparison of our experimental results for the $X^2\Sigma^+$, $4^2\Sigma^+$, $3^2\Pi$ and $4^2\Pi$ states with those of previous molecular beam [139] and recent heat-pipe oven [70,146] experiments reveal that the determined molecular parameters of LiCa on He_N lie within a few wavenumbers of the gas phase values. This demonstrates the capability of helium droplet isolation spectroscopy for the characterization of alkali-alkaline earth molecules. The interaction between droplet and molecule manifests itself in the appearance of phonon-wings in the spectra. They are caused by the coupling of the vibrational motion of the LiCa molecule to excitation modes of the helium droplet and extend from the vibronic band origin towards higher energies. For the $4^2\Sigma^+$ and $3^2\Pi$ states the vibrational spacing in combination with narrow phonon-wings allows the separation of vibrational states. The narrow, lambda-shaped peak form, which is typical for surface bound molecules [65], indicates a surface location of LiCa.
Ab initio quantum chemical calculations of potential energy curves, transition dipole moments, Franck-Condon factors and permanent dipole moments support our spectroscopic study of the LiCa molecule. The 19 lowest lying potential energy curves were determined by using a multireference configuration interaction calculation. Based on our calculations we were able to identify the previously unobserved transitions into the $5^2\Sigma^+$, $5^2\Pi$ and $6^2\Sigma^+$ states. Our results for the lower excited states and the ground state of LiCa agree well with previous calculations [3,13,53,55,56,83] and extend the previous works on LiCa to higher excited states. Despite the perturbation of the molecule by the droplet, the resolution of the experimental spectra obtained for LiCa is sufficient to test calculated potential energy curves.
LiCa has been taken as an alkali-alkaline earth prototype molecule because of the available experimental and theoretical reference data. The experimental results serve as a proof of principle and demonstrate that formation of alkali-alkaline earth molecules on helium nanodroplets is possible. Our results indicate that the preparation of various tailor-made alkali-alkaline earth molecules on helium droplet will be possible, opening a new route for the characterization of these molecules. This could be an important contribution for the preparation of ultracold molecules from ultracold atoms, a process which relies on the knowledge of accurate potential energy curves. We think that the most promising candidate for the production of ultracold Ak-Ake ground state molecules is the RbSr molecule [125]. Both, Rb and Sr atoms are surface bound species and have been well characterized on helium droplets. Based on our results for LiCa we conclude that the formation of RbSr molecules for the determination of molecular parameter is feasible. Beyond the scope of this article, our results suggest that the molecules which desorb upon excitation can be further investigated with additional lasers, which would overcome resolution constraints and lead to ro-vibrationally resolved spectra.

4.2 Lithium Atoms and Dimers on Helium Droplets

In the course of our investigation of LiCa on He_N we found some additional features in the REMPI-TOF signal at the Li and Li_2 mass. These features were identified as the Li 3p←2s and 3d←2s non-resonant two-photon transition and the Li_2 $2^3\Pi_g \leftarrow 1^3\Sigma_u^+$ transition. A closer analysis of these transitions led to the publication [96] prior to the LiCa article. The main focus of the present work is on Ak-Ake molecules, however a short summary of this publication will be given here. On the one hand it is interesting to compare the results of Ak atoms, dimers and Ak-Ake molecules on He droplets and on the other it is noteworthy that these results were obtained simultaneously with the LiCa measurements. Since the experimental measurements were the same as in LiCa, they have been performed by Florian Lackner and myself. The analysis of the data and preparation of the article was done by Florian Lackner, theoretical calculations by Johannes Poms and Johann Pototschnig.

Experimentally both Li and Li dimer transitions have been recorded by REMPI-TOF spectroscopy, the pickup temperature for Li was set to $\sim 350\,^\circ$C. The atomic transitions were excited by a non-resonant two-photon excitation of the pulsed dye laser engaged (DCM, 5.2 mJ) and ionized with a fraction of the XeCl pump laser. Li_2 has been excited and ionized by two photons of the dye laser (Coumarin 2 and Stilbene 3 with 0.3 mJ and 0.5 mJ respectively).

4.2.1 Li atoms on He Droplets

It is important to note that atomic transitions on He droplets are theoretically described by a pseudo-diatomic model, using Hund's case (a) notation [93] [2]. Here, the droplet is seen as a giant atom forming a diatomic molecule with the dopant. The energy levels are then described by the projection Λ of the angular momentum $\vec{L}$ onto the molecular axis (connecting the center of the droplet to the dopant). The projection of the spin Σ can be neglected in the case of Li (SO constant $A_{Li(^2P)}$=0.34 cm^{-1} [135]). In order to provide an unambiguous assignment, the atomic transition is denoted first and the molecular given in brackets, e.g. 3d(Δ)←2s(Σ). For a two-photon excitation transitions from the Σ ground state into Σ, Π and Δ molecular substates are allowed.
An assignment of the structures in the REMPI-TOF signal to atomic transitions is supported by comparison to other Ak-He_N systems, see e.g. Na-He_N in ref. [104] and by considering the Li-He_m (m=1-3) signals, called exciplexes [137], shown in fig. 4.8. The bare Li signal is not shown in the figure, since the background of Li ions created by a resonant two photon ionization via the 2p(Σ) state is too large.
In the context of the pseudo-diatomic model the 3p state of Li splits into a Π and a Σ molecular substate (disregarding SO splitting). It is known that an excitation of Ak-He_N systems into states with $\Lambda > 0$ leads to an exciplex formation, while excitations of Σ states mainly lead to a desorption of bare Ak atoms from the droplet [91]. This allows the assignment of the peak at

[2] Note that Ak-He_N systems are very well investigated experimentally and theoretically, see e.g. refs. [21, 46, 93–95, 104, 106, 130, 157].

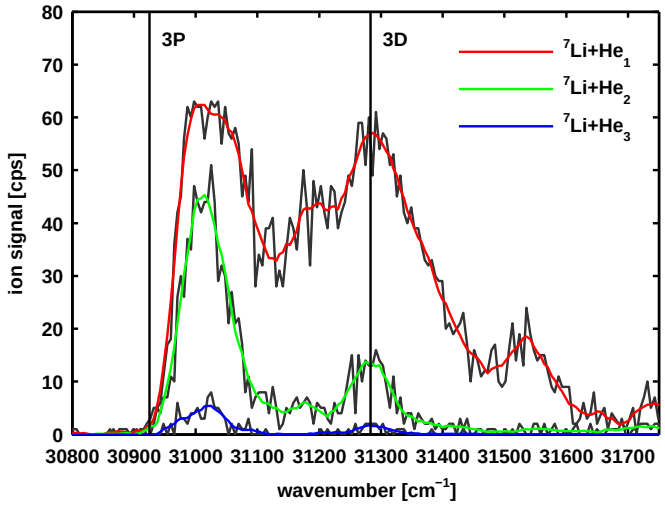

Figure 4.8: ^{7}Li-He$_m$ (m=1-3) excitation spectrum recorded with REMPI-TOF. The structures are assigned to the atomic 3p and 3d states (balck vertical lines) in the scope of the pseudo diatomic model. The transitions are excited via non-resonant two-photon excitation, hence the laser wavenumber has been multiplied by two.

$31016 \pm 2\,\mathrm{cm}^{-1}$ to the 3p(Π) state. The feature between the 3p(Π) state and the 3d line can only be clearly seen in the Li-He$_1$ signal and is therefore assigned to the 3p(Σ) state. The structure at higher energies correlating to the molecular substates of the 3d←3s transition can be compared to Rb-He$_N$ [94]. The main peak at $31278 \pm 5\,\mathrm{cm}^{-1}$ is accompanied by a significant exciplex formation, suggesting an assignment to the 3d(Δ) molecular substate. Note that this transition is nearly unshifted with respect to the atomic transition, which is unusual for low-lying atomic transitions on He droplets.
The peak at $31536 \pm 10\,\mathrm{cm}^{-1}$ is subsequently assigned to a part of the 3d(Π) or 3d(Σ) state.
A theoretical treatment of the transition is given in the article [96].

4.2.2 Li dimers on He Droplets

Figure 4.9 a) shows the Li dimer transition in the spectral range of 21250-24000 cm^{-1} recorded with REMPI-TOF spectroscopy. The signal for all isotopologues (^{6}Li$_2$, ^{6}Li^{7}Li, ^{7}Li$_2$) is given. The abundance of the isotopologues is ^{6}Li$_2$-0.55%, ^{6}Li^{7}Li-13.71%, ^{7}Li$_2$-88.71%, due to the low abundance of ^{6}Li$_2$ the signal has been multiplied by a factor of 10.
Panel b) of fig. 4.9 shows the calculated Franck-Condon-factors (FCFs) for the $2^3\Pi_g \leftarrow 1^3\Sigma_u^+$ transition [3]. The calculation was performed with the LEVEL 8.0 program of LeRoy [98], using the potential energy curves given in ref. [71]. The FCFs are given in arbitrary units and have been scaled to the $\nu' = 1$ transition, since the $\nu' = 0$ transition tends to be saturated in REMPI-TOF experiments due to the high pulse energy required to obtain a good signal. This has also been shown for LiCa (see section 4.1 p51) and RbSr (see section 4.3 p67). The trend of the experimental data is well reflected by the intensity distribution of the calculated vibrational band (except the $\nu' = 0$ line).

[3] Ak dimers on He droplets are preferably formed in their triplet state, due to the fragility of the Ak-He$_N$ system. This has been found for several Ak dimers on He droplets such as Na_2 [65], K_2 [65], Rb_2 [12, 20] and Cs_2 [45].

The structure shown in fig. 4.9 a) is assigned to the molecular $2^3\Pi_g \leftarrow 1^3\Sigma_u^+$ transition, based on the calculations. Due to cold environment provided by the droplet the transitions start from the vibrational ground state $1^3\Sigma_u^+(\nu'' = 0)$. Transitions into several vibrational levels of the electronically excited state ($\nu' = 0 - 11$) can be identified. Each vibronic transition shows the characteristic lambda-shaped broadening which is due to the coupling of the molecular motion to surface phonons of the droplet [67, 68]. At this point it is interesting to compare the singlet ($1^1\Sigma_g^+$) and triplet ($1^3\Sigma_u^+$) ground states of Ak molecules: For Na_2 it has been shown that transitions from the singlet ground state lead to narrow zero phonon lines and separated phonon-wings, while transitions from the triplet ground state lead to broad lambda-shaped features, as also obtained for Li_2. The absence of a distinct zero phonon line suggests a strong coupling of the Li dimer to the droplet. It has been shown for Na_2 [65, 67, 68] and also for the Ak-Ake molecules on He droplets in the corresponding sections of this thesis that the onset of the rising edge of the lambda-shaped lines lies within a few wavenumbers of the free molecule transition. This fact has been used to extract molecular parameters of Li_2 by the method described for LiCa (section 4.1 p51 and RbSr (section 4.3 p67). Note that the article about Li and Li_2 was published before the LiCa article, therefore the Li_2 served as a testing ground for this method. The availability of experimental high resolution data [102, 167] for the $2^3\Pi_g$ of Li_2 allowed a comparison of free molecular data to the values obtained for Li_2 on He droplets. As presented in table 1 of ref. [96] the obtained molecular parameters are in good accordance to reference values. This provided a good verification that free molecular parameters can be obtained from molecules on He nanodroplets.

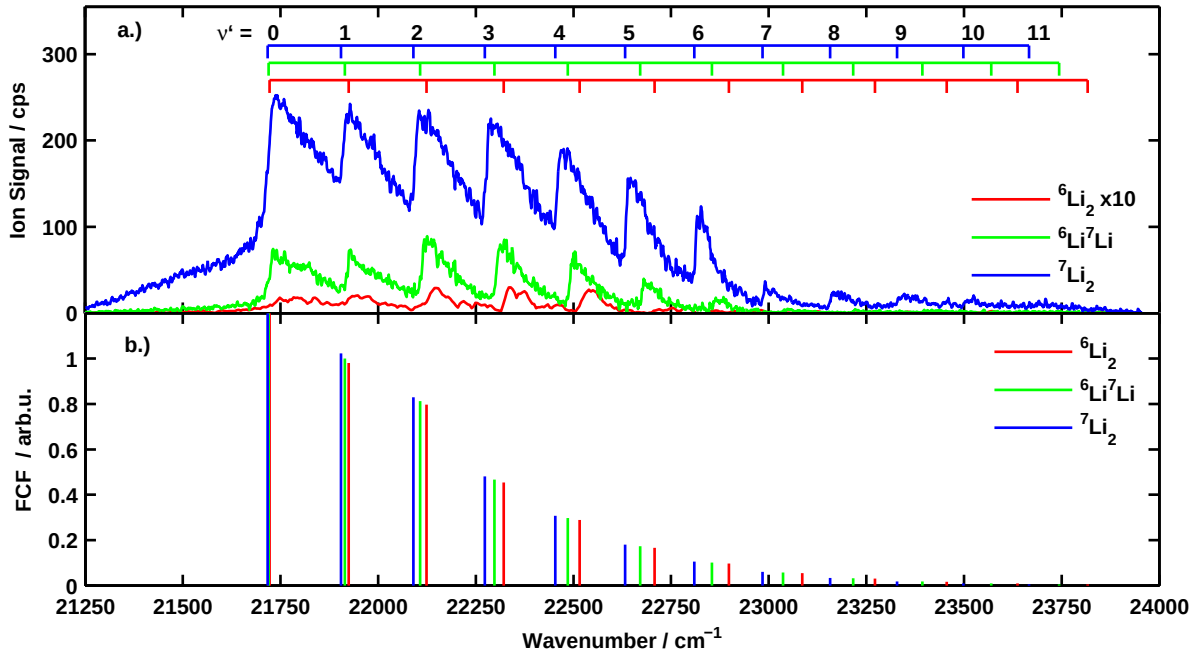

Figure 4.9: a) Li_2 $2^3\Pi_g \leftarrow 1^3\Sigma_u^+$ transition as recorded by REMPI-TOF spectroscopy. The ion yield for the three Li_2 isotopologues $^6Li_2$, $^6Li^7Li$ and $^7Li_2$ is shown, where the first was multiplied by 10 due to its low abundance. b) shows the calculated FCFs for the transition and for each isotopologue.

4.3 Rubidium-Strontium

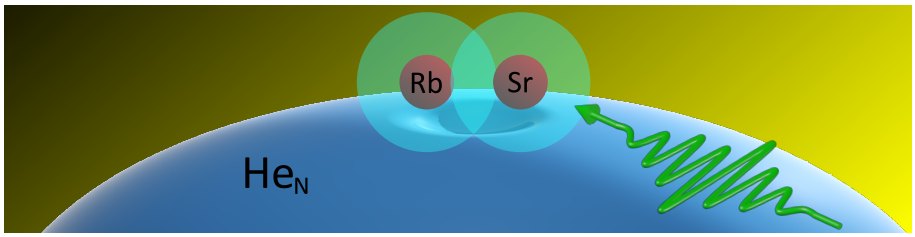

RbSr was chosen as the second Ak-Ake molecule to investigate because it is the most promising candidate for the first Ak-Ake molecular quantum degenerate gas. As mentioned in the introduction Ak-Ake molecules are interesting for ultracold molecular physics because they possess a magnetic moment in addition to the electric dipole moment, in contrast to homo- or heteronuclear Ak or Ake molecules. RbSr is the most promising candidate since both Rb [5] and Sr [150] have been condensed to a BEC, and both dimers Rb_2 [155] and Sr_2 [149] have been generated in the ultracold regime. Recently even a quantum degenerate gas mixture of Rb and Sr has been achieved [125].
Several theoretical works deal with the molecular structure of RbSr [7, 125, 169, 170], but up to the point of our research no experimental investigations were known. As will be shown in the section about the mass spectrum of RbSr, this Ak-Ake molecule holds some challenges, since both Rb and Sr possess several isotopes with a considerable abundance in a very narrow mass range.
In our investigation of the RbSr molecule on He_N we recorded a REMPI-TOF spectrum in a spectral range of $11600 - 23000\,cm^{-1}$. The transitions from the ground state ($X^2\Sigma^+$) to 6 different excited states ($2^2\Pi$, $3^2\Sigma^+$, $4^2\Sigma^+$, $3^2\Pi$, $4^2\Pi$ and $6^2\Sigma^+$) could be identified with the help of theoretical calculations performed by Johann Pototschnig. The $4^2\Sigma^+$ state showed a vibrational resolution and was further investigated with LIF spectroscopy and dispersed fluorescence (DF) spectroscopy. The vibrational resolution allowed to extract molecular parameters of the excited state and the results of the DF spectrum allowed to draw conclusions about the ground state and an intermediate state, populated during the emission from the $4^2\Sigma^+$ state.

The results of the investigations were split in several publications: A short publication [92] presents the first experimental investigation of RbSr as well as a REMPI-TOF spectrum in the spectral range of $11600 - 23000\,cm^{-1}$. It mainly deals with the dispersed fluorescence spectrum of RbSr obtained upon excitation of the vibrationally resolved $4^2\Sigma^+ \leftarrow X^2\Sigma^+$ transition. This publication has been composed by Florian Lackner, hence the paper is not contained fully here, but its contents is described in the section about dispersed fluorescence of RbSr (section 4.3.7 p79).
Secondly a more extensive article has been published, presenting a detailed analysis of the single transitions found in the REMPI-TOF experiments, with special emphasis on the vibrationally resolved transition, which was additionally investigated with LIF spectroscopy. This paper has been composed by myself and sections of it are contained fully in the following.
The theoretical results will be published in a separate article.
In general, the experiments as well as the data acquisition and processing for RbSr have been performed by Florian Lackner, Thomas Buchsteiner and myself, while the theoretical calculations where done by Johann Pototschnig.

Experimentally, the optimum pickup temperature for a maximum RbSr signal has been found to be in the range of $T_{Rb} \cong 80\,^{\circ}\mathrm{C}$ and $T_{Sr} \cong 410\,^{\circ}\mathrm{C}$. For the method of resonance enhanced multi-photon ionization time-of-flight spectroscopy a dye laser (Lambda Physik FL 3002) was used to excite the dopant molecules and a fraction of the pump laser (Radiant Dyes RD-EXC 200 XeCl laser, 26 ns pulse duration, 100 Hz) was used to ionize it. From an energy of $14700\,\mathrm{cm}^{-1}$ upwards, a two-photon ionization scheme utilizing only the dye laser was applied. The RbSr transition around $14000\,\mathrm{cm}^{-1}$ was also investigated with laser induced fluorescence spectroscopy, using a cw ring dye laser (Coherent 699) operated with Pyridine 2. The photon signal was monitored as a function of the dye laser wavenumber by a photomultiplier tube (Hamamatsu R943-02). For the recording of the DF spectrum the PMT was replaced by a grating monochromator (McPherson EU-700) with a CCD camera attached (LOT-Andor iDUS DU401ABR-DD).

The presentation of the results on RbSr are structured as follows: The sections about the mass spectrum, the REMPI-TOF spectrum and the single molecular transitions are taken from ref. [87]. Subsequently, the results gained from DF spectroscopy, published in ref. [92] are summarized. In the end the conclusion of ref. [87] has been added and extended by the contents of the conclusion of [92].
Please note that the theoretically calculated PECs of RbSr, shown in figure 4.12, have not been presented in ref. [87], but have been added in the beginning of the following section for the sake of structure.

4.3.1 Mass Spectrum

Both, Rb and Sr possess several isotopes with a high abundance in a narrow mass range, consequently some mass windows comprise of a superposition of dimer and RbSr ion yields. The dimer contribution can affect the REMPI spectra and therefore we discuss the mass spectrum at the beginning of the results section. As an example we show the sum of the mass spectra recorded while the excitation laser was scanned across the $4^2\Sigma^+ \leftarrow X^2\Sigma^+$ transition (a full mass spectrum is acquired for every laser scan-step), in Figure 4.10. This transition represents a prime example because it is superimposed by Rb and Sr dimer signals and consequently all possible masses (including monomers) can be seen and their influence on the excitation spectra can be discussed on the example of the presented mass spectrum.
The left portion in Figure 4.10 shows the monomer masses of Rb and Sr, where the contributions of Rb (green bars) and Sr (magenta bars) are denoted in the figure according to their natural abundances: ^{85}Rb-72.18%, ^{87}Rb-27.82%, ^{86}Sr-9.86%, ^{87}Sr-7.0% and ^{88}Sr-82.58% [103]. Note that atoms and molecules desorb from the helium droplet upon excitation and can thus be

detected in their corresponding mass window. The right portion of Figure 4.10 shows the distribution of the dimers and the RbSr isotopologues. Most mass peaks contain the contribution of two or more different molecules (isotopologues of Rb_2, Sr_2 and RbSr), the color coding in Figure 4.10 helps to identify these contributions. The percentages of Rb_2 are denoted by a green bar, those of Sr_2 by a magenta bar and the percentage of RbSr is denoted by a blue bar.
As can be seen, the formation of RbSr molecules on the He droplet is quite efficient. The binding energy of the RbSr ground state is in the order of $\sim$1000 cm^{-1} [54, 56, 92, 169, 170]. This energy is carried away by evaporating He atoms. Assuming 5 cm^{-1} binding energy of a He atom to the droplet [26], this results in an approximate droplet shrinking of $\sim$200 atoms upon the formation of a RbSr molecule on the droplet surface, which is negligible compared to the initial droplet size of $\hat{N}_{60,15} = 6000$.

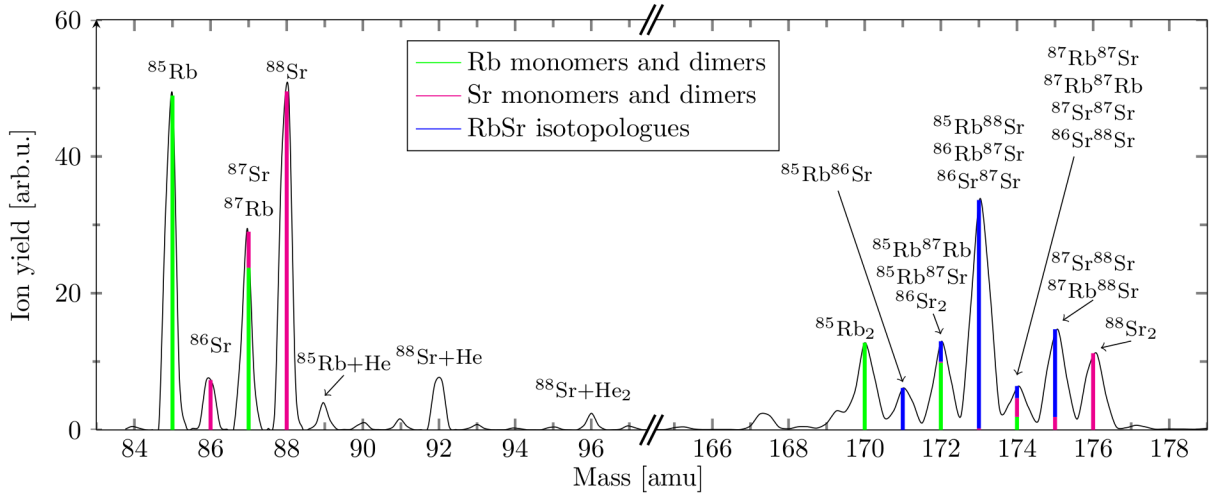

Figure 4.10: Example of a mass spectrum, showing Rb and Sr monomers (left) and dimers (right) as well as the RbSr molecule, recorded during a REMPI-TOF experiment. The black line denotes the ion yield recorded with a time of flight mass spectrometer.

As shown in the right portion of Figure 4.10, the masses of $^{85}Rb^{88}Sr$ and $^{87}Rb^{88}Sr$ coincide with the masses of Sr dimers ($^{86}Sr^{87}Sr$ and $^{87}Sr^{88}Sr$). Even though the abundance of these Sr dimer isotopologues is small, it can lead to an unwanted background in the REMPI-TOF recording, despite its advantage of providing mass resolved excitation spectra. This can be prevented to some extend by lowering the temperature of the pickup cells, thus decreasing the probability of a two-atom pickup. $^{85}Rb^{88}Sr$ has the highest abundance among the RbSr isotopologues and is only weakly influenced by a $^{86}Sr^{87}Sr$ contribution. In the example shown in Figure 4.10: While the ratio between $^{87}Rb^{88}Sr$ and the $^{87}Sr^{88}Sr$ dimer can be estimated with 9:1, the ratio of $^{85}Rb^{88}Sr$ to $^{86}Sr^{87}Sr$ is 99:1. Consequently, in order to guarantee an unambiguous identification of RbSr transitions, we only show the $^{85}Rb^{88}Sr$ ion yield in the presented spectra, if not denoted otherwise. The exclusion of the other isotopologues from the spectra and the corresponding loss in total signal are compensated by the better signal-to-dimer background ratio, since the appearance of dimers can be neglected and the pickup can be optimized for a maximum RbSr signal. Note that, in contrast to LiCa on He droplets [88], isotope shifts could not be observed in the RbSr spectra, due to the heavier constituents of the molecule.

4.3.2 Excitation Spectrum

An excitation spectrum of RbSr on He nanodroplets was recorded with REMPI-TOF spectroscopy in a spectral range of 11600 cm^{-1} - 23000 cm^{-1}. A survey spectrum of $^{85}Rb^{88}Sr$ is shown in Figure 4.11. Now we focus on a detailed analysis of the recorded transitions of RbSr on He nanodroplets. In addition to the experimental data, a stick spectrum of theoretical Franck-Condon factors (FCFs) [98] multiplied by the squared transition dipole moments (TDMs) for the denoted transitions has been calculated, which is shown in the following along with the spectra. The product of FCF*TDM^2 is hereafter referred to as 'transition probability'. Each band of FCFs is calculated for J= 0 rotational states. The transitions are starting at the vibrational ground state $X^2\Sigma^+$ ($\nu'' = 0$) of RbSr, since the molecules are efficiently cooled to their vibronic ground state due to the cold He environment (0.37 K). Please note that the transition probabilities have been scaled to fit the experimental data, but their relative heights with respect to each other still reflect the FCF*TDM^2 distribution (all bands have been scaled by the same factor). The corresponding potential energy curves have been presented in ref. [92], details of the theoretical methods and results will be presented elsewhere. Experimentally, the $4^2\Sigma^+ \leftarrow X^2\Sigma^+$ transition is vibrationally resolved and each band shows a characteristic lambda-shaped peak form [67,68]. All other states denoted in the spectrum could not be vibrationally resolved and appear as broadened featureless and partly overlapped structures. The assignment of the transitions is based on a comparison of experimental and theoretical spectra, as will be shown in detail in the following.

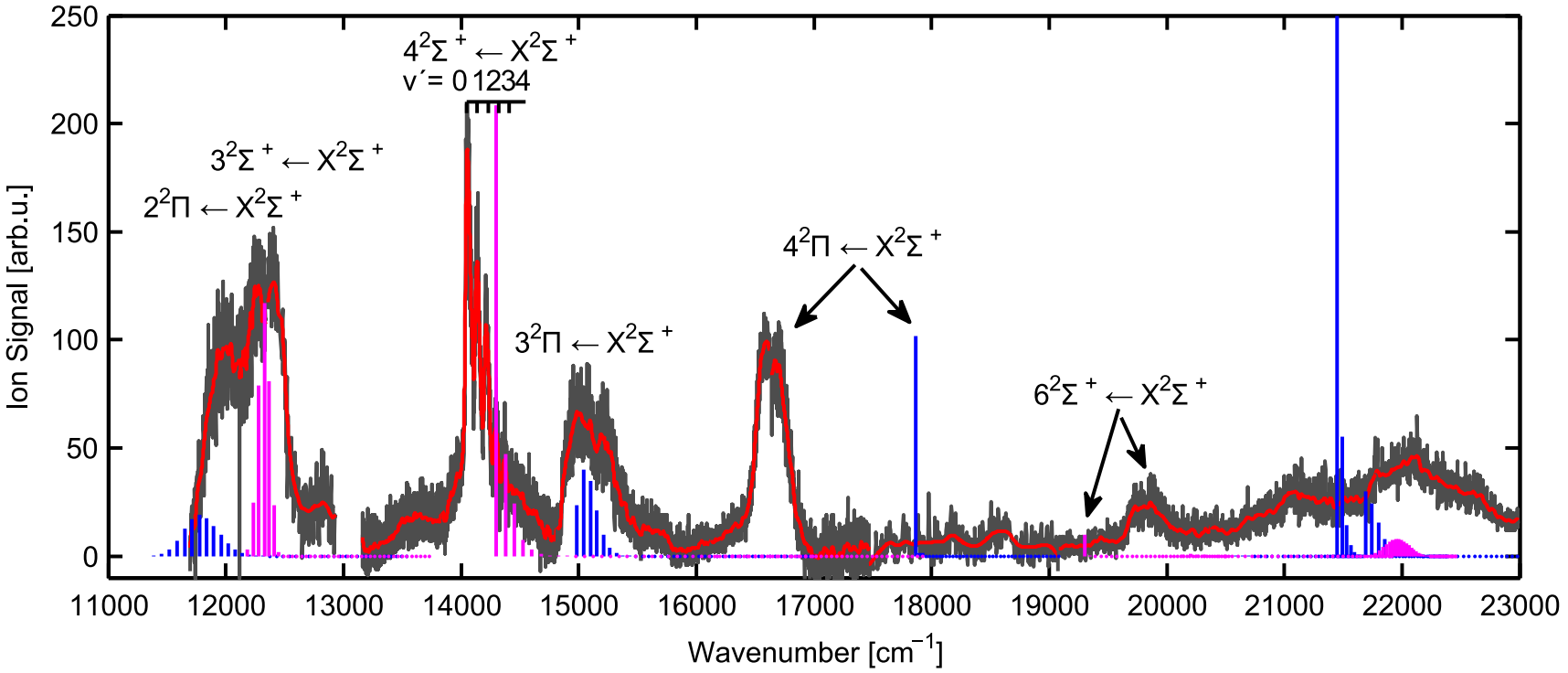

Figure 4.11: Excitation spectrum of $^{85}Rb^{88}Sr$ in the range of 11600 cm^{-1} - 23000 cm^{-1}. The signal was recorded by exciting the RbSr molecule on the He droplet by a tunable dye laser and ionizing it by a fraction of the XeCl pump laser (up to 14700 cm^{-1}) or a second photon of the dye laser (above 14700 cm^{-1}). The ion yield was recorded by a time of flight mass spectrometer. The data have been offset corrected, the gray lines show the original data points, the red and blue curves represent the data smoothed by convolution with a Gaussian. The colored bars denote the calculated transition probabilities (FCF*TDM^2) for each transition, blue indicates transitions to a Π state, magenta to a Σ state.

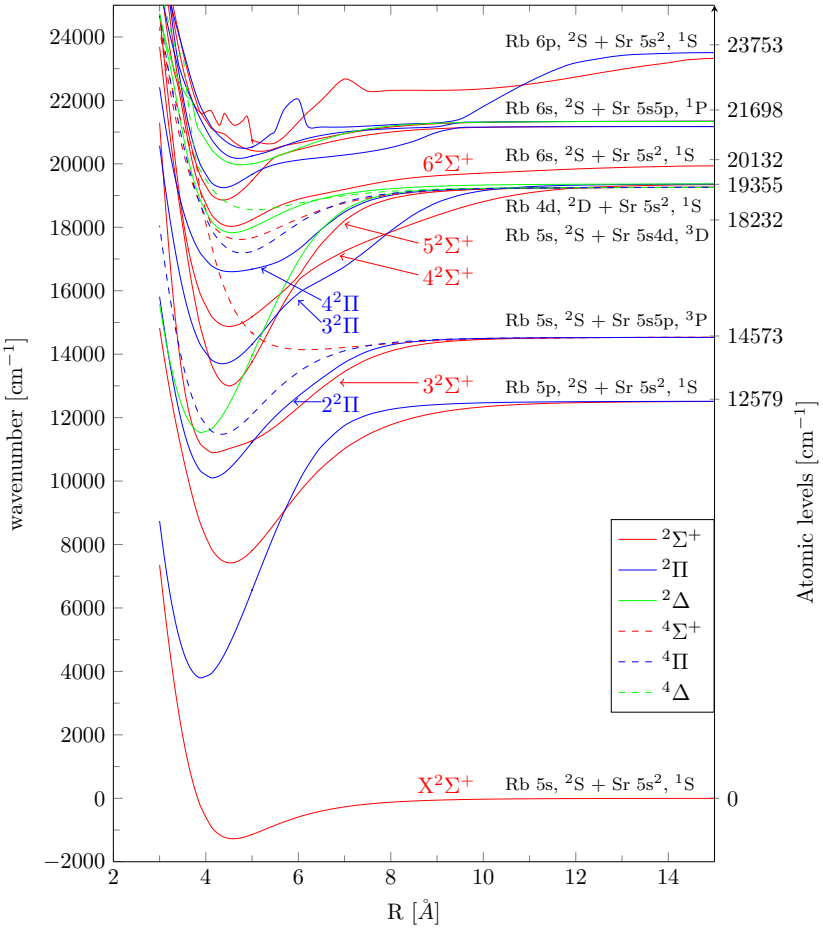

Figure 4.12: Potential energy curves for RbSr as calculated by Johann Pototschnig. The asymptotic atomic levels of the corresponding molecular states have been denoted on the left. The molecular transitions found in the REMPI-TOF recordings are indicated in the figure.

4.3.3 $2^2\Pi \leftarrow X^2\Sigma^+$ and $3^2\Sigma^+ \leftarrow X^2\Sigma^+$ Transition

Figure 4.13 shows a detailed view of the lowest energy transitions which could be observed with our laser systems. Both correlate to the Rb 5s, ^{2}S + Sr 5s5p, ^{3}P atomic asymptote. The two different data sets in the figure denote the ion yield upon excitation with a dye laser and ionization with a fraction of XeCl pump laser radiation (two photon ionization - R2PI) and the ion yield upon excitation and ionization with the pulsed dye laser alone (three photon ionization - R3PI). The structure in Figure 4.13 shows a very broad double peak feature in the R2PI (blue) as well as in the R3PI (red) signal. On the low energy side the structure is cut off, because the end of the tuning range of the dye laser optics is reached at 11600 cm^{-1}, accompanied by a rapid decrease of the Rh800 pulse energy.
On the high energy side the R2PI signal shows a constant background, which is caused by the XeCl laser. Also shown in Figure 4.13, in form of colored bars, are the calculated transition probabilities (FCF*TDM^2), these suggest two overlapping transitions in this wavelength range, which coincide well with the experimental data. Based on these calculations we assign the transition at lower energy to $2^2\Pi \leftarrow X^2\Sigma^+$ and the higher energy transition to $3^2\Sigma^+ \leftarrow X^2\Sigma^+$.
Note that the MRCI potential energy curves, which have been used for the calculation of the transition probabilities, do not consider relativistic effects. It has been shown that for a proper

description of dispersed fluorescence spectra of transitions originating from molecular states which correspond to the Rb 5s, ^{2}S + Sr 5s5p, ^{3}P asymptotes, spin-orbit coupling has to be taken into account [92]. However, for the excitation spectrum the broadened and overlapping transitions can be well explained in a simple non-relativistic picture. The corresponding relativistic Hund's case (c) potentials with a considerable transition dipole moment are of $^2\Sigma^+$ and $^2\Pi$ character at short range, the main effect of spin-orbit coupling for these states will result in a slight shift (two $\Omega = 1/2$ states and one $\Omega = 3/2$ state are relevant) [92]. However, for the sake of consistency we assign the observed double peak structure on basis of Hund's case (a) potentials without SO-coupling which is, in light of the precedent discussion, valid within our experimental resolution. A comparison of the R3PI and the R2PI signal shows that the latter is in better accordance with the calculations, since the transition dipole moment for $3^2\Sigma^+ \leftarrow X^2\Sigma^+$ is higher than for the $2^2\Pi \leftarrow X^2\Sigma^+$ transition. Note that both signals have been recorded with approximately the same laser pulse energy. This behavior is reasonable, because the R3PI signal involves an intermediate state above the $2^2\Pi$ and $3^2\Sigma^+$ states. The transition probability to this intermediate state as well as its lifetime will affect the signal. In the R2PI signal these additional effects do not occur, since the RbSr molecule is directly ionized from the $2^2\Pi$ or $3^2\Sigma^+$ excited state.

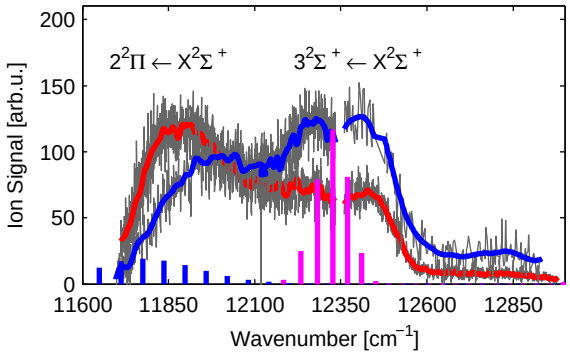

Figure 4.13: Detailed view of the $3^2\Sigma^+ \leftarrow X^2\Sigma^+$ and $2^2\Pi \leftarrow X^2\Sigma^+$ transitions. Blue denotes the R2PI signal recorded by two-photon ionization with the dye and the XeCl laser, while the red signal was obtained by a R3PI with the dye laser alone. The gray lines show the original data points, the red and blue curves represent the data smoothed by convolution with a Gaussian. The colored bars denote the calculated transition probabilities (FCF*TDM^2), blue indicates transitions to the $2^2\Pi$ state, magenta to the $3^2\Sigma^+$ state. The gap in the recording is due to a small wavelength range not covered by the two dyes Rh800 and Sty9.

4.3.4 $4^2\Sigma^+ \leftarrow X^2\Sigma^+$ Transition

Figure 4.14 shows several aspects of the RbSr $4^2\Sigma^+ \leftarrow X^2\Sigma^+$ transition in detail. The vibrational resolution of this transition allows a more refined study. The calculated transition probabilities, which facilitate the assignment of the transition, are shown in panel a) and b) of Figure 4.14. According to our calculations the $4^2\Sigma^+$ PEC is associated with the Rb 5s, ^{2}S + Sr 5s4d, ^{3}D asymptote. Note that the $4^2\Sigma^+$ PEC experiences an avoided crossing with the $5^2\Sigma^+$ PEC.
As shown in panel a) of Figure 4.14, vibronic transitions from $\nu' = 0 - 4 \leftarrow \nu'' = 0$ can be identified in the REMPI-TOF signal. Considering the droplet temperature of 0.37 K, the RbSr molecule is cooled to its vibrational ground state $\nu'' = 0$ upon formation on the droplet and all excitations start from the vibronic ground state. The asymmetric broadening of the vibrational bands is caused by an interaction of the molecule with the droplet. As explained in refs. [67,68] for alkali triplet molecules on He droplets, a strong coupling of the molecular vibrations to the

surface of the He droplet causes the merging of the zero phonon line with the phonon wing, resulting in a lambda-shaped peak form. Consequently the onset of the rising edges of the broadened lines coincide with the band origins of the free molecule within $\sim$10 cm^{-1}, as has been shown e.g., for Li_2 [96] and LiCa [88]. Similar to RbSr, a strong coupling of the LiCa molecule to the He droplet surface has been reported. This suggests that a strong coupling of the Ak-Ake molecules with the He droplet is a common feature. In comparison to Ak dimers on He droplets, where zero phonon lines have been observed for singlet transitions [65], the strong coupling of Ak-Ake molecules seems reasonable, because Ake atoms interact more strongly with the helium droplet [153].
Additional to REMPI-TOF spectroscopy the $4^2\Sigma^+ \leftarrow X^2\Sigma^+$ transition was investigated with LIF spectroscopy, the resulting spectrum is shown in panel b) of Figure 4.14. Again, the vibrational levels $\nu' = 0 - 4$ can be identified. Compared to the REMPI-TOF signal the $\nu' = 0 \leftarrow \nu'' = 0$ line is much higher with respect to the other vibronic transitions and corresponds better to the relative heights of the calculated transition probabilities shown as vertical bars in the Figure. The reason for this is a saturation of the transition in the REMPI-TOF signal due to the relatively high pulse energies necessary to obtain a reasonable count-rate. The LIF signal also shows an underlying background around 14100 cm^{-1}, which originates from the Sr_2 ($1^1\Sigma_u^+ \leftarrow X^1\Sigma_g^+$) [148] transition and probably also a very weak contribution of a Rb_3 transition ($2^4E' \leftarrow 1^4A_2'$ and $1^4A_1'' \leftarrow 1^4A_2'$) [120, 121] in this wavelength range. The background was minimized by lowering the pickup temperatures, thus decreasing the probability for dimer and especially trimer pickup, but was not suppressed completely in this experiment.
Panel c) of Figure 4.14 shows the REMPI-TOF signal for 173 amu (red), ^{85}Rb (blue) and ^{88}Sr (black) of one recording and the ^{86}Sr + ^{87}Sr dimer signal (cyan) of a different experiment, where the He droplets were solely doped with Sr and the pickup was optimized for Sr_2. As can be seen, a Sr dimer transition lies in the range of the RbSr transition, hence the ^{86}Sr^{87}Sr isotopologue contributes to the ^{85}Rb^{88}Sr (173 amu) signal and causes a small background in the range of 14100 cm^{-1}. The Sr dimer signal was subtracted from the combined signal (red), resulting in the signal shown in panel a). This signal was then fitted in order to extract molecular parameters of the $4^2\Sigma^+$ state. As a fitting function a sum of asymmetric 2σ-functions was used [11, 88, 96]:

$$L(\bar{\nu}) = I(1 + e^{(\bar{\nu}-\bar{\nu_0}+w_1/2)/w_2)})^{-1}[1 - (1 + e^{(\bar{\nu}-\bar{\nu_0}-w_1/2)/w_3))^{-1}}] \tag{4.3}$$

The onset of each rising edge is determined by finding the maximum of the second derivative in the corresponding range, the band origins are denoted in Figure 4.14 as vertical black lines and the values are given in Table 4.3. The molecular parameters T_e, ω_e and $x_e\omega_e$ for the $4^2\Sigma^+$ state are obtained by a least-squares fit to the function given in eq. 2 [64]. Results are given in Table 4.3, including the results for the REMPI data reported in ref. [92].

$$T(\nu') = T + \omega_e\left(\nu' + \frac{1}{2}\right) - x_e\omega_e\left(\nu' + \frac{1}{2}\right)^2 \tag{4.4}$$

In equation 2, $T(\nu')$ labels the energy between the zero point energy of the ground state and the vibrational levels of the excited state $4^2\Sigma^+(\nu') \leftarrow X^2\Sigma^+(\nu'' = 0)$ and T denotes the energy from $X^2\Sigma^+(\nu'' = 0)$ to the minimum of the $4^2\Sigma^+$ PEC. In the following we estimate T_e (the distance between the PEC minima) for the sake of a better comparability with theoretical results, the value is listed in Table 1. As an approximation for the zero point energy of the ground state, we take the value of $(\nu'' = 1 - \nu'' = 0)/2$ and add it to T which gives T_e. The results of dispersed fluorescence experiments are included in table 4.3 and show that the values obtained for RbSr on the droplet are well within $\sim$ 10 cm^{-1} of the free RbSr molecule values. While the results

obtained with different experimental approaches are in excellent agreement with each other, the absolute energy of the transition is overestimated by the calculation by $\sim$280 cm^{-1}. Considering the complex electronic structure of the RbSr molecule and the proximity of atomic asymptotes this still provides a good result. The calculated harmonic constant is slightly underestimated.

Table 4.3: Vibrational bands and molecular parameters of ^{85}Rb^{88}Sr for the $4^2\Sigma^+ \leftarrow X^2\Sigma^+$ transition. One standard deviation uncertainties of the fit are given in parenthesis.

Band $\nu' - \nu''$	Energy (cm^{-1}) REMPI-TOF, this work	Energy (cm^{-1}) LIF, this work	Energy (cm^{-1}) theory, this work	Energy (cm^{-1}) DF [92]
0 - 0	14028(1)	14032(1)	14300.6	14014(5)
1 - 0	14114(3)	14119(4)	14376.7	
2 - 0	14192(1)	14201(2)	14452.7	
3 - 0	14272(1)	14285(3)	14528.4	
4 - 0	14348(21)	14358(4)	14603.9	
T_e	14006(4)	14006(4)	14282.2	
ω_e	86(3)	92(4)	76.4	
$x_e\omega_e$	1.2(0.7)	1.9(0.7)	0.12	

Panel c) of figure 4.14 shows that the mass signals of the ^{85}Rb (blue) and ^{88}Sr (black) atoms, roughly follow the RbSr signal. A similar behavior has been reported for LiCa, where predissociating states enhance the fragmentation process. In general, dynamic processes of atoms or molecules on helium droplets induced by laser excitation are governed by non-radiative relaxation mechanisms, enhanced by the helium environment. For RbSr on He droplets a substantial relaxation upon excitation of the $4^2\Sigma^+$ state into lower electronic states has been reported. [92] This considerably attenuates the direct transition into the ground state $4^2\Sigma^+ \rightarrow X^2\Sigma^+$ and the majority of the fluorescence has been found to originate from lower states. This has been attributed to the $1^2\Delta$ state, which crosses the $4^2\Sigma^+$ state at its potential minimum and provides a relaxation channel to lower states. The observation of fragments which correlate to the $4^2\Sigma^+ \leftarrow X^2\Sigma^+$ transition in figure 4.14 c) suggests that not only bound states are populated during the relaxation, but also repulsive states that lead to a fragmentation of the molecule. The complex electronic structure of RbSr makes it difficult to give a complete description of the observed fragmentation of molecules, but weakly bound states which are of quartet character in the non-relativistic picture have to be considered in this process. Note that the signature of excited atomic Rb fragments has also been observed in the dispersed fluorescence spectra [92] as D-line emission.
Additionally, this fragmentation process may be superimposed by fragmentation caused by a dissociation of the $RbSr^+$ molecule by a third photon of one of the two laser in the REMPI-TOF experiments.

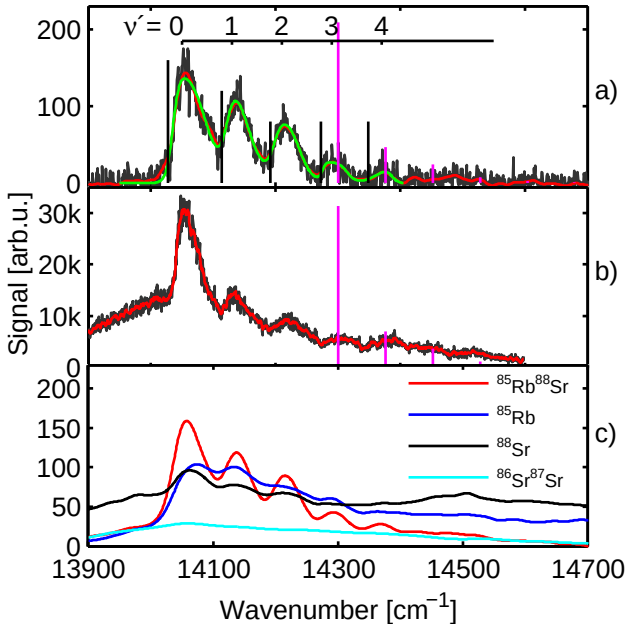

Figure 4.14: Closeup of the $4^2\Sigma^+ \leftarrow X^2\Sigma^+$ transition. a) the gray line shows the original data points recorded with REMPI-TOF spectroscopy. The red line the smoothed data, green denotes the fitted signal (according to equation 1) and the black vertical lines mark the onset of the rising edges, corresponding to free molecule transitions b) shows the $4^2\Sigma^+ \leftarrow X^2\Sigma^+$ transition recorded with LIF spectroscopy and c) shows the smoothed ion yield for atoms and molecules during the REMPI-TOF measurement. The cyan line corresponds to Sr_2 recorded with only Sr doped droplets. All signal curves have been smoothed by convolution with a Gaussian. The magenta bars in panel a) and b) denote the calculated transition probabilities (FCF*TDM^2).

4.3.5 $3^2\Pi \leftarrow X^2\Sigma^+$ Transition

Figure 4.15 shows the $3^2\Pi \leftarrow X^2\Sigma^+$ transition for the RbSr isotopologues $^{85}Rb^{86}Sr$, $^{85}Rb^{88}Sr$ and $^{87}Rb^{88}Sr$. The transition shows a broad featureless structure with a steep rising edge on the low energy side. Based on the calculations, as shown in form of transition probabilities (FCF*TDM^2) in the figure, we assign this structure to the $3^2\Pi \leftarrow X^2\Sigma^+$ transition. The signal is well reproduced by the theoretical results, in terms of spectral position as well as in the relative intensity distribution. The $3^2\Pi$ state correlates to the same atomic asymptote as the $4^2\Sigma^+$ state (Rb 5s, ^{2}S + Sr 5s5p, ^{3}D) and experiences an avoided crossing with the $4^2\Pi$ state.
Please note that for energies above 14700 cm^{-1} only the dye laser has been used to excite and ionize the RbSr molecule. In the energy range of this transition an ionization of RbSr with two photons of the dye laser becomes possible. Considering a depth of the RbSr ground state of ~1000 cm^{-1} and a depth of the $RbSr^+$ ground state [14] of 4285 cm^{-1} a two photon ionization for bare RbSr is possible above an energy of ~15200 cm^{-1}. In addition, it is known that the helium environment lowers the vertical ionization threshold (IT). Experiments have shown that the IT of species on and in He droplets is lowered as a consequence of polarization effects, ranging from several tens of wavenumbers for surface-located alkali atoms [160] up to ~1000 cm^{-1} for molecules inside the droplet [108]. Although this estimation is based on theoretical results with a relatively high uncertainty it is in agreement with the experimental spectra, which show no evidence of an ionization threshold. The slight increase of the signal at ~15160 cm^{-1} may either be related to the ionization potential of free, desorbed RbSr molecules or RbSr on He droplets, but the weak structure forbids an unambiguous assignment.
As mentioned in the mass spectrum section above, the REMPI-TOF signal of 175 amu consists of a $^{87}Rb^{88}Sr$ and a $^{87}Sr^{88}Sr$ contribution. The ratio of the two isotopologues can in the case of the

$3^2\Pi \leftarrow X^2\Sigma^+$ transition be estimated as 6:4 due to the strong Sr_2 transition in this wavelength range, despite optimization for RbSr, see Figure 4.15. The signals of the three isotopologues of RbSr should show the same structure, where the relative signal intensity reflects the natural abundance. While 171 amu ($^{85}Rb^{86}Sr$ - black) and 173 amu ($^{85}Rb^{86}Sr$ - red) have the same structure, 175 amu ($^{87}Rb^{88}Sr$ - green) has a different trend on the low energy side. It follows the trend of the rather strong Sr dimer transition around 14900 cm^{-1}. Consequently, this confirms the decision to rely on the $^{85}Rb^{88}Sr$ signal, since even in the case of a strong Sr dimer transition the influence of the $^{86}Sr^{87}Sr$ signals is negligible (97:3).
Note that the rising edge of the RbSr ion signal is reliable, but the rising edge of the Sr_2 (R3PI) ion signal is not. Because of the rapid decrease of laser energy at this end of the dye tuning range, the extension of the Sr_2 spectrum below 14700 cm^{-1} is suppressed. Different experimental parameters were used for laser dyes below and above 14700 cm^{-1}: For lower energies a R2PI scheme via ionization with a XeCl laser was used and the laser pulse energies were optimized for best RbSr signal, in this case small pulse energies were sufficient. For the excitation shown in Figure 4.15, R3PI (in the case of Sr_2) with only the dye laser was applied and a higher laser pulse energy was necessary.

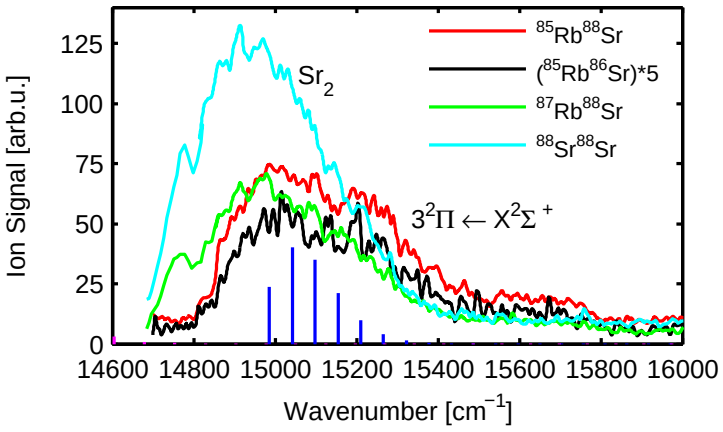

Figure 4.15: The $3^2\Pi \leftarrow X^2\Sigma^+$ transition in detail. The colored lines show different isotopologues of RbSr (black-171 amu, red-173 amu and green-175 amu) and the $^{88}Sr^{88}Sr$ dimer signal in cyan, for an easier comparison the signal for the $^{85}Rb^{86}Sr$ (black) isotopologue has been multiplied by a factor of 5. The signal was obtained by an ionization with the dye laser alone. The signal curves have been smoothed by convolution with a Gaussian. The blue bars denote the calculated transition probabilities (FCF*TDM^2).

4.3.6 Higher Excited States

Figure 4.16 shows the REMPI-TOF spectrum of RbSr in the wavelength range of 16000 cm^{-1} - 23000 cm^{-1}. Theoretical transition probabilities are plotted as vertical bars, blue for transitions into a $^2\Pi$ state, magenta for transitions into a $^2\Sigma^+$ state. In this energy range the assignment of peaks to molecular transitions becomes more difficult due to the large number of molecular potential energy curves.
The calculations enable an assignment of the two broadened and featureless structures at 16600 cm^{-1} and 19700 cm^{-1} to the transitions $4^2\Pi \leftarrow X^2\Sigma^+$ and $6^2\Sigma^+ \leftarrow X^2\Sigma^+$, respectively. Both states show roughly the same structure, where the steep rising edge is more pronounced in the $6^2\Sigma^+ \leftarrow X^2\Sigma^+$ transition. Both features are narrow and vibrational states are not resolved. A possible explanation for this is provided by the theoretical calculations. For both electronic

transitions only the $\nu' = 0 \leftarrow \nu'' = 0$ vibronic transition has a significant transition probability, due to the similarity of the excited and ground state PEC.
Beyond 16000 cm^{-1}, theoretical calculations become increasingly challenging because of the proximity of atomic Rb and Sr energy levels and numerous avoided crossings related to the increasing density of molecular states. In this region, results obtained from different theoretical methods can differ in the order of 1000 cm^{-1}. [92, 170] Consequently, the differences between experiment and calculation increase.
The $4^2\Pi$ state dissociates to the Rb 4d, ^2D + Sr $5s^2$, ^1S asymptote and is hence affected by the avoided crossing with the $3^2\Pi$ state described above. The calculated values for the $4^2\Pi$ potential energy curve deviate for large internuclear separation by $\sim$1000 cm^{-1} from atomic values [135]. A comparison with the experimental data suggests that this deviation is transferred to the potential energy curve for short ranges, because the experimental value deviates from the theoretical value by $\sim$1250 cm^{-1}.
The $5^2\Sigma^+ \leftarrow X^2\Sigma^+$ transition, which is expected to lie also in the range of 16000-17000 cm^{-1}, has a transition dipole moment (TDM) which is four orders of magnitude lower than the TDM for the $4^2\Sigma^+ \leftarrow X^2\Sigma^+$ transition. Hence we excluded an association of the observed transitions with the $5^2\Sigma^+$ state and explain the absence of this state in the excitation spectrum by this fact.
The transition at $\sim$19700 cm^{-1} is assigned to the $6^2\Sigma^+ \leftarrow X^2\Sigma^+$ transition, the theoretical result lies $\sim$400 cm^{-1} below this value. The corresponding asymptote of the $6^2\Sigma^+$ state (Rb 6s, ^2S + Sr $5p^2$, ^3D) is underestimated by $\sim$200 cm^{-1} in the theoretical calculations. Assuming that this deviation is transferred to the PEC at short ranges, the displacement between the theoretical and experimental values corresponding to the $6^2\Sigma^+ \leftarrow X^2\Sigma^+$ transition is significantly reduced.
Above an energy of 20500 cm^{-1} the density of excited states as well as the number of avoided crossings increase and additionally the deviations for the asymptotic values rise. The experimental data show a broad structure extending from 20500 cm^{-1} - 23000 cm^{-1}. An unambiguous assignment is not possible, but our calculations suggest that the observed structure consists of several overlapping transitions. Contributions to the signal most probably arise from three transitions into the $6^2\Pi$, $7^2\Pi$ and $8^2\Sigma^+$ states, where the calculated transition probability for the $6^2\Pi \leftarrow X^2\Sigma^+$ is the highest, as shown in Figure 4.16.

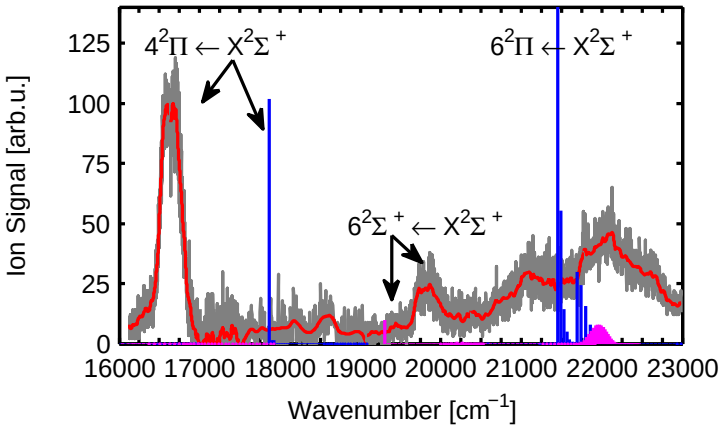

Figure 4.16: REMPI-TOF signal of the highest RbSr transitions recorded. The gray lines show the original data points, the red curve the smoothed signal (by convolution with a Gaussian). Calculated transition probabilities (FCF*TDM^2) are shown as vertical bars, blue bars denote a transition into a $^2\Pi$ state, magenta bars into a $^2\Sigma^+$ state. The arrows assign the correlated experimental and theoretical transitions. Around 22000 cm^{-1} the $8^2\Sigma \leftarrow X^2\Sigma^+$ is expected but not unambiguously assigned (see text).

4.3.7 RbSr - Dispersed Fluorescence

In this section the results obtained from an analysis of the dispersed emission of the $4^2\Sigma^+$ state is presented. These results have been published in [92] and the following text will give an account of the part of the publication concerned with the DF spectrum.

The advantage of data retrieved from DF spectra is that the signal results from free RbSr molecules, desorbed upon excitation. A relaxation of the excited molecule into vibrationally excited levels of the $X^2\Sigma^+$ ground state provides information about ground state properties.
A thorough investigation of the emission spectrum from the excitation energy of the $4^2\Sigma^+(\nu' = 0) \leftarrow X^2\Sigma^+(\nu'' = 0)$ transition (14060 cm^{-1}) down to the detection limit of the CCD camera (11500 cm^{-1}), revealed two different fluorescence channels. Fig. 4.17 shows the wavelength range around the excitation. The two peaks at the low energy side of the excitation have been assigned to the emission lines $4^2\Sigma^+(\nu' = 0) \rightarrow X^2\Sigma^+(\nu'' = 0, 1)$. A fit of the two peaks reveals a FWHM of 6 cm^{-1} and a spacing of (42±5) cm^{-1}. Within our experimental resolution this can be taken as an approximation for the harmonic constant ω_e of the ground state. The theoretical value from our calculations (42.2 cm^{-1}) is in perfect agreement with the experiment and in excellent agreement with values obtained by Żuchowski et al. [169] (ω_e =39 cm^{-1} and ω_e =38.1 cm^{-1}). This testifies the quality of the calculations for short ranges of the ground state.
A second strong fluorescence signal was found in the range of 12200-12500 cm^{-1}, as shown in figure 4.18. A theoretical explanation of this structure has proven to be rather challenging. It was finally achieved by taking spin-orbit splitting into account and calculating the PECs corresponding to the Rb 5s, ^{2}S+Sr 5s5p, ^{3}P atomic states with a relativistic approach, which leads to Hund's case (c) PECs. An effect of the spin-orbit splitting is to be expected for these states, since the SO constant for the Sr 5s5p, ^{3}P asymptote is rather large ($A_{Sr(^3P)}$=193.7 cm^{-1}). Taking the three lowest states (one Ω =3/2 and two Ω =1/2) into account allowed a simulation of the emission spectrum which represents the experimental data very well. The simulated spectrum is also shown in figure 4.18 and the spin-orbit split PECs are shown in fig. 4.19.

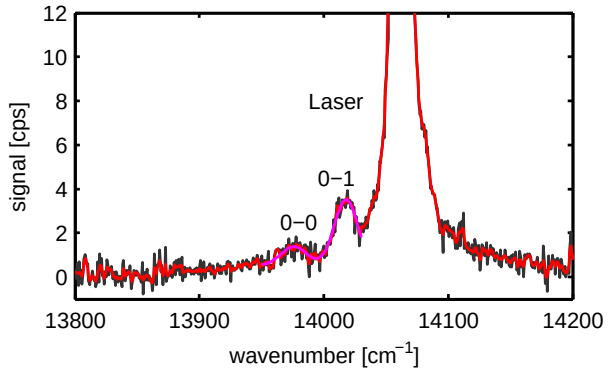

Figure 4.17: Dispersed fluorescence spectrum of RbSr upon excitation of the $4^2\Sigma^+$ state in the region of the excitation wavelength. The two peaks at the low energy side are assigned to emission lines into the first vibrational levels ($\nu'' = 0, 1$) of the ground state.

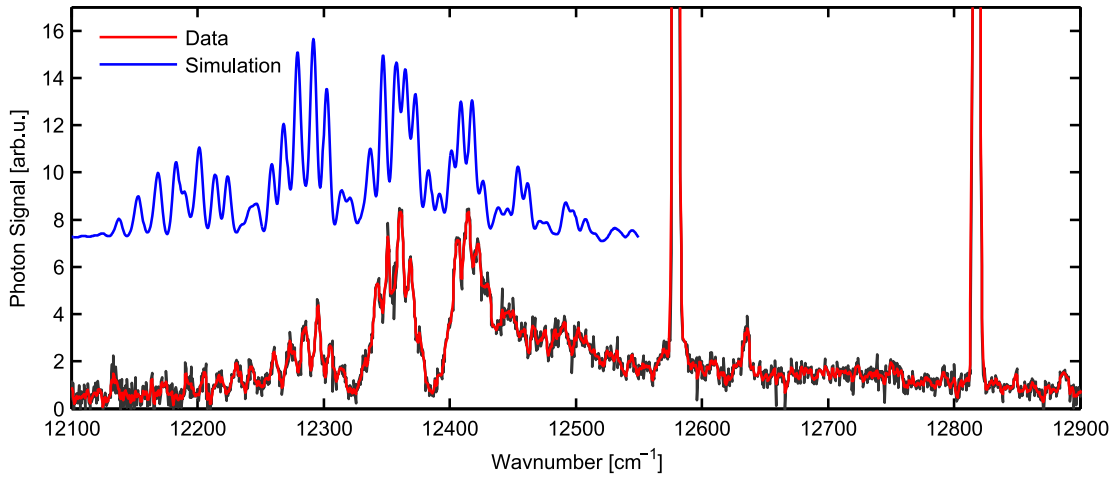

Figure 4.18: Dispersed fluorescence spectrum of RbSr upon excitation of the $4^2\Sigma^+$ state in the range of 12200-12500 cm^{-1}. The structure has been assigned to emission lines from vibrationally excited states of spin-orbit split molecular states (corresponding to the Rb 5s, ^{2}S + Sr 5s5p, ^{3}P asymptote) to the molecular ground state. A proper explanation of the structure was only possible by taking spin-orbit coupling into account for the upper states by a relativistic approach. The two large peaks at 12580 cm^{-1} and 12520 cm^{-1} correspond to the Rb D1 and D2 lines, which occur due to fragmentation of RbSr and Rb dimers.

In order to calculate the transitions the LEVEL8 program [98] was used and the linewidth was approximated by a Gaussian with a FWHM of 6 cm^{-1} (corresponding approximately to the resolution of the monochromator engaged). The largest contribution is provided by the lowest $\Omega = 1/2$ state originating from the Sr $^3P_1$ atomic state. This state has the highest TDM according to our calculations. At short range it is of $3^2\Pi$ character. The contributions of the two energetically lower states $\Omega = 1/2$ and $\Omega = 3/2$ only account for a minor effect. In order to achieve an optimal reproduction of the experimental signal, the maximum of the populated states has to be assumed at 12820 cm^{-1}, corresponding to the $\nu' \sim 14$ level of the $\Omega = 1/2$ ($^3P_1$) state. Then the spacing of the large structures (∼60 cm^{-1}) as well as those of the fine structures (∼10 cm^{-1}) is represented well, as shown in figure 4.18. In order to match the measured band position, a shift by 90 cm^{-1} to lower energies has been applied. It is interesting to note that most of the fluorescence signal originates from these intermediate states, which are the most

interesting for ultracold molecule experiments [125, 169].

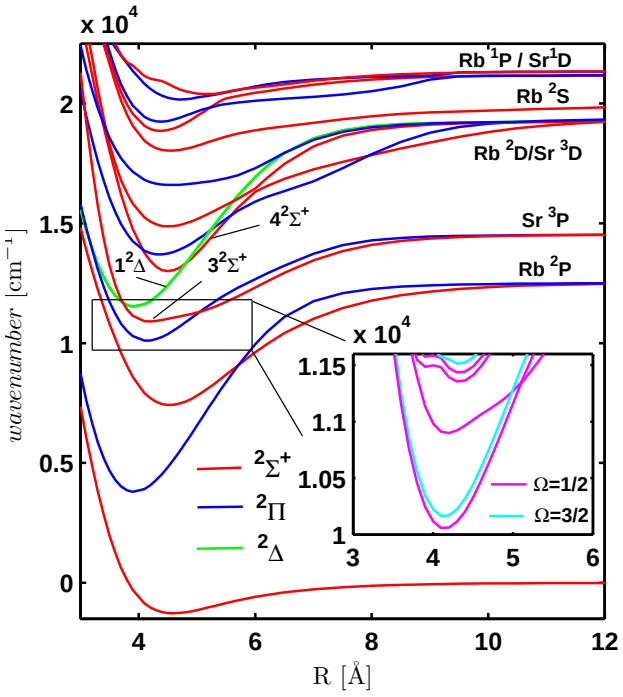

Figure 4.19: Calculated PECs for RbSr, including the relativistic PECs relevant for the interpretation of the DF spectrum.

The calculations show that it is important to consider possible effects of the $^2\Delta$ state originating from the Rb 4d, ^{2}D+Sr 5s^2, ^{1}S atomic states. In the non-relativistic picture it crosses the $3^2\Sigma^+$ state exactly in the region of the assumed population maximum, which also falls together with the minimum of the $^2\Delta$ state. The same state crosses the originally excited $4^2\Sigma^+$ close to its potential minimum, thus providing a possible relaxation channel for the excited RbSr molecules. This relaxation process might be enhanced by the He droplet, assuming that the RbSr molecule is bound to the droplet for a sufficient amount of time. However, the sharp emission lines indicate a free molecule relaxation, so the actual emission originates from free molecules. A relaxation into the energetically lower $2^2\Sigma^+$ and $1^2\Pi$ states cannot be excluded, an emission from these states is in the infrared region and beyond our detection capabilities.

4.3.8 Conclusion

In summary, we have presented a thorough experimental study of the RbSr molecule on helium nanodroplets. The utilization of REMPI-TOF spectroscopy enabled the recording of an excitation spectrum in a large spectral range from 11600 to 23000 cm^{-1}. Based on high-level ab-initio calculations [92], six transitions originating from the $X^2\Sigma^+$ ($\nu'' = 0$) vibronic ground state into excited states could be identified. The corresponding states were assigned as $2^2\Pi$, $3^2\Sigma^+$, $4^2\Sigma^+$, $3^2\Pi$, $4^2\Pi$ and $6^2\Sigma^+$ states. The interaction of the RbSr molecule with the helium droplet manifests itself in form of broadened and overlapping vibrational lines. On the basis of the observed peak shapes we can conclude that the coupling of the vibrational motion of the RbSr molecule with the liquid helium environment is strong. This appears to be a general trend for Ak-Ake

molecules on helium nanodroplets [88]. The vibrationally resolved $4^2\Sigma^+$ state was investigated in more detail with LIF and REMPI-TOF spectroscopy. The fact that vibrational levels could be resolved for the $4^2\Sigma^+$ state, enabled the determination of molecular parameters. A comparison with recent experiments [92] where $4^2\Sigma^+ \rightarrow X^2\Sigma^+$ florescence of bare RbSr molecules (formed on helium droplets) could be observed, revealed that these extracted parameters agree within a few wavenumbers with the free molecule parameters. This indicates that, despite the relatively large droplet induced broadening, the influence of the droplet on the absolute energies of the transitions is very small. In addition, we present mass spectrometric studies of the formed RbSr on helium droplets, which is very important for a correct interpretation of the recorded spectra, because of the proximity of the various isotopologues of Rb and Sr dimers and RbSr. Furthermore, we found that the complex relaxation dynamics upon laser excitation leads to a substantial fragmentation of molecules.
An analysis of the dispersed fluorescence spectrum upon excitation of the $4^2\Sigma^+$, provided access to free RbSr molecules, which desorb from the droplet upon excitation. The data retrieved from the DF spectrum gives information about the ground state. The main part of the fluorescence has been found to originate from states corresponding to the Rb 5s, ^{2}S+Sr 5s5p, ^{3}P states. The structure could be simulated by taking the spin-orbit splitting of the molecular potentials into account, in form of a relativistic calculation.
Understanding the effect of helium droplets on the spectra of dopant molecules is the key for the establishment of the helium nanodroplet isolation (HENDI) approach as a method for the characterization of novel and tailored molecules, which are difficult to form by conventional methods. The great advantage of this method is the exceptional doping possibility [26], which allows to dope the droplets with virtually any gaseous, liquid, solid as well as highly reactive atomic and molecular building blocks. This has already been exploited in the past, for example, for the formation of various, high-spin alkali molecules [60, 65, 115, 120–122]. With our work on Ak-Ake molecules on helium droplets (see also ref. [88]) we extend the family of surface bound molecules and expand the HENDI approach towards a new class of strongly surface-coupled molecules, thereby offering novel perspectives for the deliberate molecule formation with helium nanodroplets.
The results for RbSr demonstrate the potential of the HENDI approach for the preparation and characterization of molecules with special relevance for experiments in the ultracold temperature regime, thereby connecting the fields of helium nanodroplet spectroscopy and ultracold molecular physics. The recorded excitation spectra provide a solid basis for the search for optimum pathways for the formation of ultracold ground state RbSr.
The next promising candidate for the characterization on helium droplets among the Ak-Ake molecules is RbCa because both Rb and Ca, are well under control in ultracold atomic physics and for both atoms Bose-Einstein Condensation has been achieved [5, 84]. As a further example with relevance to ultracold molecular physics, the formation of molecules containing Cr as a constituent may also be explored by the helium droplet isolation approach [78, 136].

4.4 Strontium Atoms and Dimers on Helium Droplets

In the course of the experiments on RbSr doped He nanodroplets interesting spectroscopic results about Sr atoms and Sr dimers on He_N were found. The present material is currently being prepared for a publication together with the data on Ca_2 presented in section 4.6 p99.

4.4.1 Sr Atoms

Figure 4.20 a) shows the excitation spectrum of the Sr 5s5p, $^1P^o \leftarrow 5s^2$, ^1S transition on helium droplets, recorded by REMPI-TOF spectroscopy. The sharp line at $\sim$21700 cm^{-1} corresponds to the transition of free atoms and originates from a background caused by the atomic beam from the pickup cells.

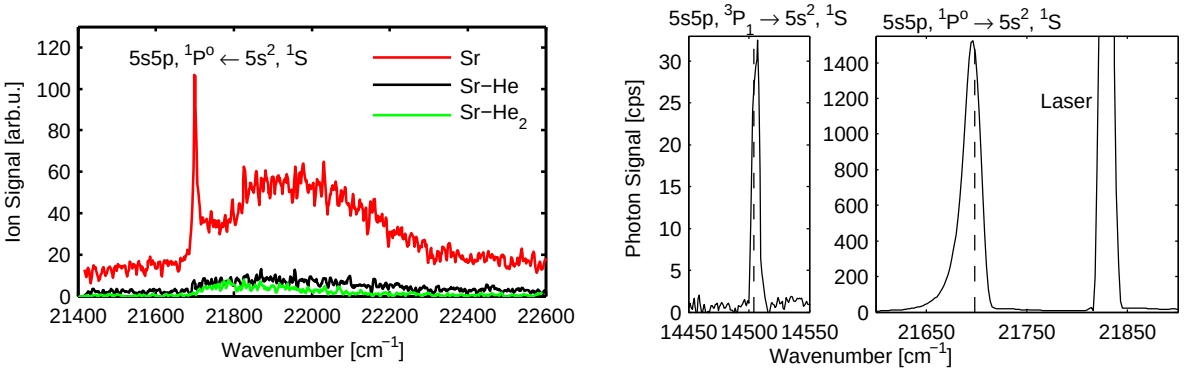

(a) (b)

Figure 4.20: a) Sr 5s5p, $^1P^o \leftarrow 5s^2$, ^1S excitation as recorded by REMPI-TOF spectroscopy. b) shows the corresponding emission of the Sr 5s5p, $^1P^o \rightarrow 5s^2$, ^1S transition, the broad line indicates an emission of Sr on the surface of the He droplet. The right panel shows the emission line from the Sr 5s5p, $^3P_1$ state, whose population is enhanced due to droplet mediated relaxation processes, as described in the text.

Our results reproduce the reported data of the Sr 5s5p, $^1P^o \leftarrow 5s^2$, ^1S transition [62] investigated by LIF spectroscopy well. Accordingly, the broad structure at higher energies of the atomic transition can be assigned to transitions into the overlapped 5p(Π) and 5p(Σ) molecular substates on the He droplet. As explained in the lithium section (4.2 p64), spectra of dopant-droplet systems can be described by the pseudo-diatomic model.
It is now interesting to ask if Sr remains on the droplet upon excitation of the 5p state, as this has been found to be the case for Rb [10], Cs [95] and Ba [107] for the corresponding excitations. For those three systems it has been shown that the non-desorption goes along with a very weak exciplex formation [158], which is also observed in the case of Sr, as can be see in fig. 4.20 a).
A reliable indication that Sr does stay on the droplet upon excitation of the 5p state is given in fig. 4.20 b). It shows the emission signal upon excitation at the maximum of the Sr 5p(Π/Σ) structure (21839 cm^{-1}) with an Ar^+ laser. The right panel shows that the emission line is broad (FWHM $\sim$20 cm^{-1}), in respect to the resolution of the spectrograph at the used slit width, which can be estimated from the FWHM of the laser ($\sim$15 cm^{-1}). This indicates that the emission happens from the upper molecular substate (most probably 5p(Π, $\nu' = 0$)) into vibrational levels of the 5s(Σ) ground state, resulting in a broadening of the emission line, as explained for Rb in ref. [10, 95]. The on-droplet emission signal cannot be separated from the emission of desorbed atoms.

The left panel in fig. 4.20 shows that a significant fraction of the excited Sr 5s5p, $^1P^o$ atoms relaxes into the Sr 5s5p, $^3P_1$ state upon excitation. This results in a comparatively strong emission signal of the Sr 5s5p, $^3P_1 \rightarrow 5s^2$, ^1S transition. The relaxation into the triplet state is classically forbidden, however the strength of the emission signal from the triplet state suggests that the He droplet mediates an efficient population of this state. Note that the emission still originates from free Sr 5s5p, $^3P_1$ atoms, as the small linewidth (FWHM $\sim$7 cm^{-1})) shows.

4.4.2 Sr Dimers on Helium Droplets

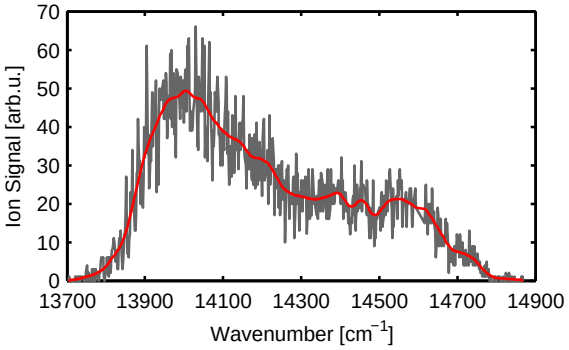

Figure 4.21: Excitation spectrum of the Sr_2 $1^1\Sigma_u^+ \leftarrow X^1\Sigma_g^+$transition, recorded with REMPI-TOF spectroscopy. In this experiment the pickup temperatures have been optimized for a Sr_2 pickup.

The REMPI-TOF excitation spectrum of Sr_2 in fig. 4.21 shows a broad structure and its form has a pronounced shoulder on the high energy side. This is probably due to the fact that two photons are needed for the ionization of the excited Sr_2 and hence the transition probabilities to an (upper) intermediate state might affect the shape of the structure.
Several theoretical calculations [17,30,81,82] as well as experimental investigations in free space as well as in various matrices [51,114,147,148] for Sr_2 are available. Results obtained for Sr_2 in argon and krypton matrices are well comparable to ours. The transitions found by Miller et.al. [114] in argon, show a Gauss-shaped peak form, extending from $\sim$13300 cm^{-1} to 14290 cm^{-1} with maximum at $\sim$14085 cm^{-1}. In krypton the same peak is shifted $\sim$380 cm^{-1} to lower energies. The maximum of the transition on He_N ($\sim$14010 cm^{-1}) lies very close to the maximum of the transition in Ar.
The shape of the structure in the matrix experiments is a pure Gaussian, in contrast, the structure shown in fig. 4.21 shows a shoulder on the high energy side and extends to slightly higher energies ($\sim$14700 cm^{-1}), as stated above the shoulder might be an effect of the two-photon ionization (subsequent to the one-photon excitation). Otherwise, the structure is surprisingly well comparable with the findings in Ar. Miller et.al. [114] give vibrational bands from $\sim$13800-14600 cm^{-1}, i.e. in the exactly same energy region as found by us. The fact that the excitation spectrum is at nearly the same position as obtained in Ar and Kr matrices together with the fact that the free molecular transition is at much lower energies indicates that the transition does not take place on the surface of the He droplet, but rather in the center of the droplet. This argument is further discussed in the Ca_2 section (4.6, p99).

The structure in Figure 4.21 is assigned to the $1^1\Sigma_u^+ \leftarrow X^1\Sigma_g^+$ transition with the atomic asymp-

totes Sr 5s4d, ^1D + Sr $5s^2$ for the excited state, based on high resolution data presented in ref. [148]. Considering the transition energy of ~12800 cm^{-1} given in ref. [148], the transition on He droplets is shifted by ~1500 cm^{-1} to higher energies, which is not unexpected for transitions in matrices. Additionally, this is the most likely transition, since other close-lying states are of triplet character ($^3\Sigma_u^+$ and $^3\Pi_u$) and cannot be excited from the singlet ground state.

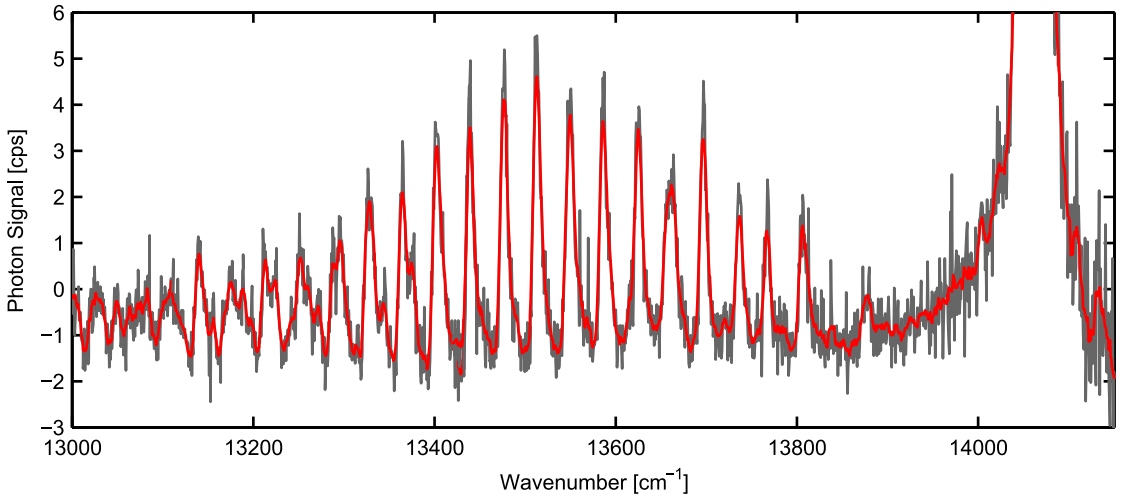

Figure 4.22: Dispersed fluorescence spectrum of the Sr_2 $1^1\Sigma_u^+ \rightarrow X^1\Sigma_g^+$transition.

Figure 4.22 shows the emission spectrum recorded upon excitation at ~14050 cm^{-1}. A fit of the single peaks to a Gaussian from ~13400 cm^{-1} upwards reveals a line spacing of 37 ± 2 cm^{-1} and a FWHM of 10 cm^{-1}. This fits the vibrational spacing given for the ground state by refs. [51,147] very well ($\omega_e = 40.3$ cm^{-1}).
The overlapped peak structures in the low energy part of the emission indicate that the spectrum is comprised of several vibrational bands. This is supported by the fact that the emission region is ~500-1000 cm^{-1} above the $1^1\Sigma_u^+(\nu' = 0) \rightarrow X^1\Sigma_g^+(\nu'' = 0)$ transition given in ref. [148], even though the spectrum originates from free Sr dimers, desorbed upon excitation. Thus, most probably, several vibrational bands of the upper state will take part in the emission. The vibrational spacing of the corresponding levels can be estimated from the Dunham coefficients given in refs. [147, 148]. For an overview, the transition energy T_e, harmonic constant ω_e and anharmonicity $x_e\omega_e$ of the ground and excited state are:

- $X^1\Sigma_g^+$: $D_e = 1082$ cm^{-1}, $\omega_e = 40.3$ cm^{-1}, $x_e\omega_e = 0.399$ [147]
- $1^1\Sigma_u^+$: $T_e = 12795$ cm^{-1}, $\omega_e = 80.7$ cm^{-1}, $x_e\omega_e = 0.230$ [148]

The vibrational spacing for the ground state is in the range of ~40-30 cm^{-1} for the first 12 levels and the spacing for the $1^1\Sigma_u^+$ state is in the range of ~60-80 cm^{-1} for the first 17 levels. The transition energy $1^1\Sigma_u^+(\nu' = 17) \rightarrow X^1\Sigma_g^+(\nu'' = 0)$ is at ~14100 cm^{-1} and thus above the values recorded in the emission spectrum in fig. 4.22. This means that for the eligible energy range the vibrational spacing of the excited state is roughly twice the spacing of the vibrational spacing for the ground state. An overlap of vibrational bands into the ground state from several vibrational states of the excited state will thus be hard to identify and separate. This is a possible explanation for the overlapped peaks in the energy range of ~13100-13400 cm^{-1}.

4.5 Rubidium-Calcium

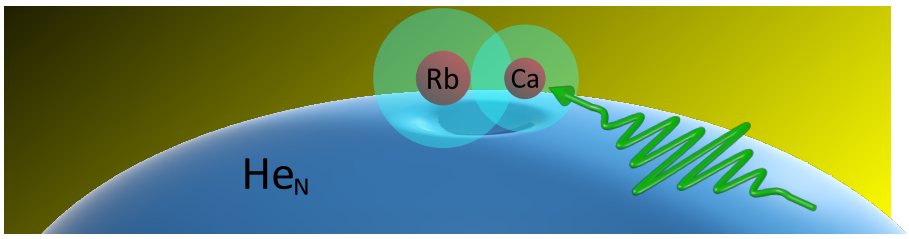

The third Ak-Ake molecule investigated in the course of this thesis was RbCa. Similar to RbSr, it is also a promising candidate for the production of a molecular quantum degenerate gas: On the one hand Bose-Einstein condensation has been achieved for Ca [84] and on the other hand recent theoretical calculations [54] show that parameters like the permanent dipole moment are favorable for the alignment in laser fields. Ref. [54] provides a good theoretical comparison of different combinations of Ak (Na, K, Rb) and Ake (Ca, Sr) molecules. According to these calculations RbCa is well comparable to RbSr for most parameters. The equilibrium distance R_e for the ground state potential is slightly smaller due to the lighter Ca and the depth of the potential ($\sim$900 cm^{-1}) is in the same range as for RbSr. These calculations and the similarity of Sr and Ca indicate that the spectra are well comparable to each other.
In the course of our investigation of RbCa on He$_N$ a REMPI-TOF spectrum in a spectral range of $13000 - 23000\,\mathrm{cm}^{-1}$ has been recorded and several transitions have been found. At this point, theoretical calculations are in progress and first results are used to describe the experimental findings presented below. Additionally, the assignment of peaks to molecular transitions is supported by a comparison to RbSr. A thorough investigation of the transitions at $16000\,\mathrm{cm}^{-1}$ and $17000\,\mathrm{cm}^{-1}$ with LIF spectroscopy did not lead to a fluorescence signal associated to RbCa, this is discussed in the corresponding section below.

As mentioned above, theoretical investigations are currently in progress and first results have been achieved. The experimental and theoretical data are currently prepared for a joint publication. The experiments were performed by Florian Lackner and myself, as well as the data acquisition and processing. The theoretical calculations are currently performed by Johann Pototschnig.

4.5.1 Mass Spectrum

Figure 4.23 shows the mass spectrum of RbCa recorded during a REMPI-TOF experiment in the spectral range of $15800 - 16500\,\mathrm{cm}^{-1}$. In contrast to RbSr, the single masses of the Ak and Ake monomers and dimers, as well as the Ak-Ake molecule are well separated. The spectrum is additionally simplified by the fact that Ca has only one significant isotope (^{40}Ca - 96.9% [103]). All relevant masses are denoted in the figure. It can be seen that both isotopologues of RbCa (^{85}Rb^{40}Ca, ^{87}Rb^{40}Ca) are efficiently formed on the He droplet. Since no other atoms or molecules contribute to these signals or lie in the vicinity, the sum of both is used in REMPI-TOF survey spectrum in fig. 4.25. Note that the strength of the RbCa molecule ion yield relative to the Ak and Ake monomer and dimer ion yield does not only depend on the pickup temperatures, but also on possible molecular dimer transitions in the same wavelength region. Furthermore, this may also increase the monomer background due to fragmentation of the dimers.

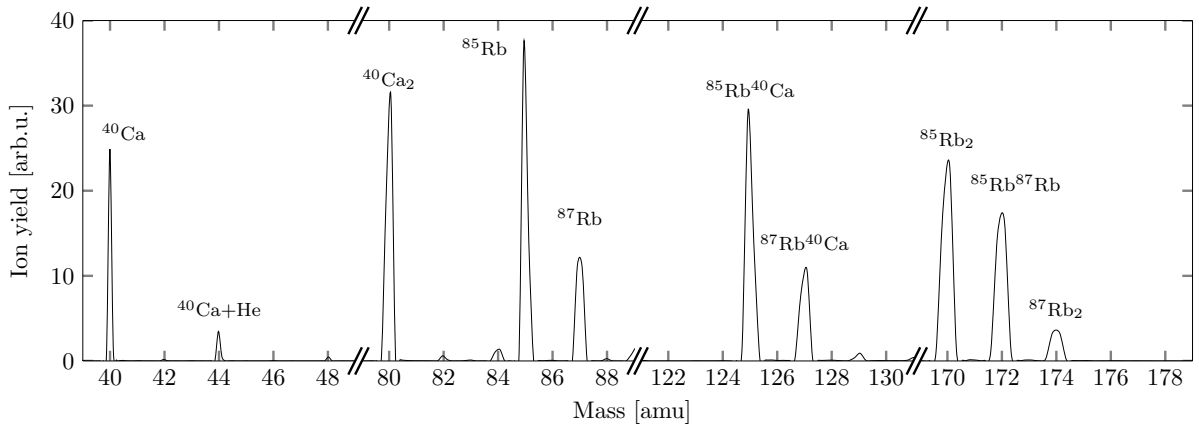

Figure 4.23: Example of a mass spectrum in a RbCa experiment, showing Rb and Ca monomers and dimers as well as the RbCa molecule, recorded during a REMPI-TOF experiment.

4.5.2 REMPI-TOF Survey Spectrum and Analysis of the Spectrum

The spectrum of RbCa recorded with REMPI-TOF spectroscopy in a spectral range of $13000 - 23000\,\mathrm{cm}^{-1}$ is shown in figure 4.25. At least six transitions can be identified.
Note that the relative heights of the peaks shown in figure 4.25 can only be tentatively compared to each other, since they mostly originate from different experiments. As mentioned in section 1.4 p6, the beam and pickup conditions for different experiments may vary and the signals were optimized for the respective conditions. These optimizations required different pickup temperatures and different laser pulse energies for each experiment. The REMPI-TOF overview spectrum in fig. 4.25 is comprised by spectra recorded by various laser dyes. They have been offset corrected, but not scaled and the laser pulse energies are within a range of $0.5 - 1.5\,\mathrm{mJ}$. The only exception is the signal above $20400\,\mathrm{cm}^{-1}$, at the respective experiment an unusually high ion yield was detected, even though the laser pulse energy was relatively low ($\sim 0.5\,\mathrm{mJ}$). Accordingly, the signal above $20400\,\mathrm{cm}^{-1}$ was scaled by a factor of 0.4. Several different experiments in this region showed that the spectral positions and shapes of the structures are completely reproducible.

The assignment of the single structures to molecular transitions is based on the first results of theoretical calculations by Johann Pototschnig. The calculated transition probabilities (FCF*TDM^2) are indicated in the figure as vertical bars. The transition probabilities have been scaled to fit the experimental data, but their relative heights with respect to each other still reflect the FCF*TDM^2 distribution (all bands have been scaled by the same factor). Generally, the theoretical values for the molecular transitions lie slightly lower in energy than the experimental values ($\sim$400 cm^{-1}) for all states, except for those above $22000\,\mathrm{cm}^{-1}$. This can be explained by the fact that the asymptotes of the RbCa PECs for large internuclear separations lie slightly below the related atomic levels, for some molecular states.
The theoretical method used by Johann Pototschnig gave a depth of the RbCa ground state of $\sim 1400\,\mathrm{cm}^{-1}$. The only other available value is lower ($\sim 900\,\mathrm{cm}^{-1}$ [54]), however, it has to be mentioned that the method in ref. [54] also underestimated the depth of the RbSr ground state. An overview of the potential energy curves for RbCa (also calculated by Johann Pototschnig), which were used to calculate the transition probabilities are shown in Figure 4.24.

In addition to the calculations, the results of the investigations of RbCa can be compared to RbSr as well as LiCa. This is shown in table 4.4. The left part of the table represents the atomic part. Here, the single atomic levels, which are relevant for the molecular states found in the

Ak-Ake molecules, are listed for the constituents (Li, Ca, Rb, Sr) of the three Ak-Ake molecules investigated. The SO splitting has been neglected and the term values for the triplet states of Sr and Ca have been taken from ref. [135].
The right part of the table represents the molecular part, the first column lists the molecular states arising from the combination of the respective atomic states (only molecular states which can be excited from the ground state are given). The rightmost three columns give the wavelength where molecular transitions for each Ak-Ake molecule have been found in our experiments (approximate peak center). RbCa is well comparable to RbSr as noted above, hence an additional column has been added, giving the energetic difference between the Ca and Sr atomic levels (Δ_{Ca-Sr}).
As the table shows, in general the Ca states lie higher in energy than the Sr states. Molecular states which are not perturbed by the interaction with others can thus be estimated to lie higher for RbCa in comparison to RbSr. Additional conclusions can be drawn from the table and will be discussed in the following sections dealing with the single structures in the REMPI-TOF spectrum, in fig. 4.25.

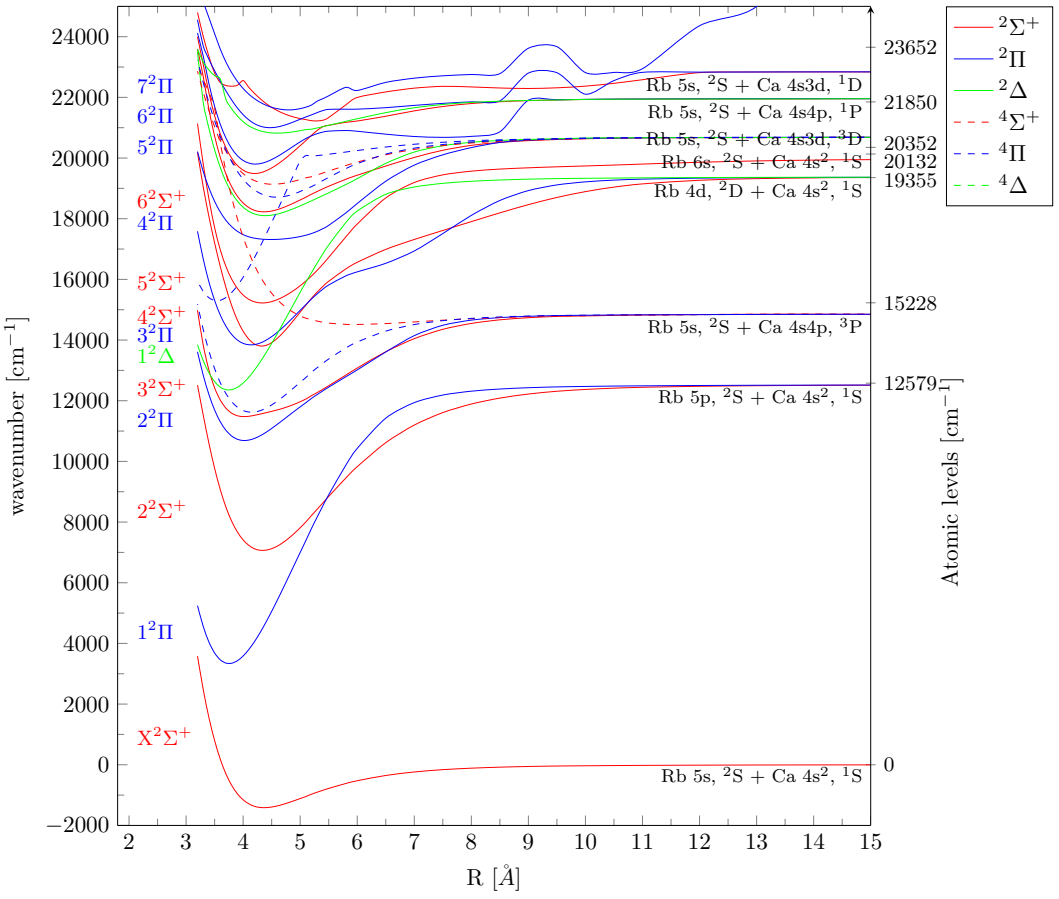

Figure 4.24: Overview of the potential energy curves of RbCa, as calculated by Johann Pototschnig [133].

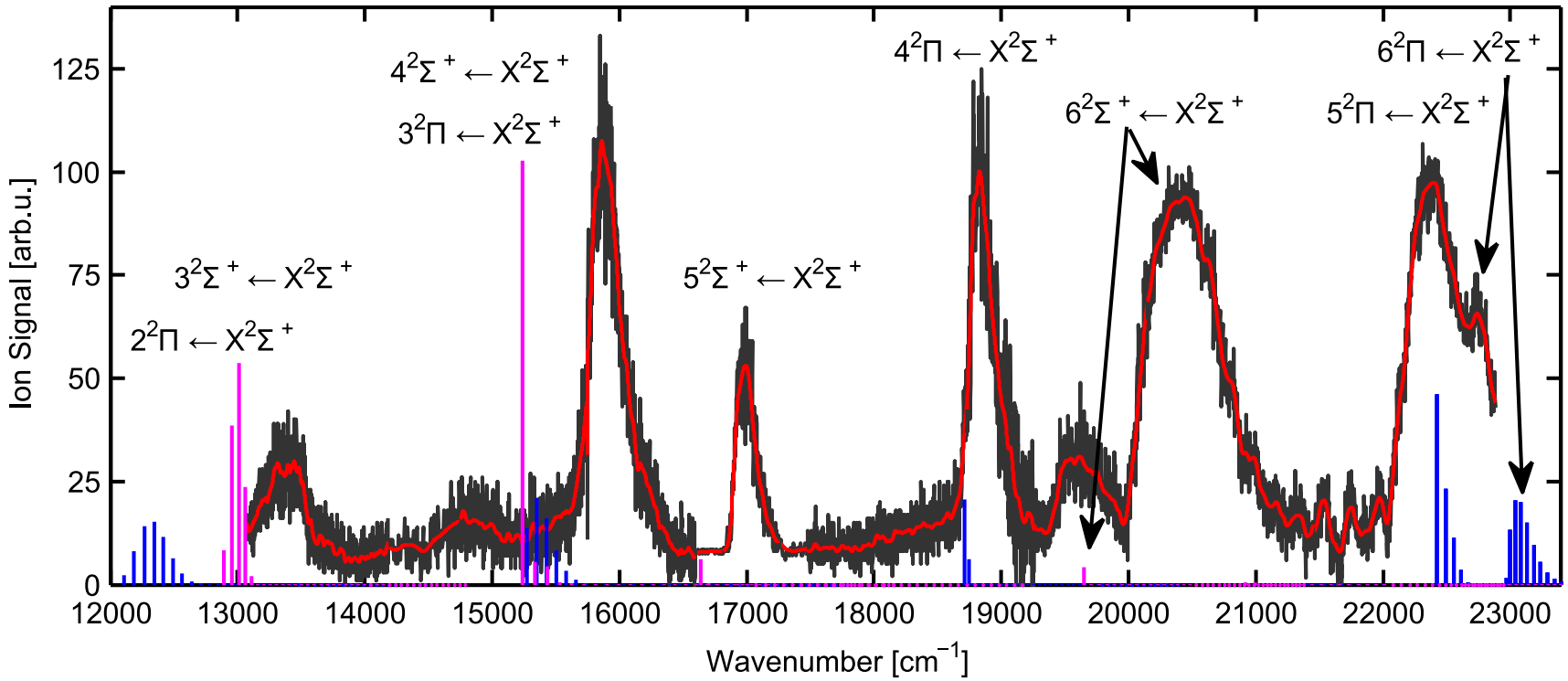

Figure 4.25: REMPI-TOF survey spectrum of RbCa in a spectral range of $13000 - 23000\,\mathrm{cm}^{-1}$. First results of theoretical transition probabilities (FCF*TDM^2), calculated by Johann Pototschnig, are indicated as vertical bars, magenta bars indicate a transition into a $^2\Sigma^+$ state, blue bars into a $^2\Pi$ state. The gray line represents the ion yield of the sum of the two RbCa isotopologues ^{125}RbCa + ^{127}RbCa as recorded, the red line has been smoothed by convolution with a Gaussian.

Table 4.4: Comparison of the atomic levels of Rb, Ca and Sr to estimate the position of the RbCa molecular levels relative to the RbSr levels.

Li		Rb		Ca[a]		Sr[a]		$\Delta_{\text{Ca-Sr}}$	Ak-Ake	LiCa[b]	RbSr[b]	RbCa[b]
Conf.	cm^{-1}	Conf.	cm^{-1}	Conf.	cm^{-1}	Conf.	cm^{-1}	cm^{-1}	State	cm^{-1}	cm^{-1}	cm^{-1}
2s ^{2}S	0	5s ^{2}S	0	4s^2 ^{1}S	0	5s^2 ^{1}S	0		$X^2\Sigma^+$	(∼-2600)	(∼-1000)	(∼-1000)
2p ^{2}P	14904	5p ^{2}P	12579	4s^2 ^{1}S	0	5s^2 ^{1}S	0		$^2\Pi$ $^2\Sigma^+$			
2s ^{2}S	0	5s ^{2}S	0	4s4p ^{3}P	15263	5s5p ^{3}P	14702	561	$^2\Sigma^+$ $^2\Pi$		∼12000 ∼12300	 ∼13300
2s ^{2}S	0	5s ^{2}S	0	4s3d ^{3}D	20357	5s4d ^{3}D	18254	2103	$^2\Sigma^+$ $^2\Pi$	∼15500 ∼19500	∼14000 ∼15000	∼15900 ∼17000
		4d ^{2}D	19355	4s^2 ^{1}S	0	5s^2 ^{1}S	0		$^2\Sigma^+$ $^2\Pi$		 ∼16600	 ∼18800
3s ^{2}S	27206	6s ^{2}S	20132	4s^2 ^{1}S	0	5s^2 ^{1}S	0		$^2\Sigma^+$		∼19800	
3s ^{2}S	0	5s ^{2}S	0	4s3d ^{1}D	21850	5s4d ^{1}D	20150	1700	$^2\Sigma^+$ $^2\Pi$	∼21500 ∼22500		
3s ^{2}S	0	5s ^{2}S	0	4s4p ^{1}P	23652	5s5p ^{1}P	21700	1952	$^2\Sigma^+$ $^2\Pi$	∼24500 ∼24500	19600	
3p ^{2}S	30925	6p ^{2}S	23754	4s^2 ^{1}S	0	5s^2 ^{1}S	0		$^2\Sigma^+$ $^2\Pi$			
1s^2 ^{1}S	43487	4p^6 ^{1}S	33691	5s^2 ^{1}S	0	5s^2 ^{1}S	0		$AkAke^+$			

[a] SO interaction has not been taken into account, the term value has been taken [135] for the Ca and Sr triplet states.
[b] Levels found in our investigations, the depths of the ground state potentials are taken from calculations by Johann Pototschnig [133] and refs. [53, 54, 169].

Structure at 13000 cm^{-1}

The small structure at 13000 cm^{-1} can be assigned to the $3^2\Sigma^+$ transition already on the basis of a comparison to RbSr. No other molecular states are close and the states $2^2\Pi$ and $3^2\Sigma^+$, related to the Rb 4s, ^2S + Ca 4s4p, ^{3}P asymptote are not perturbed. Hence, they are expected to lie $\sim$600 cm^{-1} higher than for RbSr. This is perfectly confirmed by the theoretical calculations of Johann Pototschnig [133].

Structure at 15900 cm^{-1}

The structure in the REMPI-TOF spectrum shows a steep rising edge and a broad shoulder to higher energies. The calculations suggest an assignment of this structure to the molecular states originating from the Rb 4d, ^{2}D + Ca 4s^2, ^{1}S atomic asymptote. As the transition probabilities in fig. 4.25 and also the PECs in fig. 4.24 show, the transitions into the two corresponding molecular states are overlapped. Hence, the structure at 15900 cm^{-1} can be assigned to the superimposed $3^2\Pi/4^2\Sigma^+ \leftarrow X^2\Sigma^+$ transitions. The $4^2\Sigma^+$ state has shown a vibrational resolution for LiCa as well as for RbSr, in comparison with theoretical calculations two reasons can be named why this state is not resolved for RbCa:

- The overlap of the $4^2\Sigma^+$ state with the $3^2\Pi$ state.
- The rapid decrease of the FCFs for the transitions into the $4^2\Sigma^+$ state ($\mathrm{FCF}_{\nu'=0\leftarrow\nu''=0} \approx 0.9$, $\mathrm{FCF}_{\nu'=1\leftarrow\nu''=0} \approx 0.05$).

The first argument states that, even if both states were vibrationally resolved, it would be difficult to separate the single peaks for the overlapped structure.
The second argument also explains the shape of the structure at 15900 cm^{-1}: The high transition probability into the vibrational ground state of the $4^2\Sigma^+$ state accounts for the steep rising edge. The broad shoulder, extending to higher energies, originates from a transition into the $3^2\Pi$ state, since above the energy for the $4^2\Sigma^+(\nu' = 0) \leftarrow X^2\Sigma^+(\nu'' = 0)$ transition, the transition probabilities into vibrationally excited levels of the $3^2\Pi$ state exceed those of transitions into the $4^2\Sigma^+$ state, this is reflected by the vertical bars for the respective transitions in fig. 4.25.

Structure 17000 cm^{-1}

As can be seen in table 4.4, the energetic ordering of the Ca and Sr states is different above the Ca ^{3}P state. The Ca 4s3d, ^{3}D atomic state lies higher than the corresponding Sr state. It does even lie slightly above the Rb 6s, ^{2}S state and although the two atomic states are only separated by $\sim$200 cm^{-1} the corresponding PECs of RbCa do not show a large interaction (see fig. 4.24). According to the calculations the structure at 17000 cm^{-1} can be assigned to the $5^2\Sigma^+ \leftarrow X^2\Sigma^+$ transition, where the upper state belongs to the Rb 6s, ^{2}S + Ca 4s^2, ^{1}S asymptote.
This transition has been recorded with different laser pulse energies in order to study saturation effects. REMPI-TOF spectra for the $5^2\Sigma^+ \leftarrow X^2\Sigma^+$ transition for four different pulse energies are shown in figure 4.26. For a better comparison the signal intensities have been scaled to one. It can be seen that the structure recorded with the highest laser energy (4 mJ) is significantly broadened in respect to the others, which indicates a saturation of the transition [4]. Since there is no significant difference in the shape or width of the structures recorded with a laser pulse

[4] Note that the present case is a two-photon ionization with only one laser and both the excitation and the ionization can be saturated.

energy of 0.3 mJ and 0.7 mJ, the latter was used in the overview spectrum.
The shape of the peak can be explained by the calculated Franck-Condon-factors: Only the first factor is high, the successive factors decrease by an order of magnitude each ($FCF_{\nu'=0-2\leftarrow\nu''=0} \approx 0.95, 0.04, 0.004, 0.0002$). This has also been observed for the transitions into the $4^2\Pi$ state of RbSr.

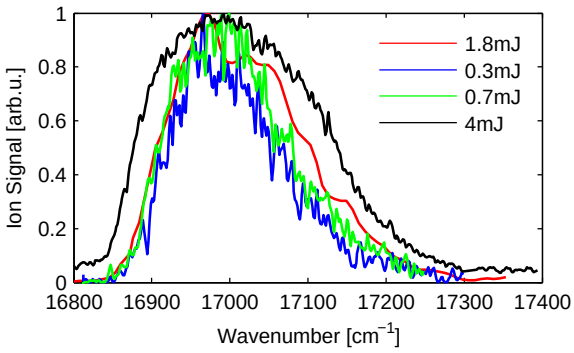

Figure 4.26: Close-up of the RbCa related structure around 17000 cm^{-1}. Excitations at different pulse energies are shown. To detect possible saturation effects all have been scaled to one. Note that the signal obtained with 4 mJ pulse energy was obtained in a different experiment.

Structures at 18800 cm^{-1} and 19600 cm^{-1}

The structure at ∼18800 cm^{-1} is assigned to the $4^2\Pi \leftarrow X^2\Sigma^+$ transition. The excited molecular state dissociates to the Rb 5s, ^{2}S + Ca 4s3d, ^{3}D asymptote. The asymmetric shape with a steep rising edge is in good agreement with the calculations, which show high FCFs into the first two vibrational transitions ($FCF_{\nu'=0,1\leftarrow\nu''=0}$ =0.76,0.23).

The structure around 19600 cm^{-1} does not result from a RbCa transition. It is an effect related to the atomic Rb 6s, ^{2}S← Rb 5s, ^{2}S transition on He droplets (free atom line at 19355 cm^{-1}). A similar effect has been found in ref. [24,65]. In ref. [65], He droplets were doped with Na and K. In a LIF experiment, it was observed that an excitation spectrum of a Na_2 triplet state can be recorded by monitoring only a K emission line. This was explained by a collisional energy transfer between a Na_2 molecule and a separated K atom on the same He droplet.
The structure at 19600 cm^{-1} in the REMPI-TOF spectrum of RbCa may be related to the same phenomenon. This becomes clear in fig. 4.27, showing the ion yields for RbCa, Rb and Rb-He. In the spectral range of 19300 − 19700 cm^{-1}, the RbCa signal clearly follows the Rb and Rb-He signal and the rising edges of all signals are at the atomic Rb 4d, ^{2}D← Rb 5s, ^{2}S transition. The exact physical process remains unclear, but several mechanisms are possible. One explanation would be a helium droplet doped with Ca_2 inside the droplet[5] and a Rb atom on the surface of the droplet. It has been shown, that upon ionization, the Rb ion can immerse into the droplet [159]. It is possible that the immersed Rb^+ dissociates the Ca_2 and forms a $RbCa^+$ molecule, which is subsequently detected by the TOF spectrometer.

[5]Spectra shown in section 4.6 p99 show that Ca_2 is located inside the droplet.

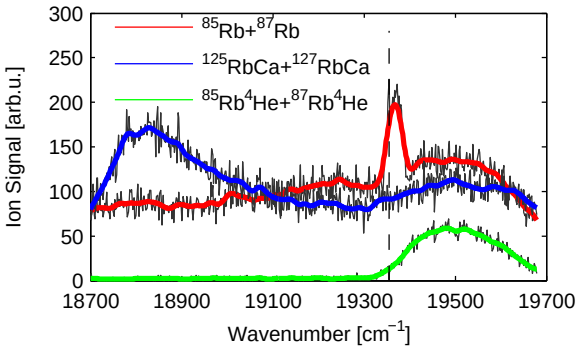

Figure 4.27: Close- up of the transition around 19600 cm^{-1} in the RbCa ion yield. The ion yield for Rb, Rb-He and RbCa are shown, the dashed vertical line indicates the free atom Rb 4d, ^{2}D← Rb 5s, ^{2}S transition. It can be seen that the RbCa signal follows the Rb and Rb-He signal. The peak in the RbCa ion yield is not correlated to a RbCa transition, as explained in the text.

Structures above 20000 cm^{-1}

For transition energies above 20000 cm^{-1} the experimental results for RbCa are more refined than for RbSr. Remarkably, between the two broad structures at 20400 cm^{-1} and 22400 cm^{-1} some vibrationally resolved lines can be seen (shown in detail in figure 4.28). The vibrational lines are Gauss-shaped and have a spacing of ∼200(10) cm^{-1}. The series can be followed from the maximum of the peak of the lower lying structure (21600 cm^{-1}) to the onset of the transition at higher energies (22000 cm^{-1}). The vibrational lines have been reproduced in several experiments, but could not be separated better from the energetically higher or lower-lying transitions. Unfortunately their origin also remains obscure. The vibrational lines only occur for the mass window of the RbCa isotopologues and a contribution of dimers or triatomic molecules (Rb_2Ca or Ca_2Rb) can be excluded. But neither the calculations nor the comparison to RbSr indicate a PEC for such high excitation energies, bound deeply enough to harbor vibrational lines with a spacing of ∼200(10) cm^{-1}. Additionally, all theoretically calculated transitions into excited states with a significant transition probability which lie in the vicinity can be assigned to other structures.

The structure at 20400 cm^{-1} is tentatively assigned to the $6^2\Sigma^+ \leftarrow X^2\Sigma^+$ transition, since the peak around ∼19600 cm^{-1} has been found not to originate from a RbCa molecular transition.

Theoretical calculations suggest to assign the structure at 22400 cm^{-1} to the $5^2\Pi \leftarrow X^2\Sigma^+$ transition and the shoulder at higher energies (22700 cm^{-1}) to the $6^2\Pi \leftarrow X^2\Sigma^+$. The transition probabilities into the corresponding $^2\Sigma^+$ states are negligible.
The $6^2\Pi$ state adiabatically correlates to Rb 5s, ^{2}S + Ca 4s4p, ^{1}P in the separated atom limit and the $6^2\Pi$ state to the Rb 5s, ^{2}S + Ca 4s3d, ^{1}D asymptote.

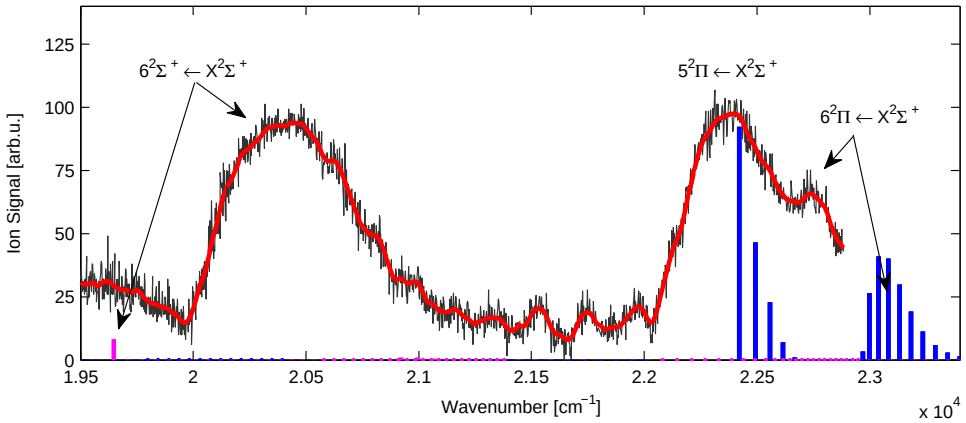

Figure 4.28: Close-up of the higher excited states of RbCa. Between the two strong transitions around 20400 cm^{-1} and 22400 cm^{-1} some vibrationally resolved states can be seen.

4.5.3 LIF Experiments

In order to find a vibrationally resolved RbCa transition, the structures at 17000 cm^{-1} and 15900 cm^{-1} were investigated with LIF spectroscopy. Additionally, a LIF spectrum in the spectral range of the Coherent 899 Ti:Sa ring laser (11100 – 13000 cm^{-1}) was recorded.

LIF Spectroscopy in the Spectral Range of 11100 – 13000 cm^{-1}

This corresponds to the wavelength range of the mid-wave optics set of the Coherent 899 Ti:Sa ring laser. A complete scan across this range was performed, the resulting spectrum is shown in fig. 4.29. No signal corresponding to RbCa could be found. At 12579 cm^{-1} and 12817 cm^{-1} the Rb D1 and D2 lines (transitions into the Rb 5p $^2P_{1/2}$ and $^2P_{3/2}$ states) dominate the spectrum. The broad structures extending to higher energies from the atomic lines correspond to the transitions on the helium droplets. These are well researched, see e.g. refs. [21,91]. The D1 and D2 structures may cover possible RbCa transitions in this range.
Below the D1 line (11100-12550 cm^{-1}), the quantum efficiency of the PMT begins to decrease rapidly: It is at 10% for 11800 cm^{-1} and 2% for 11100 cm^{-1}. As the theoretical calculations (see fig. 4.25) show, the only transition in this region is into the $2^2\Pi$ state. Depending on the accuracy of the calculation the transition is below or in the same energy range as the D1 line. Either due to the dominant D1 line, or due to the low quantum efficiency of the PMT no trace of this transition has been detected in the LIF signal, as can be seen in fig. 4.29.

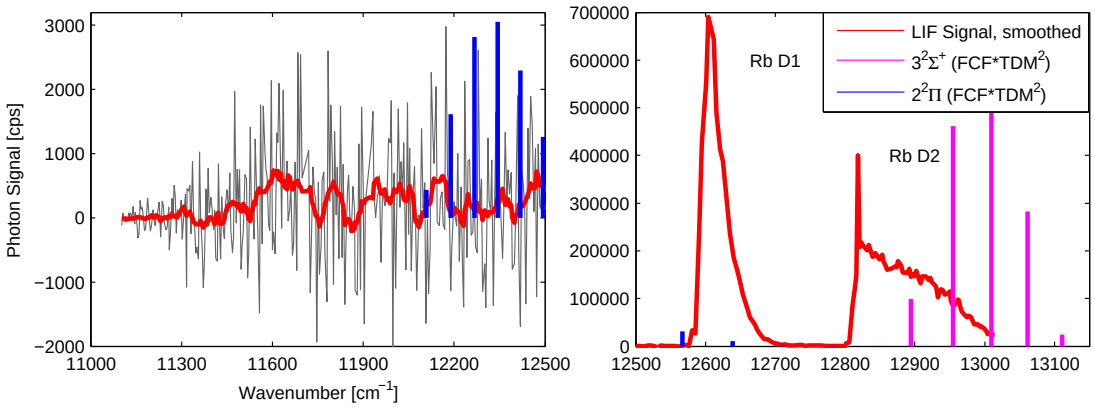

Figure 4.29: Investigation of RbCa in a spectral range of $11100 - 13000\,\mathrm{cm}^{-1}$ by LIF spectroscopy. The Rb D lines dominate the spectrum, below the D1 line the quantum efficiency of the photomultiplier decreases rapidly. The theoretical transition probabilities into the $3^2\Sigma^+$ and $2^2\Pi$ states are shown as vertical bars. Note that they are scaled differently in the two panels.

LIF Spectroscopy of the Structure at 17000 cm^{-1}

In the spectral range between $16500 - 17100\,\mathrm{cm}^{-1}$ the Rb_2 $(2)^3\Pi_g \leftarrow a^3\Sigma_u^+$ transition reported in ref. [9, 20] has been found, see fig. 4.30. Unfortunately, no signal corresponding to RbCa could be identified. However, the LIF experiment was performed subsequent to a REMPI-TOF experiment, which had been recorded with the same experimental settings, thus the formation of RbCa on the He droplets was verified for the current experimental conditions.
In this wavelength range the REMPI-TOF spectrum shows a transition into the RbCa $5^2\Sigma^+$ state. This state is crossed by a dissociative part of the $1^4\Sigma^+$ state, close to the minimum of the PEC, which may cause a complete predissociation of RbCa (see fig. 4.24). However, this should result in a fluorescence signal of the excited fragments. A dissociation into metastable Ca triplet states and ground state Rb atoms, on the other hand, would explain the lack of an emission signal. Finally, the quenching mechanism preventing an emission, detectable with our experimental setup, remains obscure.

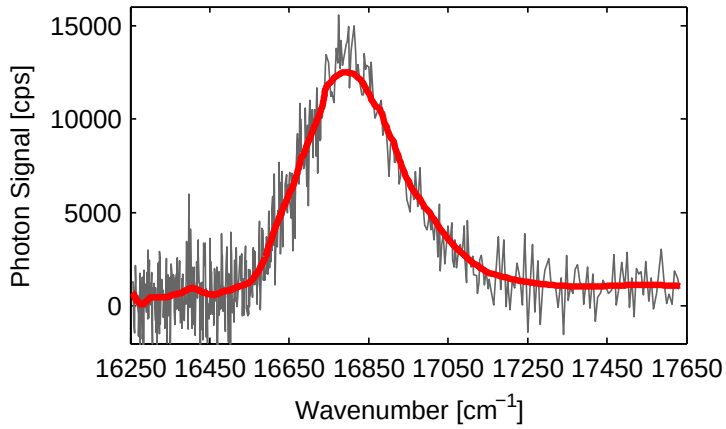

Figure 4.30: Investigation of RbCa in the spectral range of $16500 - 17100\,\mathrm{cm}^{-1}$, by LIF spectroscopy. Only the Rb_2 $(2)^3\Pi_g \leftarrow a^3\Sigma_u^+$ transition reported in refs. [9, 20] has been found.

LIF Spectroscopy of the Structure at 15900 cm^{-1}

Another LIF spectrum was recorded for the spectral range of 14450 – 16450 cm^{-1}. In this wavelength region several dimer and trimer transitions exist. The following transitions have been found (see fig. 4.31).

- Rb_2 $(1)^1\Pi_u \leftarrow a^1\Sigma_g^+$ [120]
- Rb_3 $3^4E' \leftarrow 1^4A_2'$ [120]
- Ca_2 $A^1\Sigma_u^+ \leftarrow X^1\Sigma_g^+$ [128]

The Rb dimer and trimer transitions cannot be separated in the LIF method and merge into a single peak in the spectral range between 14800−15200 cm^{-1}. The Ca_2 transition (for a detailed discussion see section 4.6 p99) appears as a broad structureless peak [6] between 15200 – 16000 cm^{-1}. The presence of a molecular state for both Rb_2 and the Ca_2 in the investigated wavelength range, allows to optimize the pickup temperatures for a relatively low dimer background signal of both species. If the dimer pickup is low, the monomer pickup of both species is nearly at its optimum, i.e. the optimum conditions for the formation of RbCa are achieved. The results of this approach are shown in fig. 4.31: The red line shows the LIF signal for a pure Rb pickup, hence only the Rb_2/Rb_3 transition can be seen. Then the pickup temperature for Ca has been increased, resulting in the blue line. At this point all transitions (Rb_2/Rb_3 and Ca_2) are quite high, i.e. the temperatures for both, Rb and Ca, are too high. Therefore, the pickup temperatures of Rb and Ca have been lowered, so that both dimer signals were minimized (black and green lines). However, no RbCa signal could be found. This means that no emission signal can be found for the RbCa transition excited around ∼15200 cm^{-1} in the LIF spectrum.

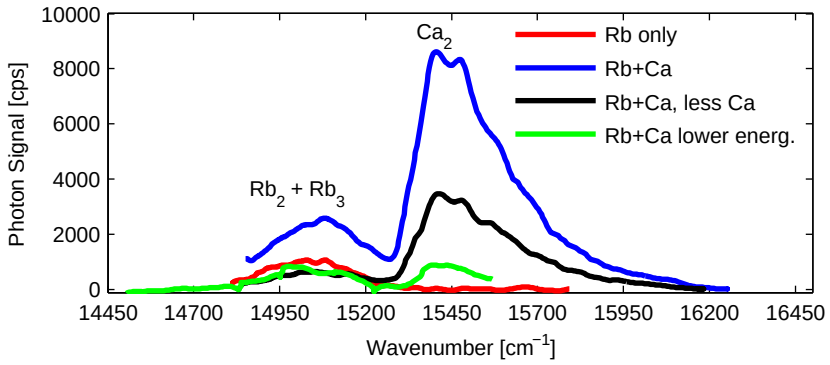

Figure 4.31: LIF investigation of RbCa in the spectral range of 14450 – 16450 cm^{-1}. The Rb_2 $(1)^1\Pi_u \leftarrow^1 \Sigma_g^+$, Rb_3 $3^4E' \leftarrow 1^4A_2'$ [120] and Ca_2 $A^1\Sigma_u^+ \leftarrow X^1\Sigma_g^+$ [128] transitions have been found in this range, allowing to optimize the pickup conditions for RbCa. However, no RbCa signal was found. The different signals have been recorded for different pickup temperatures. All signals have been smoothed by convolution with a Gaussian.

The PECs of RbCa (fig. 4.24) show that both the $3^2\Pi$ and the $4^2\Sigma^+$ state are crossed by the $1^2\Delta$ state close to the minimum of the PEC. This provides a possible reason for the absence of detectable fluorescence from these states. Assuming that the crossing $1^2\Delta$ state facilitates a similar relaxation mechanism as found for RbSr, but even more efficient, the excited RbCa

[6] The structure of the transition is lost, because of the fast scan speed and the perturbation by Rb, as well as by the smoothing of the data

molecules will either dissociate or be transferred to a lower-lying state. It remains unclear why no fluorescent light is detected, since an emission from both the $3^2\Sigma^+$ and the $2^2\Pi$ is well within our detection limits. Only a transfer to the $2^2\Sigma^+$ and the $1^2\Pi$ states would result in an emission too far in the infrared to be detected by our methods. Such relaxation processes could be enhanced by the helium droplet.

4.6 Calcium Dimers on Helium Droplets

To complete the picture, in the course of our investigations of RbCa on He droplets also one interesting transition for Ca_2 has been found. The transition has already been mentioned in the explanation of the LIF experiments on RbCa above. Figure 4.32 shows the Ca_2 transition as recorded with LIF spectroscopy, in contrast to the explanation above the signal has been optimized for Ca_2 pickup and the Rb pickup cell has been cooled down.

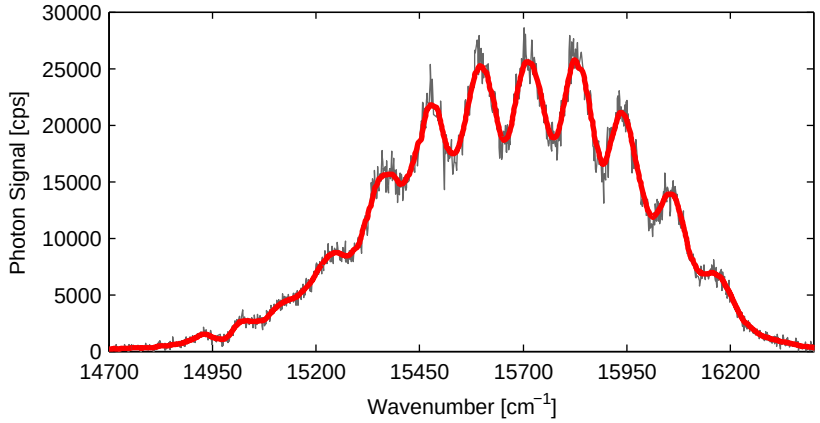

Figure 4.32: Ca_2 $A^1\Sigma_u^+ \leftarrow X^1\Sigma_g^+$ transition on/in He droplets, recorded with LIF spectroscopy.

As can be seen in the figure the transition shows a broad structure extending from 14800 to 16200 cm^{-1} and several vibrational transitions are resolved. The structure is assigned to the $A^1\Sigma_u^+ \leftarrow X^1\Sigma_g^+$ transition based on ref. [1,114]. According to theoretical calculations [1,25,82] the $A^1\Sigma_u^+$ state correlates to the Ca 4s3d,^{1}D+4s^2,^{1}S states. This seems reasonable as it is the same state as has been excited for Sr_2, see section 4.4 p83.

This $A^1\Sigma_u^+ \leftarrow X^1\Sigma_g^+$ transition has been recorded in liquid He [128], in solid krypton [114], in argon and neon [50] and in free space [16,69]. This allows a comparison of the same transition in several different matrices. A comparison of the position of the vibrational lines and their spacing for the Ca_2 transition in He II, Kr and Ar to our data is given in table 4.5. The values have been obtained by fitting a sum of Gaussians to the whole structure.
The energy shift of the dimer transition in the different matrices in comparison to the free space values is comparable to that of Sr_2: The shift between He droplets, liquid He and Argon is small (in this case negligible) and in the order of $\sim$400 cm^{-1} between Ar and Kr. For free molecule transitions, ref. [69] gives an energy of $T_e = 14251(66)\,cm^{-1}$. The Ca_2 on He_N transition is hence less shifted in respect to the free space transition than the Sr_2 transition ($\sim$500 cm^{-1} and $\sim$1500 cm^{-1} respectively).
Our results are best comparable to the liquid He data, the transition reported in ref. [128] is in the exactly same spectral range as the recorded one and most of the same vibrational levels $\nu' = 1-12$ could be resolved. The line centers of the single vibrational transition fall, with a few exceptions, within the uncertainty limits of the values obtained in liquid He II. This is actually a strong indicator that this transition has not been excited on, but in the He droplet, similar to Sr_2, see section 4.4 p83.
The solvation of dopants on He droplets is an interesting question and has been treated in many publications [4,26,61]. It was shown that all Ak metals and the heavier Ake metals (Ca, Sr

and Ba) are located on the surface of the droplet [107, 138, 153]. Upon excitation most of these species desorb from the droplet with the exception of Cs, Rb and Ba upon the excitation into their $P_{1/2}$ and P_1 states, respectively [10, 95, 107]. It has also been shown that the presence of a solvated dopant (e.g. Xe) can cause an immersion of the surface-located dopant [61, 109]. So it is not a priori clear where the dopants are located: On or in the He droplet. The present indication of Ake dimers residing in the droplet is interesting, since the observed spectra of high spin alkali dimers, as well as Ak-Ake molecules did show indications for these molecules to be located on the surface of the droplet. However, the interaction energy between Ake atoms and the He droplet is larger than for Ak atoms, which might account for a different behavior of the Ake dimers. Additionally, it has been shown that Ak clusters can immerse into the droplet when they reach a certain size [39, 40, 144]. The similarity of the excitation spectrum of the Ca_2 as well as the Sr_2 transition on He droplets to other matrices and especially of Ca_2 on He_N to liquid He are undeniable indicators that these two Ake dimers are immersed into the droplet. Note that the emission spectra still show that they desorb from the droplet upon excitation.

Table 4.5: Vibrational bands for the $A^1\Sigma^+ \leftarrow X^1\Sigma_g^+$ transition of Ca_2. Uncertainties are in the range of $5\,cm^{-1}$.

$\nu' \leftarrow \nu''$	this work		He II [128]		solid Kr [114]		solid Ar [113]	
	$\bar{\nu}$ cm^{-1}	spacing cm^{-1}	$\bar{\nu}$ cm^{-1}	spacing cm^{-1}	$\bar{\nu}$ cm^{-1}	spacing cm^{-1}	$\bar{\nu}$ cm^{-1}	spacing cm^{-1}
0			14835		14432			
1	14930		14912	77	14550	118	14900	
2	15022	92	15013	101	14667	117	15015	115.0
3	15134	112	15138	125	14786	119	15120	105.0
4	15240	106	15235	97	14905	119	15228	108.0
5	15364	123	15336	101	15024	119	15340	112.0
6	15479	115	15461	125	15140	116	15452	112.0
7	15595	116	15570	109	15256	116	15562	110.0
8	15714	119	15672	102	15373	117	15676	114.0
9	15828	115	15801	129	15489	116	15788	112.0
10	15940	112	15922	121	15603	114	15900	112.0
11	16054	113	16055	133	15718	115	16010	110.0
12	16163	109			15833	115	16120	110.0
13					15949	116		

CHAPTER 5

Summary

The goal of this work was the investigation of alkali-alkaline earth metal (Ak-Ake) molecules on helium nanodroplets. After the preparation of the necessary experimental requirements, the formation of Ak-Ake molecules could be verified on the example of the lithium-calcium molecule. Since this molecule had been studied before, both experimentally and theoretically, it provided a good testing ground for an approach by helium nanodroplet isolation spectroscopy (HENDI). We were able to show that our method works well and that Ak-Ake molecules can be formed and studied on He_N. Furthermore, we have shown that free molecule data can be retrieved from the experimental data, thus supporting theoretical studies and providing valuable input to benchmark theoretical calculations.

The next molecule, rubidium-strontium (RbSr), was the primary goal of this thesis. Recently, this molecule has attracted increasing interest in ultracold molecular physics, since it is the most promising candidate for the achievement of a molecular quantum degenerate gas with a permanent electric and magnetic dipole moment. Despite this high interest and several thorough theoretical studies, RbSr eluded experimental investigations up to now - a perfect challenge for helium nanodroplet isolation spectroscopy. The HENDI approach allowed us to form and characterize the RbSr molecule utilizing a successive set of three spectroscopic methods: Resonance enhanced multi-photon ionization time-of-flight (REMPI-TOF) spectroscopy, laser induced fluorescence (LIF) spectroscopy and dispersed emission spectroscopy. Several electronic transitions have been identified and a vibrationally resolved state allowed the extraction of free molecule parameters for the RbSr molecule. Moreover, information about the ground state was obtained from dispersed emission spectra. The latter also gave an insight into the relaxation dynamics of RbSr on He droplets, which is dominated by non-radiative, droplet mediated mechanisms.

Recently, the RbCa molecule was investigated by the same means. The experience gained in the course of the experiments with LiCa and RbSr made an efficient and thorough investigation of yet another previously uninvestigated molecule on He_N possible. Interestingly, LIF experiments on transitions, identified in the REMPI-TOF excitation spectrum, showed the presence of quenching mechanisms suppressing fluorescent light beyond the detection limit. Theoretical calculations are currently in progress and first results, together with a comparison to RbSr, have been used to describe the experimental data. The true nature of the quenching mechanisms still remains obscure, but future experiments with infrared-sensitive detectors may shed light on them.

Besides the results on the Ak-Ake molecules, insights into the interaction of lithium, strontium

and calcium atoms as well as their dimers with the He droplet were gained. The inherent mass-sensitivity of REMPI-TOF spectroscopy permitted the detection of interesting Ak, Ake atoms and dimer features during the Ak-Ake experiments and the simple pickup process enabled an easy optimization of the desired signal. Therefore, various studies of Li, Ca, Sr and their dimers doped to He_N were performed, consequently leading to the publication of 'collateral' articles.

In summary it can be stated that in the course of this PhD thesis a combination of well renowned techniques was established and developed for the effective characterization of tailored molecules: Helium nanodroplet isolation spectroscopy has once more proven to be a powerful tool to form and hold tailored, weakly bound molecules. The simple doping method of the droplet allows to dope it with virtually any atomic and molecular species and their cold temperature will facilitate the formation of many exotic molecules. The following combination of spectroscopic techniques allows for an efficient characterization of such molecules: Resonance enhanced multi-photon ionization time-of-flight spectroscopy enables the acquisition of an excitation spectrum of the molecule over a wide energy range ($>10000\,cm^{-1}$) in a reasonable timeframe. Molecular transitions up to highly excited states can be quickly identified this way. A closer and complementary investigation of selected transitions is provided by laser induced fluorescence spectroscopy, while at the same time verifying the existence of fluorescent light. A successive study of this emission by dispersed fluorescence spectroscopy then provides access to free molecules, since they desorb from the droplet upon excitation.
This effective scheme allows an efficient formation and reliable characterization of virtually arbitrary atoms and molecules, even radicals or gaseous species. Future applications might look into the formation of molecules inside helium droplets, the interaction of surface bound atoms to dopants immersed into the droplet, as well as the reaction dynamics of atoms on He_N in femtosecond time-resolved studies.

List of Figures

List of Tables

Bibliography

[1] O. Allard, S. Falke, A. Pashov, O. Dulieu, H. Knöckel, and E. Tiemann. Study of Coupled States for the $(4s^2)^1S+(4s4p)^3P$ Asymptote of Ca_2^*. *Eur. Phys. J. D*, 35(3):483–497, 2005.

[2] J. Allen and D. Misener. Flow of Liquid Helium II. *Nature*, 141:75, 1938.

[3] A. Allouche and M. Aubert-Frécon. Theoretical Study of Low-lying Electronic States of the CaLi Molecule. *Chem. Phys. Lett.*, 222(5):524 – 528, 1994.

[4] F. Ancilotto, P. B. Lerner, and M. W. Cole. Physics of Solvation. *J. Low Temp. Phys.*, 101:1123–1146, 1995.

[5] M. H. Anderson, J. R. Ensher, M. R. Matthews, C. E. Wieman, and E. A. Cornell. Observation of Bose-Einstein Condensation in a Dilute Atomic Vapor. *Science*, 269(5221):198–201, 1995.

[6] J. F. Annett. *Superconductivity, Superfluids and Condensates.* Oxford University Press, 2004.

[7] T. Aoki, Y. Yamanaka, M. Takeuchi, Y. Torii, and Y. Sakemi. Photoionization Loss in Simultaneous Magneto-optical Trapping of Rb and Sr. *Phys. Rev. A*, 87:063426, Jun 2013.

[8] G. Auböck. *Spectroscopy of Alkali-Metal Atoms and their High-Spin Oligomers on Helium Nanodroplets in External Magnetic Fields.* PhD thesis, Graz University of Technology, 2008.

[9] G. Auböck, M. Aymar, O. Dulieu, and W. E. Ernst. Reinvestigation of the $Rb_2(2)^3\Pi_g$ - $a^3\Sigma_u^+$ Band on Helium Nanodroplets. *J. Chem. Phys.*, 132(5):054304, 2010.

[10] G. Auböck, J. Nagl, C. Callegari, and W. E. Ernst. Electron Spin Pumping of Rb Atoms on He Nanodroplets via Nondestructive Optical Excitation. *Phys. Rev. Lett.*, 101(3):035301, July 2008.

[11] G. Auböck, J. Nagl, C. Callegari, and W. E. Ernst. Observation of Relativistic E $\otimes$ e Vibronic Coupling in Rb_3 and K_3 Quartet States on Helium Droplets. *J. Chem. Phys.*, 129(11):114501, 2008.

[12] G. Auböck, J. Nagl, J. Callegari, and W. E. Ernst. Triplet State Excitation of Alkali Molecules on Helium Droplets: Experiments and Theory. *J. Phys. Chem.*, A 2007, 111:7404–7410, 2007.

[13] L. Augustovičová and P. Soldán. Ab Initio Properties of MgAlk (Alk = Li, Na, K, Rb, Cs). *J. Chem. Phys.*, 136(8):084311, 2012.

[14] M. Aymar, R. Guérout, and O. Dulieu. Structure of the Alkali-metal-atom + Strontium Molecular Ions: Towards Photoassociation and Formation of Cold Molecular Ions. *J. Chem. Phys.*, 135(6):064305, 2011.

[15] E. Becker, R. Klingelhofer, and P. Lohse. Strahlen aus Kondensiertem Helium im Hochvakuum. *Z. Naturforsch. A*, 16:1259, 1961.

[16] V. E. Bondybey and J. H. English. Laser-induced Fluorescence of the Calcium Dimer In Supersonic Jet - the Red Spectrum of Ca_2. *Chem. Phys. Lett.*, 111(3):195–200, 1984.

[17] N. Boutassetta, A. R. Allouche, and M. Aubert-Frécon. Theoretical Study of the Electronic Structure of the Sr_2 Molecule. *Phys. Rev. A*, 53(6):3845–3852, June 1996.

[18] C. C. Bradley, C. A. Sackett, J. J. Tollett, and R. G. Hulet. Evidence of Bose-Einstein Condensation in an Atomic Gas with Attractive Interactions. *Phys. Rev. Lett.*, 75(9):1687–1690, Aug. 1995.

[19] D. Brink and S. Stringari. Density of States and Evaporation Rate of Helium Clusters. *Z. Phys. D Atom. Mol. Cl.*, 15(3):257–263, 1990.

[20] F. R. Brühl, R. A. Miron, and W. E. Ernst. Triplet States of Rubidium Dimers on Helium Nanodroplets. *J. Chem. Phys.*, 115(22):10275–10281, 2001.

[21] F. R. Brühl, R. A. Trasca, and W. E. Ernst. Rb-He Exciplex Formation on Helium Nanodroplets. *J. Chem. Phys.*, 115(22):10220–10224, Dec. 2001.

[22] H. Buchenau, E. L. Knuth, J. Northby, J. P. Toennies, and C. Winkler. Mass Spectra and Time-of-Flight Distributions of Helium Cluster Beams. *J. Chem. Phys.*, 92(11):6875–6889, 1990.

[23] H. Buchenau, J. P. Toennies, and J. A. Northby. Excitation and Ionization of ^{4}He Clusters by Electrons. *J. Chem. Phys.*, 95(11):8134–8148, 1991.

[24] O. Bünermann. *Spektroskopie von Alkali- und Erdalkaliatomen, -molekülen, Alkaliclustern und Komplexen organischer Moleküle auf Heliumnanotröpfchen.* PhD thesis, Universität Bielefeld, 2006.

[25] B. Bussery-Honvault and R. Moszynski. Ab Initio Potential Energy Curves, Transition Dipole Moments and Spin-Orbit Coupling Matrix Elements for the First Twenty States of the Calcium Dimer. *Mol. Phys.*, 104(13-14):2387–2402, 2006.

[26] C. Callegari and W. E. Ernst. *Handbook of High-Resolution Spectroscopy,* eds. M. Quack and F. Merkt, chapter : Helium Droplets as Nanocryostats for Molecular Spectroscopy - from the Vacuum Ultraviolet to the Microwave Regime, pages 1551–1594. John Wiley & Sons, Chichester, 2011.

[27] L. D. Carr, D. DeMille, R. V. Krems, and J. Ye. Cold and Ultracold Molecules: Science, Technology and Applications. *New Journal of Physics*, 11:055049, May 2009.

[28] F. Chevy and C. Salomon. Superfluidity in Fermi Gases. *Physics World*, 18(3), 2005.

[29] C. Chin, R. Grimm, P. Julienne, and E. Tiesinga. Feshbach Resonances in Ultracold Gases. *Rev. Mod. Phys.*, 82:1225–1286, Apr 2010.

[30] E. Czuchaj, M. Krosnicki, and H. Stoll. Valence Ab Initio Calculation of the Potential Energy Curves for Ca-Rare Gas Van Der Waals Molecules. *Chem. Phys.*, 292(1):101–110, July 2003.

[31] F. Dalfovo, S. Giorgini, L. Pitaevskii, and S. Stringari. Theory of Bose-Einstein Condensation in Trapped Gases. *Rev. Mod. Phys.*, 71:463, 1999.

[32] F. Dalfovo and S. Stringari. Helium Nanodroplets and Trapped Bose Einstein Condensates as Prototypes of Finite Quantum Fluids. *J. Chem. Phys.*, 115(22):10078–10089, 2001.

[33] J. G. Danzl, E. Haller, M. Gustavsson, M. J. Mark, R. Hart, N. Bouloufa, O. Dulieu, H. Ritsch, and H.-C. Nägerl. Quantum Gas of Deeply Bound Ground State Molecules. *Science*, 321(5892):1062–1066, 2008.

[34] J. G. Danzl, M. J. Mark, E. Haller, M. Gustavsson, R. Hart, J. Aldegunde, J. M. Hutson, and H.-C. Nägerl. An Ultracold High-Density Sample of Rovibronic Ground-State Molecules in an Optical Lattice. *Nat. Phys.*, 6(4):265–270, 2010.

[35] K. B. Davis, M. O. Mewes, M. R. Andrews, N. J. van Druten, D. S. Durfee, D. M. Kurn, and W. Ketterle. Bose-Einstein Condensation in a Gas of Sodium Atoms. *Phys. Rev. Lett.*, 75(22):3969–3973, Nov. 1995.

[36] J. Deiglmayr, A. Grochola, M. Repp, K. Mörtlbauer, C. Glück, J. Lange, O. Dulieu, R. Wester, and M. Weidemüller. Formation of Ultracold Polar Molecules in the Rovibrational Ground State. *Phys. Rev. Lett.*, 101(13):133004, Sept. 2008.

[37] D. DeMille. Quantum Computation with Trapped Polar Molecules. *Phys. Rev. Lett.*, 88:067901, Jan 2002.

[38] W. Demtröder. *Molekülphysik Theoretische Grundlagen und experimentelle Methoden.* Oldenbourg, 2003. ISBN 3-486-24974-6.

[39] L. A. der Lan, P. Bartl, C. Leidlmair, H. Schöbel, S. Denifl, T. D. Märk, A. M. Ellis, and P. Scheier. Submersion of Potassium Clusters in Helium Nanodroplets. *Phys. Rev. B*, 85(11):115414, 2012.

[40] L. A. der Lan, P. Bartl, C. Leidlmair, H. Schöbel, R. Jochum, S. Denifl, T. D. Märk, A. M. Ellis, and P. Scheier. The Submersion of Sodium Clusters in Helium Nanodroplets: Identification of the Surface - Interior Transition. *J. Chem. Phys.*, 135(4):044309, 2011.

[41] R. J. Donnelly. The Discovery of Superfluid Helium. *Physics Today*, pages 30–35, 1995.

[42] R. J. Donnelly. The Two-fluid Theory and Second Sound in Liquid Helium. *Physics Today*, 62(10):34–39, Oct. 2009.

[43] R. J. Donnelly and C. F. Barenghi. The Observed Properties of Liquid Helium at the Saturated Vapor Pressure. *J. Phys. Chem. Ref. Data*, 27(6):1217–1274, 1998.

[44] S. C. Doret, C. B. Connolly, W. Ketterle, and J. M. Doyle. Buffer-Gas Cooled Bose-Einstein Condensate. *Phys. Rev. Lett.*, 103(10):103005–, Sept. 2009.

[45] W. E. Ernst, R. Huber, S. Jiang, R. Beuc, M. Movre, and G. Pichler. Cesium Dimer Spectroscopy on Helium Droplets. *J. Chem. Phys.*, 124:024313, 2006.

[46] L. Fechner, B. Grüner, A. Sieg, C. Callegari, F. Ancilotto, F. Stienkemeier, and M. Mudrich. Photoionization and Imaging Spectroscopy of Rubidium Atoms Attached to Helium Nanodroplets. *Phys. Chem. Chem. Phys.*, 14:3843–3851, 2012.

[47] R. P. Feynman. Superfluidity and Superconductivity. *Rev. Mod. Phys.*, 29(2):205–212, 1957.

[48] T. Fliessbach. *Statistische Physik; Lehrbuch zur Theoretischen Physik IV*. Spektrum, 2010.

[49] D. G. Fried, T. C. Killian, L. Willmann, D. Landhuis, S. C. Moss, D. Kleppner, and T. J. Greytak. Bose-Einstein Condensation of Atomic Hydrogen. *Phys. Rev. Lett.*, 81(18):3811–3814, Nov. 1998.

[50] M. Gaveau, M. Briant, P. Fournier, J. Mestdagh, and J. Visticot. Spectroscopy and Dynamics of Calcium Dimers Deposited on Large Argon and Neon van der Waals Clusters. *J. Chem. Phys.*, 116(3):955–963, 2002.

[51] G. Gerber, R. Möller, and H. Schneider. Laser Induced Bound-Bound and Bound-Continuum Emission of the Sr_2 $A^1\Sigma_u^+$ - $X^1\Sigma_g^+$. *J. Chem. Phys.*, 81(4):1538–1551, 1984.

[52] L. F. Gomez, E. Loginov, R. Sliter, and A. F. Vilesov. Sizes of Large He Droplets. *J. Chem. Phys.*, 135(15):154201, 2011.

[53] G. Gopakumar, M. Abe, M. Hada, and M. Kajita. Ab Initio Study of Ground and Excited States of $^6Li^{40}Ca$ and $^6Li^{88}Sr$ Molecules. *J. Chem. Phys.*, 138(19):194307–14, May 2013.

[54] G. Gopakumar, M. Abe, M. Hada, and M. Kajita. Dipole Polarizability of Alkali-Metal (Na, K, Rb) - Alkaline-Earth-Metal (Ca, Sr) Polar Molecules: Prospects for Alignment. *arXiv:1405.3503*, 2014.

[55] G. Gopakumar, M. Abe, M. Kajita, and M. Hada. *Ab initio* Study of Permanent Electric Dipole Moment and Radiative Lifetimes of Alkaline-Earth-Metal–Li Molecules. *Phys. Rev. A*, 84:062514, Dec 2011.

[56] R. Guérout, M. Aymar, and O. Dulieu. Ground State of the Polar Alkali-Metal-Atom–Strontium Molecules: Potential Energy Curve and Permanent Dipole Moment. *Phys. Rev. A*, 82(4):042508, 2010.

[57] A. Guirao, M. Pi, and M. Barranco. Finite Size Effects in the Evaporation Rate of ^3He Clusters. *Z. Phys. D Atom. Mol. Cl.*, 21(2):185–188, 1991.

[58] H. Hara, Y. Takasu, Y. Yamaoka, J. M. Doyle, and Y. Takahashi. Quantum Degenerate Mixtures of Alkali and Alkaline-Earth-Like Atoms. *Phys. Rev. Lett.*, 106:205304, May 2011.

[59] J. Harms, M. Hartmann, J. P. Toennies, A. F. Vilesov, and B. Sartakov. Rotational Structure of the IR Spectra of Single SF_6 Molecules in Liquid ^4He and ^3He Droplets. *J. Mol. Spectrosc.*, 185(1):204–206, Sept. 1997.

[60] A. W. Hauser, G. Auböck, and W. E. Ernst. *Vibronic Interactions and the Jahn-Teller Effect: Theory and Applications*, volume 23 of *Progress in Theoretical Chemistry and Physics*, chapter Jahn-Teller Effect and Spin-Orbit Coupling in Heavy Alkali Trimers, pages 301–316. Springer Science+Business Media B.V., 2012.

[61] A. Hernando, A. Masson, M. Briant, J.-M. Mestdagh, M.-A. Gaveau, and N. Halberstadt. Fluorescence Emission of Ca-atom from Photodissociated Ca_2 in Ar Doped Helium Droplets. II. Theoretical. *J. Chem. Phys.*, 137:184311, 2012.

[62] A. Hernando, R. Mayol, M. Pi, M. Barranco, F. Ancilotto, O. Bünermann, and F. Stienkemeier. The Structure and Energetics of ^{3}He and ^{4}He Nanodroplets Doped with Alkaline Earth Atoms. *J. Phys. Chem. A*, 111(31):7303–7308, Apr. 2007.

[63] I. V. Hertel and C.-P. Schulz. *Atome, Moleküle und optische Physik 2 - Moleküle und Photonen- Spektroskopie und Streuphysik*. Springer, 2010. ISBN 978-3-642-11972-9.

[64] G. Herzberg. *Molecular Spectra and Molecular Structure I. Spectra of Diatomic Moleules*. Van Nostrand Reinhold, New York, 1950.

[65] J. Higgins, C. Callegari, J. Reho, F. Stienkemeier, W. E. Ernst, M. Gutowski, and G. Scoles. Helium Cluster Isolation Spectroscopy of Alkali Dimers in the Triplet Manifold. *J. Phys. Chem. A*, 102(26):4952–4965, 1998.

[66] J. Higgins, W. E. Ernst, C. Callegari, J. Reho, K. K. Lehmann, G. Scoles, and M. Gutowski. Spin Polarized Alkali Clusters: Observation of Quartet States of the Sodium Trimer. *Phys. Rev. Lett.*, 77(22):4532–4535, Nov. 1996.

[67] V. Hizhnyakov and G. Benedek. Vibronic Transitions Between States with Hard and Soft Phonon Dynamics. *Chem. Phys. Lett.*, 460:447–450, 2008.

[68] V. Hizhnyakov, I. Tehver, and G. Benedek. Theory of the Optical Spectrum of Na_2 on ^{4}He Droplets: Effects of the Zero-Point Energy of the Nearest Atoms. *Eur. Phys. J. B*, 70:507–512, 2009.

[69] R. T. Hofmann and D. O. Harris. Laser Spectroscopy, Rotational Assignment, and Perturbation Analysis of the $A^1\Sigma_u^+$ - $X^1\Sigma_g^+$ Ca_2 red system. *J. Chem. Phys.*, 85(7):3749–3759, 1986.

[70] M. Ivanova, A. Stein, A. Pashov, A. V. Stolyarov, H. Knockel, and E. Tiemann. The $X^2\Sigma^+$ State of LiCa Studied by Fourier-Transform Spectroscopy. *J. Chem. Phys.*, 135(17):174303, Nov. 2011.

[71] P. Jasik and J. Sienkiewicz. Calculation of Adiabatic Potentials of Li_2. *Chem. Phys.*, 323(2):563–573, 2006.

[72] F. Jensen. *Introduction to Computational Chemistry: Second Edition*. John Wiley & Sons, 2011. ISBN: 978-0470011874.

[73] K. M. Jones, S. Maleki, S. Bize, P. D. Lett, C. J. Williams, H. Richling, H. Knöckel, E. Tiemann, H. Wang, P. L. Gould, and W. C. Stwalley. Direct Measurement of the Ground-State Dissociation Energy of Na_2. *Phys. Rev. A*, 54:R1006–R1009, Aug 1996.

[74] K. M. Jones, E. Tiesinga, P. D. Lett, and P. S. Julienne. Ultracold Photoassociation Spectroscopy: Long-Range Molecules and Atomic Scattering. *Rev. Mod. Phys.*, 78(2):483–535, May 2006.

[75] M. Kajita, G. Gopakumar, M. Abe, and M. Hada. Elimination of the Stark Shift from the Vibrational Transition Frequency of Optically Trapped ^{174}Yb^{6}Li Molecules. *Phys. Rev. A*, 84:022507, Aug 2011.

[76] M. Kajita, G. Gopakumar, M. Abe, and M. Hada. Sensitivity of Vibrational Spectroscopy of Optically Trapped SrLi and CaLi Molecules to Variations in m_p/m_e. *J. Phys. B: At. Mol. Opt.*, 46(2):025001, 2013.

[77] L. Kapitza. Viscosity of Liquid Helium Below the λ-point. *Nature*, 141, 1938.

[78] A. Kautsch, M. Koch, and W. E. Ernst. Electronic Relaxation after Resonant Laser Excitation of Cr in Superfluid Helium Nanodroplets. *J. Phys. Chem. A*, 117 (39):9621–9625, Feb. 2013.

[79] E. Knuth. Size Correlations for Condensation Clusters Produced in Free-jet Expansions. *J. Chem. Phys.*, 107(21):9125–9132, 1997.

[80] T. Köhler, K. Góral, and P. S. Julienne. Production of Cold Molecules via Magnetically Tunable Feshbach Resonances. *Rev. Mod. Phys.*, 78(4):1311–1361, Dec. 2006.

[81] S. Kotochigova. Relativistic Electronic Structure of the Sr_2 Molecule. *J. Chem. Phys.*, 128(2):24303–24303, 2008.

[82] S. Kotochigova and P. Julienne. NIST Potential Energy Surface Database of Group II Dimer Molecules. Website, Aug. 2010. Available online at `http://physics.nist.gov/PhysRefData/PES/RefData/Sr.html`; visited on August 26$^{\text{th}}$ 2011.

[83] S. Kotochigova, A. Petrov, M. Linnik, J. Klos, and P. S. Julienne. Ab Initio Properties of Li-Group-II Molecules for Ultracold Matter Studies. *J. Chem. Phys.*, 135(16):164108, 2011.

[84] S. Kraft, F. Vogt, O. Appel, F. Riehle, and U. Sterr. Bose-Einstein Condensation of Alkaline Earth Atoms: ^{40}Ca. *Phys. Rev. Lett.*, 103(13):130401, Sept. 2009.

[85] R. V. Krems. Molecules Near Absolute Zero and External Field Control of Atomic and Molecular Dynamics. *Int. Rev. Phys. Chem.*, 24(1):99–118, Jan. 2005.

[86] G. Krois. Heavy Alkali and Alkaline Earth Metals on Cold Helium Droplets: First Comparison of Excitation Spectra. Master's thesis, Graz University of Technology, 2011.

[87] G. Krois, F. Lackner, J. V. Pototschnig, T. Buchsteiner, and W. Ernst. Characterization of RbSr Molecules: A Spectral Analysis on Helium Droplets. *submitted article*, 2014.

[88] G. Krois, J. V. Pototschnig, F. Lackner, and W. E. Ernst. Spectroscopy of Cold LiCa Molecules Formed on Helium Nanodroplets. *J. Phys. Chem. A*, 117(50):13719–13731, Dec. 2013.

[89] M. Krug. A Matlab Program to Control a Time-of-flight Multichannel Analyzer and Test Experiments on Caesium. Bachelorthesis, Graz University of Technology, 2010.

[90] F. Lackner. Laserspektroskopie und Flugzeitmassenspektrometrie an Rubidium-dotierten Heliumnanotröpfchen. Master's thesis, Graz University of Technology, 2009.

[91] F. Lackner. *Rydberg States of Alkali-Metal Atoms on Superfluid Helium Nanodroplets*. PhD thesis, Graz University of Technology, 2012.

[92] F. Lackner, G. Krois, T. Buchsteiner, J. V. Pototschnig, and W. E. Ernst. Helium Nanodroplet Assisted Preparation of Cold RbSr Molecules. *submitted article*, 2014.

[93] F. Lackner, G. Krois, and W. E. Ernst. RydbergRitz Analysis and Quantum Defects for Rb and Cs Atoms on Helium Nanodroplets. *Mol. Phys.*, 111, 14-15, Mar. 2013.

[94] F. Lackner, G. Krois, M. Koch, and W. E. Ernst. Rubidium on Helium Droplets: Analysis of an Exotic Rydberg Complex for $n* < 20$ and $0 <= l <= 3$. *J. Phys. Chem. Lett.*, 3(10):1404–1408, 2012.

[95] F. Lackner, G. Krois, M. Theisen, M. Koch, and W. E. Ernst. Spectroscopy of nS, nP, and nD Rydberg Series of Cs Atoms on Helium Nanodroplets. *Phys. Chem. Chem. Phys.*, 13:18781–18788, 2011.

[96] F. Lackner, J. Poms, G. Krois, J. V. Pototschnig, and W. E. Ernst. Spectroscopy of Lithium Atoms and Molecules on Helium Nanodroplets. *J. Phys. Chem. A*, 117 (46):11866–11873, July 2013.

[97] L. Landau. Theory of the Superfluidity of Helium II. *Phys. Rev.*, 60:356, 1941.

[98] R. J. Le Roy. Level 8.0. University of Waterloo Chemical Physics Research Report CP-663, University of Waterloo, 2007. A Computer Program for Solving the Radial Schrödinger Equation for Bound and Quasibound Levels.

[99] H. Lefebvre-Brion and R. Field. *The Spectra and Dynamics of Diatomic Molecules*. Elsevier, 2004.

[100] M. Lewerenz, B. Schilling, and J. Toennies. A New Scattering Deflection Method for Determining and Selecting the Sizes of Large Liquid Clusters of ^{4}He. *Chem. Phys. Lett.*, 206(1-4):381 – 387, 1993.

[101] M. Lewerenz, B. Schilling, and J. P. Toennies. Successive Capture and Coagulation of Atoms and Molecules to Small Clusters in Large Liquid Helium Clusters. *J. Chem. Phys.*, 102(20):8191–8207, 1995.

[102] D. Li, F. Xie, L. Li, A. Lazoudis, and A. M. Lyyra. New Observation of the ^{6}Li^{7}Li $3^3\Sigma_g^+$, $1^3\Delta_g$, and $2^3\Pi_g$ States and Molecular Constants with all $^6Li_2$, $^7Li_2$, and ^{6}Li^{7}Li Data. *J. Mol. Spectrosc.*, 246(2):180–186, 2007.

[103] D. R. Lide. *CRC Handbook of Chemistry and Physics, 84th Edition*. CRC Press. Boca Raton, 2003.

[104] E. Loginov, C. Callegari, F. Ancilotto, and M. Drabbels. Spectroscopy on Rydberg States of Sodium Atoms on the Surface of Helium Nanodroplets. *J. Phys. Chem. A*, 115:6779–88, 2011.

[105] E. Loginov and M. Drabbels. Excited State Dynamics of Ag Atoms in Helium Nanodroplets. *J. Phys. Chem. A*, 111(31):7504–7515, 2007.

[106] E. Loginov and M. Drabbels. Unusual Rydberg System Consisting of a Positively Charged Helium Nanodroplet with an Orbiting Electron. *Phys. Rev. Lett.*, 106(8):083401, 2011.

[107] E. Loginov and M. Drabbels. Spectroscopy and Dynamics of Barium-doped Helium Nanodroplets. *J. Chem. Phys.*, 136(15):154302, 2012.

[108] E. Loginov, D. Rossi, and M. Drabbels. Photoelectron Spectroscopy of Doped Helium Nanodroplets. *Phys. Rev. Lett.*, 95(16):163401, Oct. 2005.

[109] E. Lugovoj, J. P. Toennies, and A. Vilesov. Manipulating and Enhancing Chemical Reactions in Helium Droplets. *J. Chem. Phys.*, 112(19):8217, 2000.

[110] D. Mateo. Animations of Pickup Processes in He Droplets. `http://www.youtube.com/channel/UCG5C-EDeUh65BseG7UxNRIg`, 2013. [Online; accessed 14-July-2014].

[111] D. Mateo, A. Hernando, M. Barranco, E. Loginov, M. Drabbels, and M. Pi. Translational Dynamics of Photoexcited Atoms in ^{4}He Nanodroplets: The Case of Silver. *Phys. Chem. Chem. Phys.*, 15(42):18388–18400, 2013.

[112] A. Micheli, G. Brennen, and P. Zoller. A Toolbox for Lattice-Spin Models with Polar Molecules. *Nat. Phys.*, 2(5):341–347, 2006.

[113] J. C. Miller and L. Andrews. Laser-Excited Fluorescence of Calcium Dimer in Inert Gas Matrices. *J. Chem. Phys.*, 69(5):2054–2063, 1978.

[114] J. C. Miller, B. S. Ault, and L. Andrews. Absorption Spectra of Matrix-isolated Alkaline Earth Metal Diatomic Molecules. *J. Chem. Phys.*, 67(6):2478–2487, 1977.

[115] M. Mudrich, O. Bünermann, F. Stienkemeier, O. Dulieu, and M. Weidemüller. Formation of Cold Bialkali Dimers on Helium Nanodroplets. *Eur. Phys. J. D*, 31(2):291–299, 2004.

[116] R. S. Mulliken. The Interpretation of Band Spectra. Part IIc. Empirical Band types. *Rev. Mod. Phys.*, 3(1):89–155, Jan. 1931.

[117] R. S. Mulliken. Some Neglected Subcases of Predissociation in Diatomic Molecules. *J. Chem. Phys.*, 33(1):247–252, 1960.

[118] J. Nagl. Aufbau und Test einer Düsenstrahlapparatur zur Spektroskopie an Alkalimetall-dotierten Edelgasclustern. Master's thesis, Graz University of Technology, 2004.

[119] J. Nagl. *Spectroscopic Investigations of Homo- and Heteronuclear Molecules of K and Rb on the Surface of Argon and Helium Clusters.* PhD thesis, Graz University of Technology, 2008.

[120] J. Nagl, G. Aubčk, A. W. Hauser, O. Allard, C. Callegari, and W. E. Ernst. High-Spin Alkali Trimers on Helium Nanodroplets: Spectral Separation and Analysis. *J. Chem. Phys.*, 128(15):154320, 2008.

[121] J. Nagl, G. Auböck, A. W. Hauser, O. Allard, C. Callegari, and W. E. Ernst. Heteronuclear and Homonuclear High-Spin Alkali Trimers on Helium Nanodroplets. *Phys. Rev. Lett.*, 100:063001, 2008.

[122] J. Nagl, A. W. Hauser, G. Auböck, C. Callegari, and W. E. Ernst. Optical Spectroscopy of Potassium-Doped Argon Clusters. Experiments and Quantum-Chemistry Calculations. *J. Phys. Chem. A*, 111(49):12386–12397, Dec. 2007.

[123] K.-K. Ni, S. Ospelkaus, M. H. G. de Miranda, A. Pe'er, B. Neyenhuis, J. J. Zirbel, S. Kotochigova, P. S. Julienne, D. S. Jin, and J. Ye. A High Phase-Space-Density Gas of Polar Molecules. *Science*, 322(5899):231–235, 2008.

[124] S. Ospelkaus, A. Pe'er, K.-K. Ni, J. J. Zirbel, B. Neyenhuis, S. Kotochigova, P. S. Julienne, J. Ye, and D. S. Jin. Efficient State Transfer in an Ultracold Dense Gas of Heteronuclear Molecules. *Nat Phys*, 4(8):622–626, Aug. 2008.

[125] B. Pasquiou, A. Bayerle, S. M. Tzanova, S. Stellmer, J. Szczepkowski, M. Parigger, R. Grimm, and F. Schreck. Quantum Degenerate Mixtures of Strontium and Rubidium Atoms. *Phys. Rev. A*, 88:023601, Aug 2013.

[126] H. Pauly. *Atom, Molecule, and Cluster Beams I: Basic Theory, Production and Detection of Thermal Energy Beams*. Springer, 2000.

[127] H. Pauly. *Atom, Molecule, and Cluster Beams II: Cluster Beams, Fast and Slow Beams, Accessory Equipment and Applications*. Springer, 2000.

[128] J. Persson, Q. Hui, M. Nakamura, and M. Takami. Optical Spectra of Metal Dimers and Trimers in Superfluid Helium. *Phys. Rev. A.*, 52(3):2011, 1995.

[129] A. Pifrader. Pulsed Laser Spectroscopic Investigations of Rubidium Atoms Attached to Helium Nanodroplets. Master's thesis, Graz University of Technology, 2009.

[130] A. Pifrader, O. Allard, G. Aubock, C. Callegari, W. E. Ernst, R. Huber, and F. Ancilotto. One- and Two-photon Spectroscopy of Highly Excited States of Alkali-metal Atoms on Helium Nanodroplets. *J. Chem. Phys.*, 133(16):164502, Oct. 2010.

[131] L. Pitaevski and S. Stringari. *Bose-Einstein Condensation*. Oxford Science Publications, 2003.

[132] J. V. Pototschnig. Theoretical Investigation of the Interaction between Chromium and Helium. Master's thesis, Graz University of Technology, 2012.

[133] J. V. Pototschnig. *A Theoretical Investigation of the Ground State and Excited States of Alkali - Alkaline Earth Diatomic Molecules*. PhD thesis, Graz University of Technology, expected 2015.

[134] G. Quemener and P. S. Julienne. Ultracold Molecules under Control! *Chem. Rev.*, 112(9):4949–5011, 2012.

[135] Y. Ralchenko, A. Kramida, J. Reader, and N. A. T. (2011). NIST Atomic Spectra Database (ver. 4.1.0). *National Institute of Standards and Technology, Gaithersburg, MD*, 2011.

[136] M. Ratschek, M. Koch, and W. E. Ernst. Doping Helium Nanodroplets with High Temperature Metals: Formation of Chromium Clusters. *J. Chem. Phys.*, 136(10):104201, 2012.

[137] J. Reho, C. Callegari, J. Higgins, W. E. Ernst, K. K. Lehmann, and G. Scoles. Spin-Orbit Effects in the Formation of the Na-He Excimer on the Surface of He Clusters. *Faraday Discuss.*, 108:161–174, 1997.

[138] Y. Ren and V. V. Kresin. Surface Location of Alkaline-earth-metal-atom Impurities on Helium Nanodroplets. *Phys. Rev. A*, 76:043204, 2007.

[139] L. M. Russon, G. K. Rothschopf, M. D. Morse, A. I. Boldyrev, and J. Simons. Two-Photon Ionization Spectroscopy and All-Electron Ab Initio Study of LiCa. *J. Chem. Phys.*, 109(16):6655–6665, Oct. 1998.

[140] A. A. Scheidemann, V. V. Kresin, and H. Hess. Capture of Lithium by ^{4}He Clusters: Surface Adsorption, Penning Ionization, and Formation of $HeLi^+$. *J. Chem. Phys.*, 107(8):2839–2844, 1997.

[141] M. Schnell and G. Meijer. Cold Molecules: Preparation, Applications, and Challenges. *Angew. Chem. Int. Edit.*, 48(33):6010–6031, 2009.

[142] G. Scoles. *Atomic and Molecular Beam Methods Volume 1.* Oxford University Press, 1988.

[143] G. Scoles. *Atomic and Molecular Beam Methods Volume 2.* Oxford University Press, 1988.

[144] C. Stark and V. V. Kresin. Critical Sizes for the Submersion of Alkali Clusters into Lliquid Helium. *Phys. Rev. B*, 81:085401, 2010.

[145] Stefan Frädrich (Autor), Timo Wuerz (Illustrator). *Günter, der innere Schweinehund: Ein tierisches Motivationsbuch.* GABAL, 2011. ISBN: 978-3897494572.

[146] A. Stein, M. Ivanova, A. Pashov, H. Knöckel, and E. Tiemann. Spectroscopic Study of the $2^2\Sigma^+$ and the $4^2\Sigma^+$ Excited States of LiCa. *J. Chem. Phys.*, 138(11):114306, 2013.

[147] A. Stein, H. Knöckel, and E. Tiemann. Fourier-transform Spectroscopy of Sr_2 and Revised Ground-state Potential. *Phys. Rev. A*, 78(4):042508–, Oct. 2008.

[148] A. Stein, H. Knöckel, and E. Tiemann. The States $1^1\Sigma_u^+$, $1^1\Pi_u$ and $1^1\Sigma_u^+$ of Sr_2 Studied by Fourier-transform Spectroscopy. *Eur. Phys. J. D*, 64(2-3):227–238, 2011.

[149] S. Stellmer, B. Pasquiou, R. Grimm, and F. Schreck. Creation of Ultracold Sr_2 Molecules in the Electronic Ground State. *Phys. Rev. Lett.*, 109:115302, Sep 2012.

[150] S. Stellmer, M. K. Tey, B. Huang, R. Grimm, and F. Schreck. Bose-Einstein Condensation of Strontium. *Phys. Rev. Lett.*, 103(20):200401, Nov. 2009.

[151] F. Stienkemeier, J. Higgins, C. Callegari, S. I. Kanorsky, W. E. Ernst, and G. Scoles. Spectroscopy of Alkali Atoms (Li, Na, K) Attached to Large Helium Clusters. *Z. Phys. D: At., Mol. Clusters*, 38(3):253–263, 1996.

[152] F. Stienkemeier, J. Higgins, W. Ernst, and G. Scoles. Spectroscopy of Alkali Atoms and Molecules Attached to Liquid He Clusters. *Z. Phys. B*, 98:413–416, 1995.

[153] F. Stienkemeier, F. Meier, and H. Lutz. Alkaline Earth Metals (Ca, Sr) Attached to Liquid Helium Droplets: Inside or Out. *J. Chem. Phys.*, 107:10816, 1997.

[154] I. Tehver, V. Hizhnyakov, and G. Benedek. Sodium Molecule on the Surface of Liquid Helium-4 Droplets: Optical Transitions Probe Collective Excitations. *Phys. Status Solidi C*, 10(2):232–235, 2013.

[155] G. Thalhammer, K. Winkler, F. Lang, S. Schmid, R. Grimm, and J. H. Denschlag. Long-Lived Feshbach Molecules in a Three-Dimensional Optical Lattice. *Phys. Rev. Lett.*, 96:050402, Feb 2006.

[156] M. Theisen. *Aggregation of Rb and Cs atoms on Helium Nanodroplets and Laser Ionization of Cold Clusters.* PhD thesis, Graz University of Technology, 2011.

[157] M. Theisen, F. Lackner, F. Ancilotto, C. Callegari, and W. E. Ernst. Two-step Excitation of Rb Atoms on He Nanodroplets. *Eur. Phys. J. D*, 61(2):403–408, Jan. 2011.

[158] M. Theisen, F. Lackner, and W. E. Ernst. Forming Rb+ Snowballs in the Center of He Nanodroplets. *Phys. Chem. Chem. Phys.*, 12(45):14861–14863, 2010.

[159] M. Theisen, F. Lackner, and W. E. Ernst. Cs Atoms on Helium Nanodroplets and the Immersion of Cs^+ into the Nanodroplet. *J. Chem. Phys.*, 135(7):074306, 2011.

[160] M. Theisen, F. Lackner, G. Krois, and W. E. Ernst. Ionization Thresholds of Alkali Metal Atoms on Helium Droplets. *J. Phys. Chem. Lett.*, 2(21):2778–2782, Nov. 2011.

[161] L. Tisza. On the Thermal Supraconductibility of Liquid Helium II and the Bose-Einstein Statistics. *Comptes Rendus Hebdomadaires Des Seances De L Academie Des Sciences*, 207:1035–1037, 1938.

[162] J. Toennies. Die Faszinierenden Quanteneigenschaften von Helium und Ihre Anwendung. *Physik Journal*, 7/8:49–55, 2002.

[163] J. P. Toennies and A. F. Vilesov. Superfluid Helium Droplets: A Uniquely Cold Nanomatrix for Molecules and Molecular Complexes. *Angew. Chem. Int. Edit.*, 43(20):2622–2648, 2004.

[164] J. Ulmanis, J. Deiglmayr, M. Repp, R. Wester, and M. Weidemüller. Ultracold Molecules Formed by Photoassociation: Heteronuclear Dimers, Inelastic Collisions, and Interactions with Ultrashort Laser Pulses. *Chem. Rev.*, 112(9):4890–4927, 2012.

[165] N. Vitanov, M. Fleischhauer, B. Shore, and K. Bergmann. Coherent Manipulation of Atoms and Molecules by Sequential Laser Pulses. In B. Bederson and H. Walther, editors, *Advances In Atomic, Molecular, and Optical Physics*, volume Volume 46 of *Advances In Atomic, Molecular, and Optical Physics*, pages 55–190. Elsevier, 2001.

[166] M. Weidemüller and C. Zimmermann, editors. *Cold Atoms and Molecules.* Wiley-VCH, 2009.

[167] X. Xie and R. Field. Perturbation Facilitated Optical-Optical Double Resonance spectroscopy of the $^6Li_2$ $3^3\Sigma_g^+$, $2^3\Pi_g$, $1^3\Delta_g$, $b^3\Pi_u$, and $a^3\Sigma_u^+$ states. *J. Mol. Spectrosc.*, 117:228–244, 1986.

[168] T. Zelevinsky, S. Kotochigova, and J. Ye. Precision Test of Mass-ratio Variations With Lattice-confined Ultracold Molecules. *Phys. Rev. Lett.*, 100(4):043201, Feb. 2008.

[169] P. Żuchowski, R. Guerout, and O. Dulieu. Ground- and excited-state properties of the polar and paramagnetic RbSr molecule: A comparative study. *Phys. Rev. A*, 90:012507, 2014. arXiv:1402.0702.

[170] P. S. Żuchowski, J. Aldegunde, and J. M. Hutson. Ultracold RbSr Molecules Can Be Formed by Magnetoassociation. *Phys. Rev. Lett.*, 105:153201, Oct 2010.

Danksagung

Figure 1: Der Schweinehund. Treuer Wegbegleiter über viele Jahre. Bild aus den Tiefen des Internets, ursprünglich aus dem Buch 'Günter, der innere Schweinehund' [145]. Dieses Bild diente sowohl in meiner Masterarbeit als auch in dieser Arbeit als Muster für noch zu erstellende Bilder.

Die letzte Seite dieser Arbeit möchte ich dazu nutzen, um den Menschen zu danken die, direkt oder indirekt, an der Er- und Fertigstellung dieser Arbeit beteilig waren. Direkt, indem sie mich in meiner Arbeit betreut und begleitet haben und indirekt indem sie mich unterstützt und motiviert haben, sozusagen meinen inneren Schweinehund immer wieder einmal Gassi geführt haben.

Zuerst möchte ich mich bei meinem Betreuer Prof. Wolfgang E. Ernst bedanken, ohne den ich nicht nur keine Anstellung an der TU hätte, sondern nicht einmal die Apparatur selbst vorhanden wäre. Im Besonderen möchte ich mich dafür bedanken, eine gute Anstellung bekommen zu haben, in der ich mich ausschließlich der Arbeit im Rahmen meiner Dissertation widmen konnte, sowie für die Möglichkeit, pünktlich zum Ende meines Arbeitsvertrags auch die Dissertation abschließen zu können beides ist keineswegs selbstverständlich.
Zusätzlich auch Danke dafür, dass ich durchaus zwischendurch eigene Interessen verfolgen konnte und auch schon einmal für eine interessante, wenn auch nicht unbedingt themenbezogene Summer School freigestellt wurde.
Fachlicher Natur gebührt der größte Dank meinem Laborkollegen, Co-Betreuer und 'Chef' Flo. An dieser Stelle Danke für mittlerweile fast vier Jahre treue Begleitung durch stressige und lockere, durch motivierte und weniger motivierte Phasen. Danke dir für viele geduldige Erklärungen und so manches nächtliche Bier!
An dieser Stelle auch ein Dankeschön an Johann für die theoretisch-praktische Unterstützung

bei der Erklärung unserer Daten sowie auch so mancher theoretischen Frage und an Thomas für die technische und motivierende Unterstützung im Labor und für die zahlreichen angeregten Diskussionen zu ebenso zahlreichen Themen.

Damit kommen wir nun schon an den Schnittpunkt vom Beruflichen und Privaten, vielen Dank an alle die im Laufe meiner Dissertation an diesem Institut waren und das soziale Rückgrat meiner Arbeit gebildet haben, das mir persönlich so wichtig ist. Den Heliumsurfern (Toni, Mike und Pat) und dem weltraumwissenschaftlichen Außenposten (Michi) vielen Dank für die wunderbaren Unterhaltungen in zahlreichen kreativen Kaffeepausen. Im Speziellen: Danke an Toni fürs ansudern lassen, an Pat fürs mitsudern und an Mike für die erfolgreichen Ausgleiche draußen, ich hoffe auf weitere Projekte!
Weiter im Privaten möchte ich mich bei zumindest einigen meiner Freunde bedanken (und hoffe, dass der Rest nicht beleidigt ist): Gernot, Danke für die vielen 'Theoriekaffees', die 'Securitybriefings', die sozialen Tratscherl und die sanften, aber bestimmten und unaufhörlichen Hinweise, dass Linux doch besser ist als Windows. Irgendwann schaff ich die Konvertierung schon noch. Babsi, Danke fürs da sein wann auch immer ich dich brauche! Aber auch für so manche arbeitsbezogene Diskussion, durch dich habe ich die Welt der Wissenschaft zum Teil besser verstehen gelernt als durch meine Arbeit selbst. Kathi, geteilte Müh' ist halbe Müh', das Credo gilt, wir habens fast geschafft und ich finde am Ende haben wirs doch ganz gut gemacht, Danke für die treue Begleitung!
Wo wir schon bei treuer Begleitung sind, liebe Andrea, irgendwie ist seit einiger Zeit alles um einiges leichter als zuvor. Danke fürs Zuhören, Motivieren und vor allem Ablenken, aber auch fürs Korrigieren! Tja, die Chemie zwischen Naturwissenschaftlern und Geisteswissenschaftlern kann doch stimmen. Ganz ordentlich sogar.
Zu guter Letzt, Danke an Mama und Papa. Es ist schön, auch in einem Alter, in dem man (theoretisch) erwachsen sein sollte, noch ein ruhiges und sicheres Zuhause zu haben, in das man sich flüchten kann, wenn man Ausgleich oder Entspannung sucht. Genauso schön ist das Wissen, dass, egal wo es hingeht, alles eigentlich gar nicht so schlimm werden kann, weil da ja immer noch ein Zuhause ist, in das man zurükkehren kann.